NUMERICAL ANALYSIS OF SCRAMJET CAVITY FLAMEHOLDERS AT VARYING FLIGHT MACH NUMBERS

A Thesis
Presented to
the Graduate School of
Clemson University

In Partial Fulfillment
of the Requirements for the Degree
Master of Science
Mechanical Engineering

---

by
Matthew Quinones
December 2018

Accepted by:
Dr. Richard Miller, Committee Chair
Dr. John Saylor
Dr. Xiangchun Xuan

Abstract

Various types of air breathing engines are used as propulsion devices in aviation. At high flight velocities, the use of a ramjet or supersonic combustion ramjet (scramjet) may be preferred due to the natural compressibility of air at high speed. A scramjet, while similar to the ramjet, does not slow air to subsonic speeds prior to combustion, allowing it to operate at much higher flight velocities at very high altitude. For this reason, however, the residence time of air inside of the combustor is on the order of milliseconds, requiring rapid mixing and ignition of the fuel to generate adequate thrust. To do this, a flameholder is often used, which generates turbulence, shock waves, and maintains a recirculation region through geometric effects. In this study, four geometry types involving eighteen separate designs were chosen and analyzed using CFD software. Isolator inlet Mach numbers of 2.2, 4, 6, 8, and 10 were selected to model varying flight velocity, and hydrogen fuel was injected sonically at all injector locations with a single step reaction mechanism applied for combustion. An existing square cavity model was chosen and modified to produce slanted cavity, double cavity, and combined strut-cavity designs. The flameholders were analyzed in a non-reacting simulation to observe their effects on the flow field and fuel mixing efficiency. Reacting simulations were performed for each flameholder to investigate flame stabilization capabilities, thermal choking, stagnation pressure losses and drag generated inside of the combustor. Results show that all designs sustain a flame during combustion at all flight Mach numbers. However, the square cavity with a back cavity injector does this while limiting losses and drag due to shock wave formation, thermal choking, and geometric effects in the flow.

Acknowledgements

I would like to thank my advisor, Dr. Miller, for providing me feedback on my research and guiding me during my time as a graduate student. I would also like to thank Dr. Saylor and Dr. Xuan for serving on my committee.

Thank you to my family and friends for supporting me throughout my college career, especially during graduate school. Special thanks go to Morgan for putting up with my seemingly constant ranting about failed simulations.

Finally, I would like to thank Clemson University for allowing me access to the Palmetto cluster to accelerate my research. The use of the cluster was invaluable to me, and I am extremely grateful to have had access to such a powerful processing tool.

Table of Contents

Page

Abstract....ii

Acknowledgements iii

List of Figures vi

1 Introduction....1

1.1 Literature Review 2

1.2 Objectives....3

2 Flow Modeling Theory....4

2.1 Governing Equations of Fluid Motion....4

2.2 Reynolds Averaging and Favre Averaging....6

2.3 Turbulence Modeling....8

2.4 Species Transport 11

2.5 Thermodynamic Equation of State....12

2.6 Combustion Modeling 13

3 Computational Method....13

3.1 Computational Setup 13

3.2 Combustor Geometries 14

3.3 Meshing....26

3.4 Initialization and Boundary Conditions....29

4 Results and Analysis....30

4.1 Non-Reacting Simulations at M = 2.2 30

Table of Contents (cont.)

Page

4.1.1 Effects of Flameholder on Non-Reacting Flow Field....................................30
4.1.2 Mixing Efficiency..39
4.2 Reacting Simulations at M = 2.2..47
4.3 Reacting Simulations at M = 4..58
4.4 Reacting Simulations at M = 6..67
4.5 Reacting Simulations at M = 8..72
4.6 Reacting Simulations at M = 10..76
4.7 Viability of Flameholders in a Reacting Flow.......................................80
4.7.1 Shock Trains and Engine Unstart..80
4.7.2 Stagnation/Total Pressure Losses..83
4.7.3 Net Thrust...90
5 Conclusion..93
Nomenclature..95
References..98

List of Figures **Page**

Figure 1 Square Cavity Geometry (all lengths in mm) 14

Figure 2 Square Cavity Main Injector (all units in mm) 15

Figure 3 Bottom Cavity Injector (all units in mm) 16

Figure 4 Back Cavity Injector (all units in mm) 16

Figure 5 Slanted Cavity Geometry (all units in mm) 17

Figure 6 Main Inlet for Slanted Cavity (all units in mm) 18

Figure 7 Front Inlet, Slanted Cavity (all units in mm) 19

Figure 8 Bottom Inlet, Slanted Cavity (all units in mm) 19

Figure 9 Top Injector Location (all units in mm) 20

Figure 10 New Main Injector Location (all units in mm) 21

Figure 11 Double Cavity Geometry (all units in mm) 22

Figure 12 Double Cavity Normal Injector (all units in mm) 23

Figure 13 Double Cavity Parallel Injector (all units in mm) 23

Figure 14 Strut-Cavity Geometry (all units in mm) 24

Figure 15 Strut Flameholder, 10 by 10 (all units in mm) 25

Figure 16 Strut Fuel Injector, 10 by 10 26

Figure 17 Square Cavity Tet Mesh 28

Figure 18 Slanted Cavity Tet Mesh 28

Figure 19 Double Cavity Tet Mesh 28

Figure 20 10 by 10 Strut-Cavity Tet Mesh 29

Figure 21 Square Cavity Non-Reacting Pressure 30

List of Figures (cont.)

Page

Figure 22 Slanted Cavity Non-Reacting Pressure..31

Figure 23 Double Cavity Non-Reacting Pressure..31

Figure 24 Slanted Cavity with Top Injector Non-Reacting Pressure..............................32

Figure 25 10 mm Strut-Cavity Non-Reacting Pressure...33

Figure 26 15 mm Strut-Cavity Non-Reacting Pressure...34

Figure 27 7.17 mm Strut-Cavity Non-Reacting Pressure..35

Figure 28 Square Cavity Flameholder Vortex..37

Figure 29 Slanted Cavity Flameholder Vortex...37

Figure 30 Double Cavity Flameholder Vortex...38

Figure 31 10 by 10 Strut Flameholder Vortex..38

Figure 32 Combustor Mixing Planes on 10 by 10 Strut-Cavity 41

Figure 33 Square Cavity Mixing Efficiencies 41

Figure 34 Slanted Cavity Mixing Efficiencies...42

Figure 35 Double Cavity Mixing Efficiencies...42

Figure 36 Slanted Cavity with Top Injector Mixing Efficiencies..................................43

Figure 37 10 mm Strut-Cavity Mixing Efficiencies..44

Figure 38 15 mm Strut-Cavity Mixing Efficiencies..45

Figure 39 7.17 mm Strut-Cavity Mixing Efficiencies...46

Figure 40 Flame Position, Square Cavity M = 2.2...49

Figure 41 Flame Position, Slanted Cavity M = 2.2..50

Figure 42 Flame Position, Double Cavity M = 2.2 51

List of Figures (cont.)

Page

Figure 43 Flame Position, Slanted Cavity with Top Injector M = 2.2 52

Figure 44 Flame Position, 10 mm Strut-Cavity M = 2.2 53

Figure 45 Flame Position, 15 mm Strut-Cavity M = 2.2 54

Figure 46 Flame Position, 7.17 mm Strut-Cavity M = 2.2 55

Figure 47 Flame Position, Square Cavity M = 4 59

Figure 48 Flame Position, Slanted Cavity M = 4 60

Figure 49 Flame Position, Double Cavity M = 4 61

Figure 50 Flame Position, Slanted Cavity with Top Injector M = 4 62

Figure 51 Flame Position, 10 mm Strut-Cavity M = 4 63

Figure 52 Flame Position, 15 mm Strut-Cavity M = 4 64

Figure 53 Flame Position, 7.17 mm Strut-Cavity, M = 4 65

Figure 54 Flame Position, Square Cavity M = 6 67

Figure 55 Flame Position, Slanted Cavity M = 6 67

Figure 56 Flame Position, Double Cavity M = 6 68

Figure 57 Flame Position, Slanted Cavity with Top Injector M = 6 68

Figure 58 Flame Distribution, 10 mm Strut-Cavity M = 6 69

Figure 59 Flame Position, 15 mm Strut-Cavity M = 6 70

Figure 60 Flame Position, 7.17 mm Strut-Cavity M = 6 71

Figure 61 Flame Position, Square Cavity M = 8 73

Figure 62 Flame Position, Slanted Cavity M = 8 73

Figure 63 Flame Position, Double Cavity M = 8 73

List of Figures (cont.)

Page

Figure 64 Flame Position, Slanted Cavity with Top Injector M = 8 74

Figure 65 Flame Position, 10 mm Strut-Cavity M = 8 74

Figure 66 Flame Position, 7.17 mm Strut-Cavity M = 8 75

Figure 67 Flame Position, 15 mm Strut-Cavity M = 8 75

Figure 68 Flame Position, Square Cavity M = 10 76

Figure 69 Flame Position, Slanted Cavity M = 10 77

Figure 70 Flame Position, Double Cavity M = 10 77

Figure 71 Flame Position, Slanted Cavity with Top Injector M = 10 78

Figure 72 Flame Position, 10 mm Strut-Cavity M = 10 78

Figure 73 Flame Position, 15 mm Strut-Cavity M = 10 79

Figure 74 Flame Position, 7.17 mm Strut-Cavity M = 10 79

Figure 75 Potential Unstart Conditions, 15 mm Strut-Cavity M = 2.2 81

Figure 76 Potential Unstart Conditions, 15 mm Strut-Cavity M = 4 82

Figure 77 Translated Shock Train in 15 mm Strut-Cavity M = 6 83

Figure 78 Stagnation Pressure at M = 2.2 84

Figure 79 Stagnation Pressure at M = 4 85

Figure 80 Stagnation Pressure at M = 6 86

Figure 81 Stagnation Pressure at M = 8 87

Figure 82 Stagnation Pressure at M = 10 88

Figure 83 Net Thrust by Mach Number 91

1 Introduction

In a traditional air breathing engine such as a turbofan, air is pulled into the engine via a fan, compressed in a compressor, mixed with fuel and then combusted. This heated gas then turns a turbine powering the compressor and fan, and then exits the engine to produce thrust. At higher flight velocities, the compressibility of air allows for the removal of the fan and compressor, forcing the air to compress as it enters a converging nozzle and slowing it to subsonic speeds; these engines, known as ramjets, operate with few moving parts and are often found on supersonic aircraft and missiles. At higher velocities, the air entering the engine cannot be slowed to subsonic speeds before entering the combustor, resulting in engines known as supersonic combustion ramjets (scramjets). As the name suggests, combustion occurs at supersonic speeds, after which the flow is accelerated using a diverging nozzle to generate thrust. With the ability to operate at flight Mach numbers upwards of 10 at high altitudes, scramjets would allow for travel between distant locations at unparalleled speeds while only using a few moving parts, allowing for durability over long periods of operation [1].

Scramjets operate at very high velocities, and therefore the air inside the engine has an extremely short residence time. If fuel is not properly mixed and combusted in this short period of time, a phenomenon known as flame blowout occurs, in which the flame forms outside of the combustor, and little to no thrust is generated. To avoid this, it is necessary to implement what is known as a flameholder inside of the combustor. A flameholder is usually a geometric variation inside of the combustor that generates turbulence and recirculation, which in turn promotes mixing of fuel and sustains reaction through recirculation of hot gases and combustion radicals. A flame (active combusting region) is often anchored on the flameholder because of this recirculation and shear layers that are created on the flameholder [2]. This helps start and maintain reaction within the combustor, which allows for consistent thrust to be produced. Each flameholder design creates turbulence and recirculation in different manners, but also negatively affects the flow field by generating drag, losses, and possible engine unstart due to shock wave formation, combustion oscillations, and thermal choking. For a flameholder to be effective, it must be able to sustain combustion at a wide range of flight Mach numbers without compromising thrust production.

1.1 Literature Review

At present, there have been numerous investigations into the characteristics and performance of scramjet engines; the majority of research has been focused on the development and analysis of flameholder geometries. Several different geometries that will be used as a basis for this study have already been tested experimentally, such as a square cavity in the wall by Micka and Driscoll [3], a slanted cavity design in the wall by Ben-Yakar and Hanson [4], and central strut in the flow field by Huang and Yan [5]. A fully operational experimental scramjet, known as the X-43A, has been tested several times by NASA, successfully cruising at a flight Mach number of 9.6 for approximately 10 seconds in 2004 [6].

Analyses tend to consist of CFD, small scale combustor testing, or a combination of the two. Several forms of CFD have been applied, primarily involving application of the Reynolds Averaged Navier-Stokes (RANS) and Large Eddy Simulation (LES) methods, such as their application to a strut based flameholder by Mura and Izard [7] and Berglund and Fureby [8], respectively. Both of these studies are focused on the performance of a strut flameholder, as well as verification of the capability of the models to predict combustion characteristics in the given engines. Small scale testing tends to focus on combustion characteristics of a flameholder based on a given flight Mach number or fuel equivalence ratio. For example, a double cavity flameholder at a Mach number of 2.64 was analyzed experimentally by Pan et al to observe the combustion mechanism of two cavities in parallel or in series with one another on the walls of a combustor [9]. Several other studies, including the study by Micka and Driscoll, were performed for similar reasons. To add to these existing studies, this paper will provide a comparative combustion analysis among several flameholder designs across a variety of flight Mach numbers.

1.2 Objectives

To understand the capabilities of various types of flameholders, four geometry types were chosen and analyzed using quasi-2D computational fluid dynamics (CFD). In this study, a square cavity, slanted cavity with and without a top wall injector, double cavity, and strut-cavity geometries were chosen and analyzed using ANSYS CFX software. Within this set of geometries, eighteen distinct designs were used with sonically injected hydrogen fuel to investigate the effects of fuel injection on flame stability and scramjet operation. The Mach number at the inlet of the geometry was set at values of 2.2, 4, 6, 8, and 10 to demonstrate how the flameholders behave at increasingly higher Mach numbers, modeling an increase in flight speed. Quantitative analyses were performed on each of the designs in a non-reacting case at an inlet Mach number of 2.2 to gauge mixing efficiency of the engine. Further analyses were performed in a reacting flow field at all Mach numbers to calculate the effects of the flameholders on the stagnation pressure of the flow and the net thrust or drag produced by the simulated engine. Qualitative analyses were performed to observe flame location and stabilization, as well as pressure distribution in the non-reacting case to demonstrate general flow characteristics as a result of the flameholders, and in the reacting case to observe possible loss of thrust due to air mass flow rate disruption at the engine intake.

2 Flow Modeling Theory

2.1 Governing Equations of Fluid Motion

When modeling the fluid within the scramjet, the fundamental conservation laws involving mass (continuity) and linear momentum are used as descriptors of a flow's motion. As supersonic flow is being considered, and compressibility effects are significant at approximately M > 0.3, the fully compressible forms of the conservation equations are required. The spatial and time derivatives of density are now non-zero, and therefore may not be neglected as is often done in incompressible flows. The continuity equation is then written in its general form as

$$\frac{\partial \rho}{\partial t} + \frac{\partial (\rho u_j)}{\partial x_j} = 0 \tag{1}$$

where ρ is the fluid density, and u_j the flow velocity in direction j. Since it is assumed that all simulations would be performed during cruising, in which flight velocity is constant due to a balance between thrust and total aircraft drag, Eq. (1) can be simplified to its stationary form:

$$\frac{\partial(\rho u_j)}{\partial x_j} = 0 \tag{2}$$

Also necessary is the linear momentum conservation equation, better known as the Navier-Stokes equation; its most general compressible form can be written as

$$\frac{\partial(\rho u_i)}{\partial t} + \frac{\partial(u_i \rho u_j)}{\partial x_j} = \frac{\partial \tau_{ij}}{\partial x_j} + \rho f_i \tag{3}$$

where τ_{ij} represents the Cauchy stress tensor (external surface forces) and f_i the external body forces on the fluid in the *i* direction. Once again, because the simulations are run during the cruising portion of flight, Eq. (3) may be simplified to its stationary form, written as

$$\frac{\partial(u_i \rho u_j)}{\partial x_j} = \frac{\partial \tau_{ij}}{\partial x_j} + \rho f_i \tag{4}$$

To calculate the stress tensor in each direction, a constitutive relation is necessary. The fluid considered in this study is air broken into its constituent gases (oxygen and nitrogen) mixing with hydrogen fuel and is treated as a Newtonian fluid. The stress tensor can then be written using Stokes hypothesis as

$$\tau_{ij} = -p\delta_{ij} + 2\mu\left(\frac{1}{2}\left(\frac{\partial u_i}{\partial x_j} + \frac{\partial u_j}{\partial x_i}\right) - \frac{\delta_{ij}}{3}\frac{\partial u_k}{\partial x_k}\right) \tag{5}$$

where p is the pressure of the fluid, μ the dynamic viscosity, and δ_{ij} the Kronecker delta tensor [10].

2.2 Reynolds Averaging and Favre Averaging

The high speed flow in a scramjet engine, as well as specific geometric features in the combustor or isolator will eventually result in the generation of turbulence in the boundary layer or free stream. To account for the presence of turbulence, the Reynolds decomposition can be applied to the governing flow equations shown in the previous section; this decomposition breaks down a variable in terms of its time averaged and fluctuating components. An example of this is shown using the x_1-direction velocity:

$$u_1 = \bar{u}_1 + u_1' \tag{6}$$

$$\bar{u}_1 = \lim_{\Delta t \to \infty} \frac{1}{\Delta \mathrm{t}} \int_t^{\mathrm{t}+\Delta \mathrm{t}} u_1 dt \tag{7}$$

This averaging operator can be applied to the continuity and Navier-Stokes equations to derive the Reynolds Averaged Navier-Stokes (RANS) equations, which are often implemented in CFD analyses to compute mean properties of the flow (velocities, temperatures, stresses, etc.).

Also common is the Favre average. Rather than only involving a time average, the Favre average is density weighted, which allows it to take into account the fluctuation of density due to compressibility effects. A similar decomposition can be performed on a variable that breaks it up into an averaged component and fluctuating component. For example, applying this decomposition to the x_1-direction velocity results in

$$u_1 = \tilde{u}_1 + u_1'' \tag{8}$$

$$\tilde{u}_1 = \frac{\overline{\rho u_1}}{\bar{\rho}} \tag{9}$$

To account for the variable density and turbulence in the scramjet, Eqs. (2) and (4) are modified using the Favre averaging operator, resulting in the following mean flow equations and constitutive relations [10]:

$$\frac{\partial\left(\bar{\rho}\tilde{u}_j\right)}{\partial x_j} = 0 \tag{10}$$

$$\frac{\partial\left(\tilde{u}_i\bar{\rho}\tilde{u}_j\right)}{\partial x_j} = -\frac{\partial \bar{p}}{\partial x_i} + \frac{\partial \bar{\sigma}_{ij}}{\partial x_j} - \frac{\partial \bar{R}_{ij}}{\partial x_j} \tag{11}$$

$$\bar{\sigma}_{ij} \approx 2\tilde{\mu}\left(\frac{1}{2}\left(\frac{\partial \tilde{u}_i}{\partial x_j} + \frac{\partial \tilde{u}_j}{\partial x_i}\right) - \frac{\delta_{ij}}{3}\frac{\partial \tilde{u}_k}{\partial x_k}\right) \tag{12}$$

$$\bar{R}_{ij} = \bar{\rho}\widetilde{u_i''u_j''} \tag{13}$$

Equations (10) and (11) are often called the Favre Averaged Navier-Stokes (FANS) equations, and are implemented in CFD in a similar way as the RANS equations (the effects of body forces from Eq. (4) are often assumed to be negligible). In Eq. (11), the averaged Cauchy stress tensor $\bar{\tau}_{ij}$ is broken down into pressure stress ($\bar{p}$) and viscous stress ($\bar{\sigma}_{ij}$) for simplification. The averaged viscous stress term defined in Eq. (12) is considered an approximation based on the assumption that $\overline{\rho' u_i'}/\bar{\rho}\bar{u}_i$ is small, which was demonstrated to be valid in a DNS simulation in [10]. A new term $\bar{R}_{ij}$ has been introduced as a result of the averaging process, and is known as the turbulence stress tensor (sometimes called the Reynolds stress tensor). To provide closure to the linear momentum equation, this term must be modeled.

2.3 Turbulence Modeling

In order to fully calculate the mean velocity using the RANS equations, it is necessary to model this stress tensor. As it is not possible to directly calculate this tensor due to the stochastic fluctuations of velocity in a turbulent flow field, it is often modeled in RANS using one of several turbulence models combined with the Boussinesq approximation. This approximation is written as

$$\bar{\rho}\widetilde{u_i''u_j''} = 2\bar{\rho}k\frac{\delta_{ij}}{3} + 2\bar{\mu}_t\left(\frac{1}{2}\left(\frac{\partial \tilde{u}_i}{\partial x_j} + \frac{\partial \tilde{u}_j}{\partial x_i}\right) - \frac{\delta_{ij}}{3}\frac{\partial \tilde{u}_k}{\partial x_k}\right) \tag{14}$$

where k is the turbulent kinetic energy, defined as

$$k = \frac{1}{2}\overline{u_i''u_i''} \tag{15}$$

and $\bar{\mu}_t$ is known as the eddy viscosity [10]. The eddy viscosity is not a true viscosity; rather, it is a representation of the stresses generated by the dissipation of turbulent eddies, much like how viscosity generates stresses due to particle interactions.

The method for calculating the eddy viscosity, as well as the turbulent kinetic energy, depends on the turbulence model that is implemented in the analysis. For all experiments in this study, Menter's k-ω Shear Stress Transport (SST) model was used, which involves additional transport equations for the turbulent kinetic energy (k) and the specific rate of dissipation (ω). The stationary forms of the two transport equations for this model are

$$\frac{\partial\left(\rho u_j k\right)}{\partial x_j} = P - \beta^*\rho\omega k + \frac{\partial}{\partial x_j}\left[\left(\mu + \sigma_k\mu_t\right)\frac{\partial k}{\partial x_j}\right] \tag{16}$$

$$\frac{\partial(\rho u_j \omega)}{\partial x_j} = \frac{\gamma_\omega \rho}{\mu_t} P - \beta \rho \omega^2 + \frac{\partial}{\partial x_j}\left[(\mu + \sigma_\omega \mu_t)\frac{\partial \omega}{\partial x_j}\right] + 2\rho(1 - F_1)\frac{\sigma_{\omega 2}}{\omega}\frac{\partial k}{\partial x_j}\frac{\partial \omega}{\partial x_j} \tag{17}$$

where P is a production term defined as

$$P = 2\mu_t\left(\frac{1}{2}\left(\frac{\partial u_i}{\partial x_j} + \frac{\partial u_j}{\partial x_i}\right) - \frac{1}{3}\frac{\partial u_k}{\partial x_k}\delta_{ij}\right) + \frac{2}{3}\rho k \delta_{ij} \tag{18}$$

and β, β^*, γ_ω, σ_ω, $\sigma_{\omega 2}$, and σ_k are constants. The eddy viscosity is calculated using

$$\mu_t = \rho \frac{a_1 k}{\max(a_1 \omega, \Omega F_2)} \tag{19}$$

where $a_1 = 0.31$ and Ω is the magnitude of vorticity [11].

This model makes use of two blending functions, written in Eq. (17) as F_1 and in Eq. (19) as F_2, which allow it to transition between the *k*-*ε* turbulence model in the free stream and the *k*-*ω* turbulence model in the boundary layer. The first blending function F_1 is calculated using

$$F_1 = \tanh(arg_1^4) \tag{20}$$

$$arg_1 = \min\left[max\left(\frac{\sqrt{k}}{0.09\omega d}; \frac{500\nu}{d^2\omega}\right); \frac{4\rho\sigma_{\omega 2}k}{CD_{k\omega}d^2}\right] \tag{21}$$

$$CD_{k\omega} = \max\left(2\rho\sigma_{\omega 2}\frac{1}{\omega}\frac{\partial k}{\partial x_j}\frac{\partial \omega}{\partial x_j}; 10^{-20}\right) \tag{22}$$

with d being the distance to the closest wall and ν the kinematic viscosity [11]. This function is used in Eq. (17) to change the effect of the turbulent kinetic energy and specific dissipation gradients at varying distances from the wall. It is also used to describe the constants in Eqs. (16) and (17), which are blended using

$$\phi = F_1\phi_1 + (1 - F_1)\phi_2 \tag{23}$$

where ϕ_1 and ϕ_2 are the specific constants in two separate sets that result in a single blended constant ϕ; the values in each set can be found in [11]. The second blending function F_2 is calculated with similar equations [11]:

$$F_2 = \tanh(arg_2^2) \tag{24}$$

$$arg_2 = \max\left(\frac{2\sqrt{k}}{0.09\omega d}; \frac{500\nu}{d^2\omega}\right) \tag{25}$$

This function F_2 appears when calculating the eddy viscosity as seen in Eq. (19).

The decision to use this turbulence model, as opposed to a simpler *k-ε* or the standard *k-ω* or a more complex model such as the Reynolds Stress Model (RSM) was based on computational complexity as well as robustness of the model. A model such as the RSM, while not requiring a constitutive relation to find the eddy viscosity directly (although such assumptions are required for the modeled Reynolds stress and dissipation equations), is far more computationally complex, introducing seven transport equations that must be solved to fully resolve the Reynolds stress tensor and provide closure for the RANS equations [12]. A simpler model, such as one of the *k-ε* models or other *k-ω* models can provide closure for the Reynolds stress tensor; however, they are deficient in handling certain types of flows. For example, the standard *k-ε* model, while adequate for modeling turbulence in free shear flows, struggles to accurately calculate the turbulent length scale near walls. Conversely, the standard *k-ω* is capable of predicting turbulence close to the wall, but is heavily dependent on freestream conditions to determine the value of *ω* outside of the boundary layer [13]. By blending the two of these models together, the SST turbulence model has the benefit of being able to predict turbulence in a shear flow (far from the wall in the scramjet), as well as close to the wall in the boundary layer (flow passing over walls or struts in the flow field). For this reason, it was advantageous to select this model when performing mixing and combustion analyses across all Mach numbers.

2.4 Species Transport

Along with the motion of the flow and the behavior of turbulence, it is necessary to model the production, transport, and consumption of all species involved in mixing and combustion. To do this, species transport equations are added to the simulations for hydrogen, oxygen, and water, while nitrogen remains as a constraint; in other terms, the remaining mass fraction after computing the mass fraction of the other three gases at a given location will be comprised of nitrogen. The stationary species transport equation is written as

$$\frac{\partial\left(u_j C_i\right)}{\partial x_j} = \frac{\partial}{\partial x_j}\left[D_i \frac{\partial C_i}{\partial x_j}\right] + S_i \tag{26}$$

where C_i is the mass concentration of gas i, D_i the diffusion coefficient for gas i, and S_i the production or consumption term for chemical reactions [14]. This equation can be Favre averaged, much like Eqs. (2) and (4), to generate the stationary mean species transport equation:

$$\frac{\partial\left(\tilde{u}_j \tilde{C}_i\right)}{\partial x_j} = \frac{\partial}{\partial x_j}\left[D_i \frac{\partial \tilde{C}_i}{\partial x_j}\right] + \tilde{S}_i - \frac{\partial\left(\widetilde{u_j'' C_i''}\right)}{\partial x_j} \tag{27}$$

An assumption can be made regarding the fluctuating term in Eq. (27), equating it to a coefficient K (eddy diffusion coefficient, a function of μ_t) multiplied by the negative gradient of the mean mass concentration, which is similar in form to Fick's first law [14]. The density weighted average mass fraction of a gas $\tilde{Y}_i$ can be defined as:

$$\tilde{Y}_i = \frac{\tilde{C}_i}{\bar{\rho}} \tag{28}$$

When combined with Eq. (27) and the assumption made regarding the fluctuating term, the result is the density weighted mean mass fraction transport equation [15]:

$$\frac{\partial\left(\bar{\rho}\tilde{u}_j\tilde{Y}_i\right)}{\partial x_j} = \frac{\partial}{\partial x_j}\left[\bar{\rho}K\frac{\partial \tilde{Y}_i}{\partial x_j} + \bar{\rho}D_i\frac{\partial \tilde{Y}_i}{\partial x_j}\right] + \tilde{S}_i \tag{29}$$

2.5 Thermodynamic Equation of State

To compute the Mach number at a given location, the ideal gas assumption was applied. Although water is present following combustion, it was assumed that at both the fuel and air inlets, only ideal gases were present. By applying an averaging operator, the ideal gas law relates average pressure, density and temperature using

$$\bar{p} = \bar{\rho}R\tilde{T} \tag{30}$$

where R is the specific gas constant and $\tilde{T}$ is the density averaged absolute temperature. If the flow is considered isentropic (assumed at the inlets), the speed of sound is written using Eq. (30) as

$$c = \sqrt{\gamma R\tilde{T}} \tag{31}$$

where γ is the ratio of specific heats. This leads to the definition of the Mach number, which is the ratio of flow velocity to the speed of sound:

$$M = \frac{u}{c} \tag{32}$$

2.6 Combustion Modeling

During combustion analyses, it is necessary to mathematically model the reaction between fuel and oxidizer. As a scramjet involves high-speed non-premixed combustion, the presence of turbulence is crucial to achieve adequate mixing for very short residence times. For this reason, the eddy dissipation model (EDM) was chosen. This model considers the rate of turbulent mixing of fuel and air (which is assumed to be slower than chemical reaction rates) to compute reaction rates at all locations in the flow for each time step. It is not inherently realistic, as it does not consider ignition sources or chemical kinetics (including production and consumption of radicals during reaction), and often overpredicts temperature in reacting regions. However, because of the aforementioned short flow residence time and necessity of proper mixing to achieve complete combustion, the EDM can be considered applicable to the cases in this study.

3 Computational Method

3.1 Computational Setup

The following software was used to setup, run, and process mixing and combustion analyses:

- Dassault Systèmes SolidWorks 2016 for geometry creation
- ANSYS Workbench 17.2 as the project interface
- ANSYS Meshing for mesh generation
- ANSYS CFX for setup and solver
- ANSYS CFD-Post for data collection
- MATLAB R2017a for data processing and plotting

3.2 Combustor Geometries

The combustor geometries used for this study are based on an experiment by Micka and Driscoll described in [3] involving a small-scale scramjet with a cavity flameholder. This study was chosen as a basis due to the simplicity of the engine's design. This simplicity allowed for new flameholder designs to be created and implemented in ANSYS by modifying the original geometry while maintaining a consistent computational domain size. The specific geometry for the square cavity flameholder described in [3] is shown in Fig. 1.

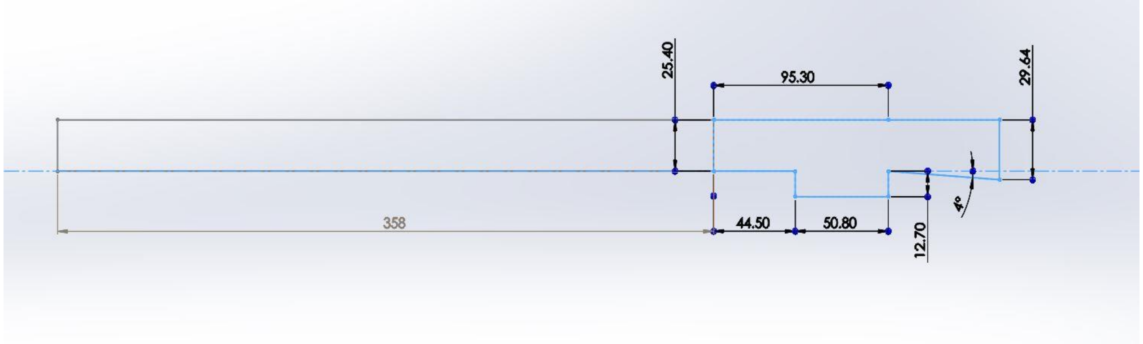

Figure 1 Square Cavity Geometry (all lengths in mm)

This engine model is comprised of a 358 mm long by 25.40 mm wide isolator which is followed by the combustor with a 50.80 mm wide by 12.70 mm deep cavity flameholder and a diverging nozzle with a 4° angle of deflection. The engine exhaust has a height of 29.64 mm, resulting in a nozzle length of 60.63 mm. The geometry was extruded to 2.667 mm to produce a quasi-2D simulation.

Two injector layouts were tested using this geometry. Both layouts involved a 1.50 mm diameter main fuel injector on the bottom wall of the exit of the isolator located 29 mm from the front edge of the cavity; this main injector is shown on the combustor section model in Fig. 2.

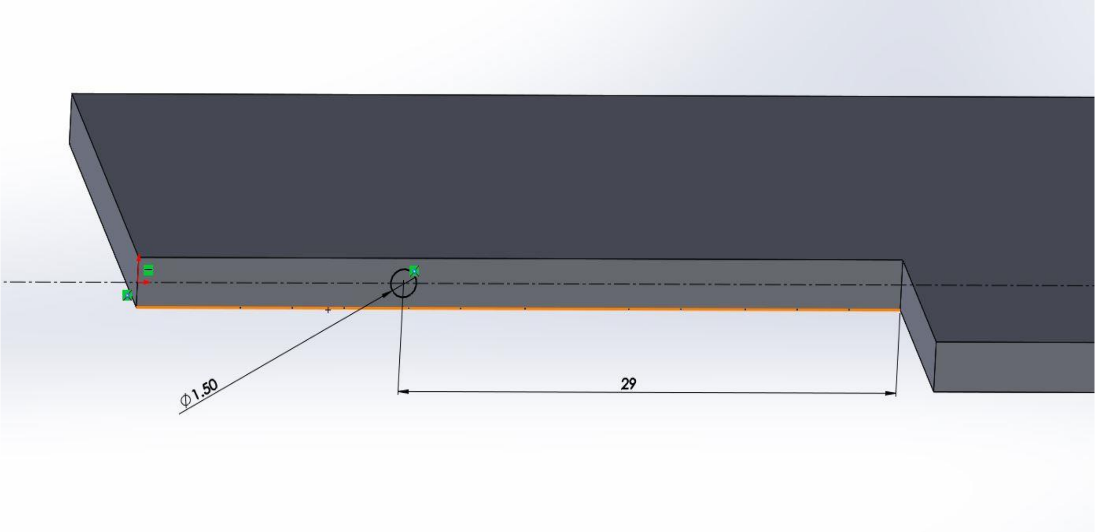

Figure 2 Square Cavity Main Injector (all units in mm)

This main injector was combined with a 1.50 mm diameter injector located at either the bottom of the cavity or on the back face of the cavity shown in Figs. 3 and 4.

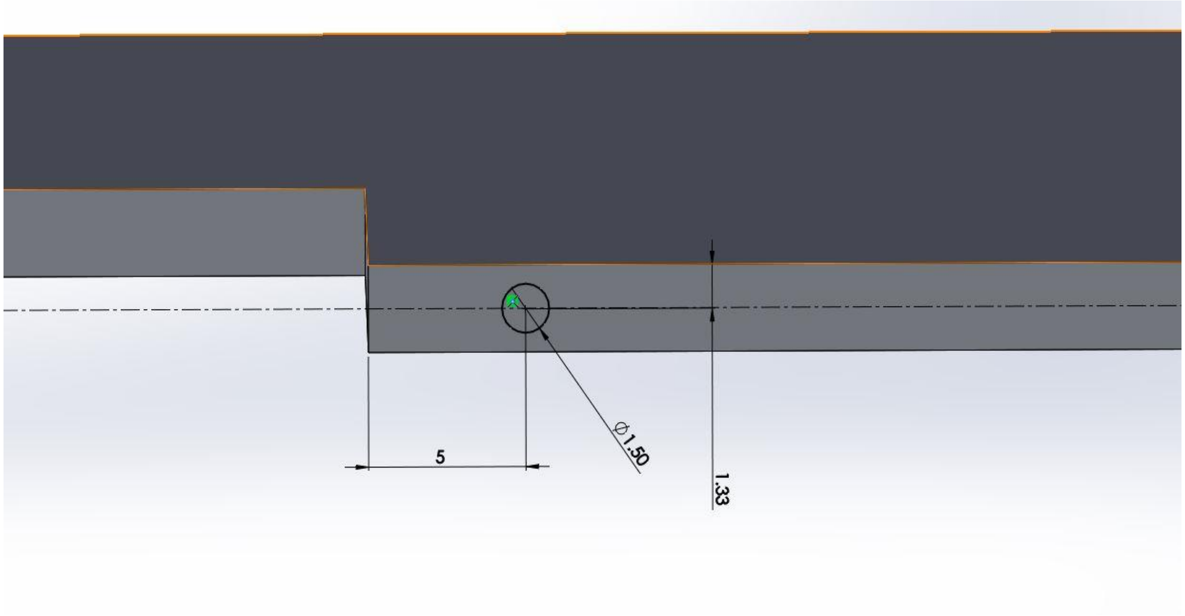

Figure 3 Bottom Cavity Injector (all units in mm)

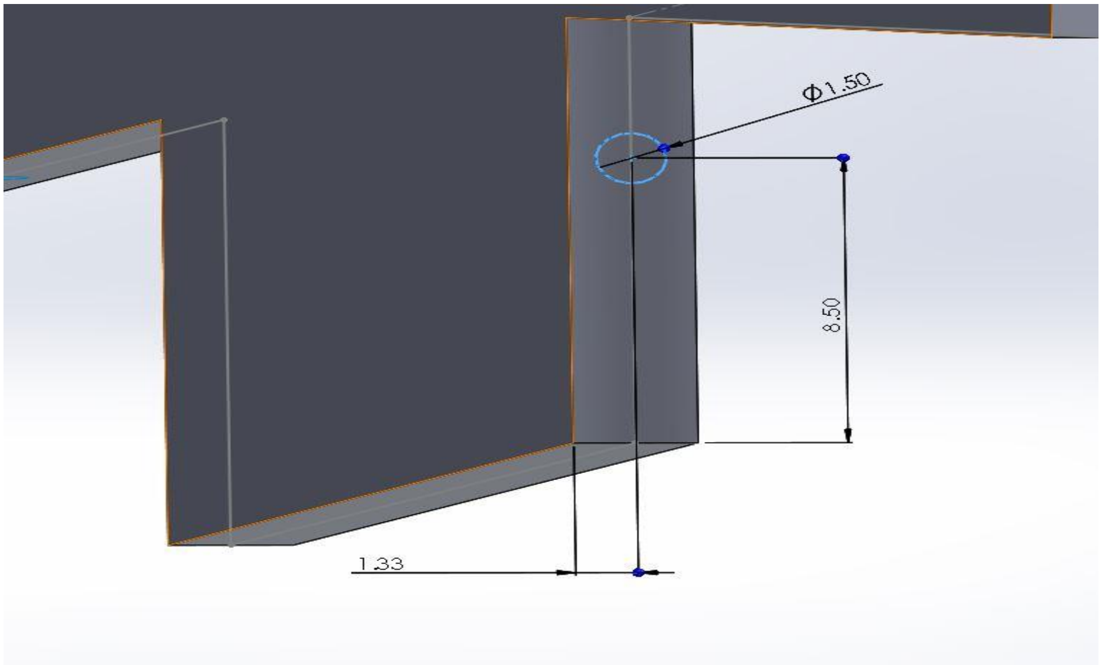

Figure 4 Back Cavity Injector (all units in mm)

Another commonly used flameholder design is a slanted cavity on the wall of the combustor. As the name suggests, the back wall is slanted at a given angle rather than perpendicular to the bottom face of the cavity; an example of this style of flameholder is seen in experiments by Ben-Yakar and Hanson in [4]. The geometry used for the slanted cavity in this study is shown in Fig. 5.

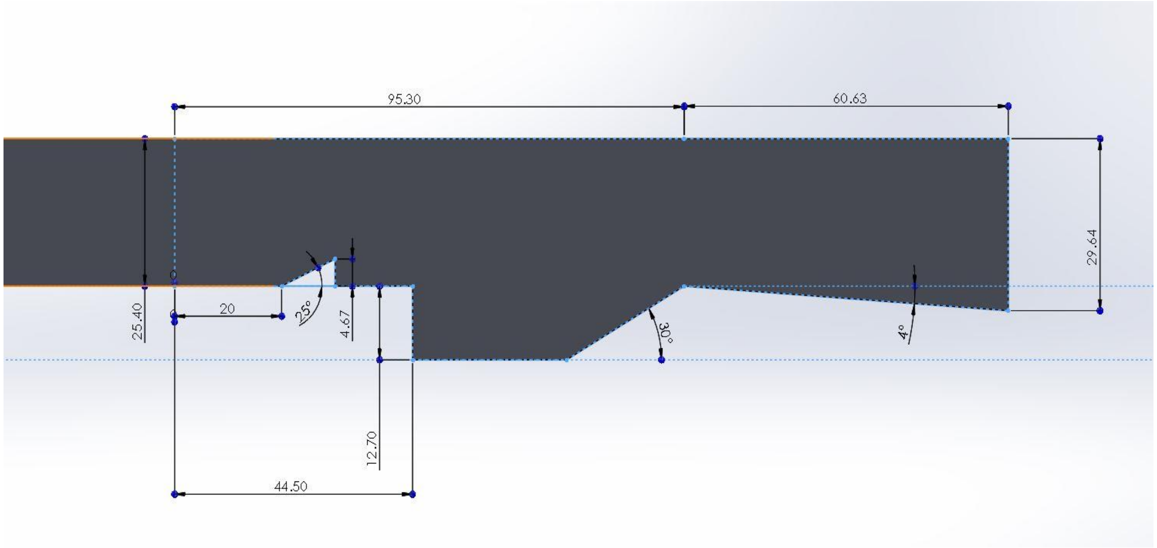

Figure 5 Slanted Cavity Geometry (all units in mm)

The back wall of the cavity was slanted to 30° relative to the horizontal while maintaining the distance between the start of the combustor and the back of the cavity of 95.30 mm. Compared to the square cavity design, the cavity depth of 12.70 mm, distance from combustor inlet to the front of the cavity of 44.50 mm, nozzle exit height of 29.64 mm (also nozzle length of 60.36 mm), isolator height of 25.40 mm, and nozzle angle of deflection of 4° were all kept constant. The only modification made to the square design, aside from the slanting of the cavity back wall, was the addition of a small 4.67 mm tall, 25° ramp prior to the cavity. This was used to house the main fuel inlet and also act as a method of promoting turbulent mixing through vortex generation. This geometry was also extruded to be 2.667 mm thick for quasi-2D simulation.

Several fuel injector layouts were used for the slanted cavity geometry. The most basic involves the main fuel injector on the ramp with a cavity inlet located on either the front face or bottom of the cavity. The locations of these injectors are shown in Figs. 6, 7, and 8.

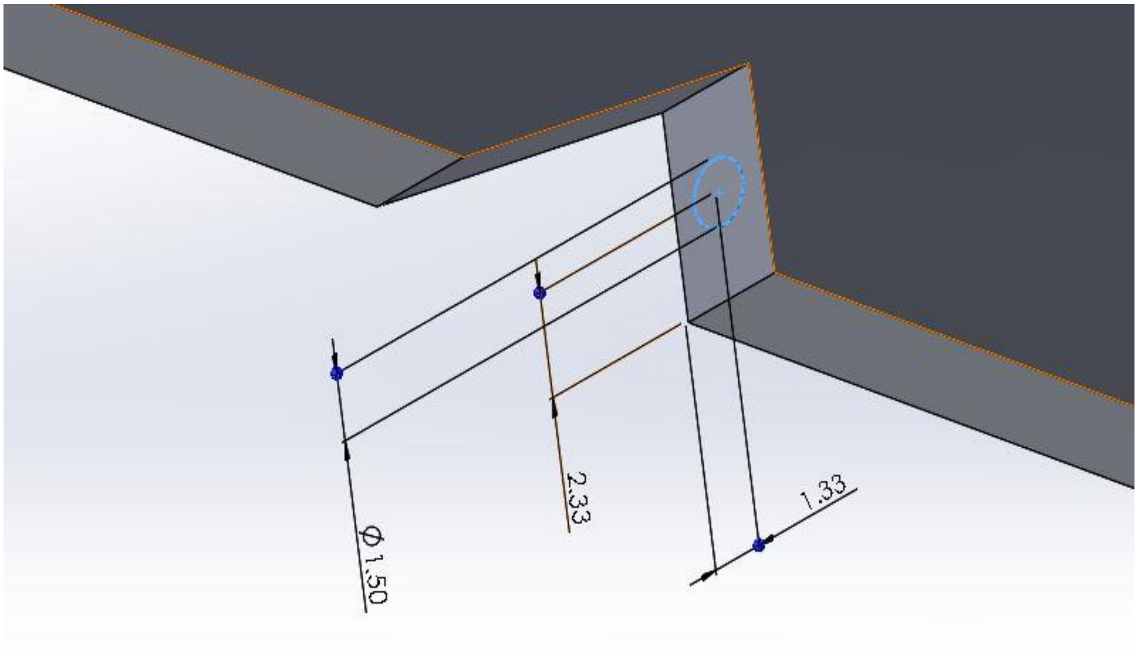

Figure 6 Main Inlet for Slanted Cavity (all units in mm)

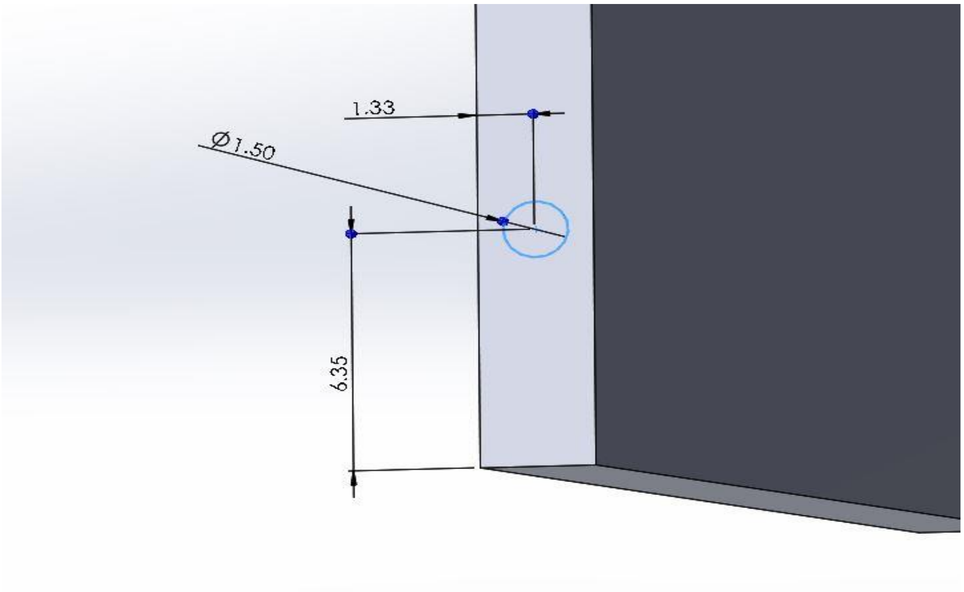

Figure 7 Front Inlet, Slanted Cavity (all units in mm)

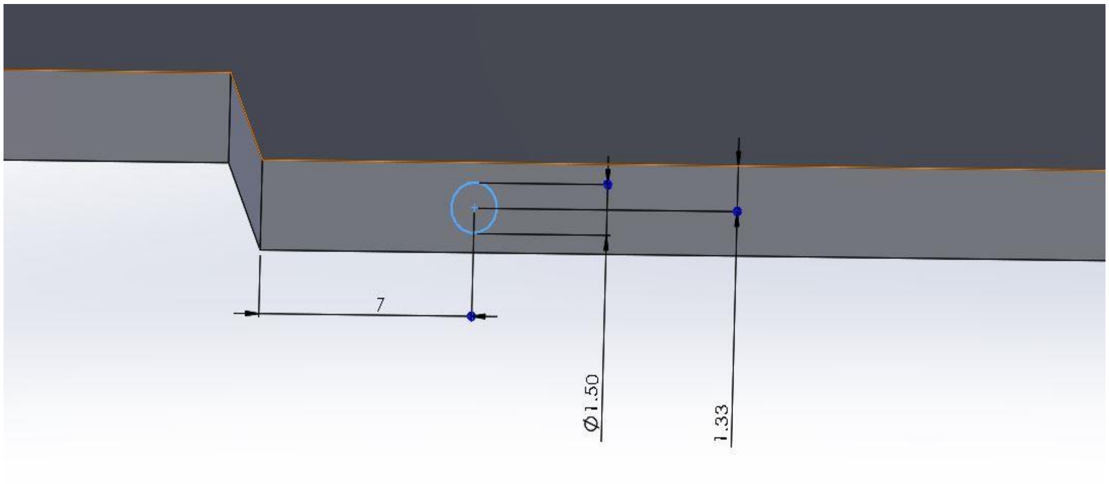

Figure 8 Bottom Inlet, Slanted Cavity (all units in mm)

Another injector layout involved the placement of a third injector on the top of the combustor wall to increase fuel penetration into the free-stream. The same geometry was used when including the third injector; however, the location of the main fuel injector shown in Fig. 6 was modified or removed for two of the three setups. A cavity inlet was placed on the bottom of the slanted cavity for all three of these new setups. The location of the top wall injector and the new placement of the main fuel inlet are shown in Figs. 9 and 10.

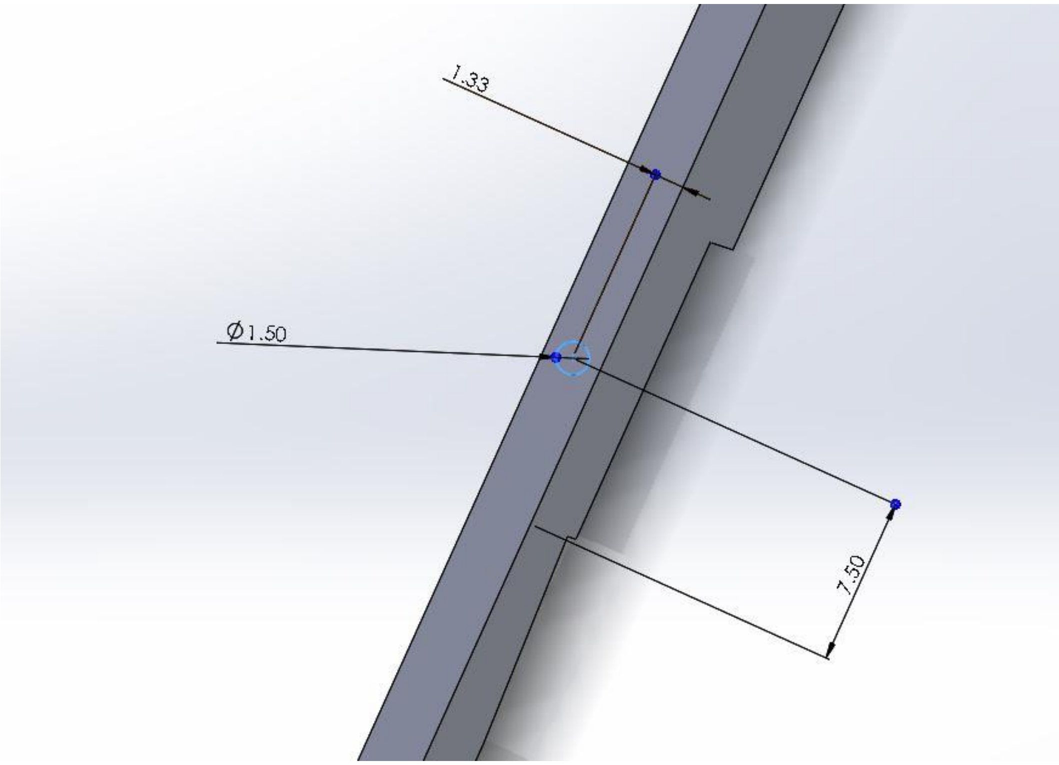

Figure 9 Top Injector Location (all units in mm)

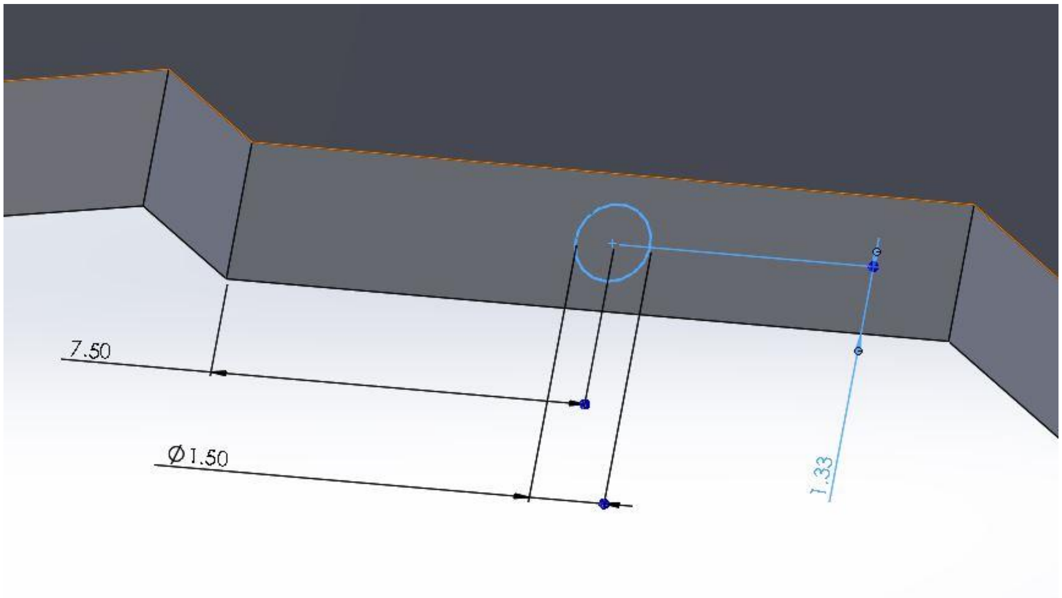

Figure 10 New Main Injector Location (all units in mm)

Each of these injectors is placed 7.50 mm from the end of the ramp and is 1.50 mm in diameter.

Although not as common in scramjet testing, the slanted cavity design can be mirrored about a central axis passing through the combustor; this results in a double cavity style design, which has been experimentally analyzed in [9]. The double cavity style design used for this study is shown in Fig. 11.

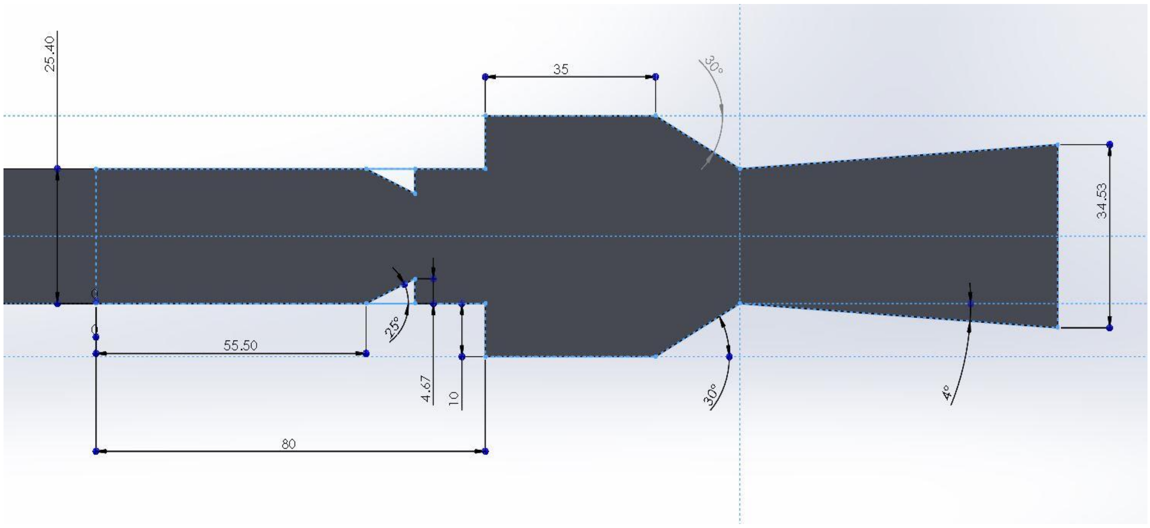

Figure 11 Double Cavity Geometry (all units in mm)

This design uses two identical cavities placed in parallel with the same 30° slanted back wall seen in the slanted cavity design; the 25° ramp was also mirrored across the central axis. Both sides of the nozzle are now diverging at a 4° angle, as opposed to the previous design in which only the bottom diverged, producing a nozzle exit which is 34.53 mm tall. The isolator remains the same height as the previous geometries, and the cavity depth was decreased to 10 mm. Like the other geometries, the domain was extruded to a thickness of 2.667 mm.

The fuel injector locations for this geometry are similar to the standard slanted cavity design; one of the two layouts places the main fuel injectors on the back face of the ramps, while the other places them on the face normal to the flow direction (see Fig. 10). Both layouts involve injectors on the bottom face of the cavities (in this case, bottom refers to the deepest wall) in the same location as is shown in Fig. 8. These locations are shown in Figs. 12 and 13.

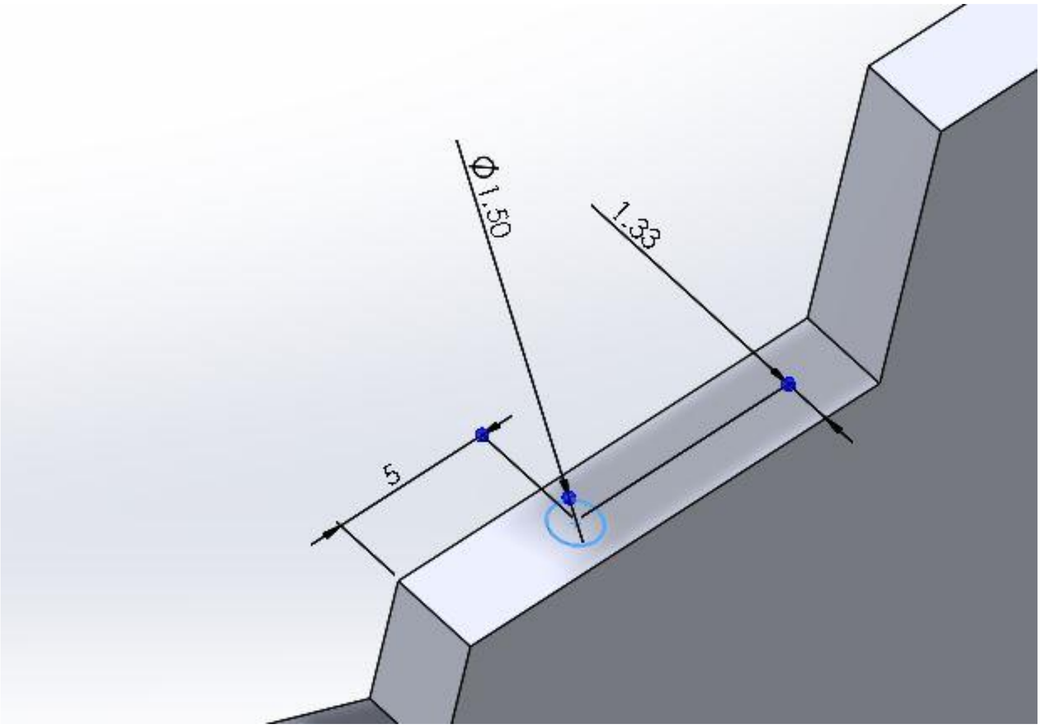

Figure 12 Double Cavity Normal Injector (all units in mm)

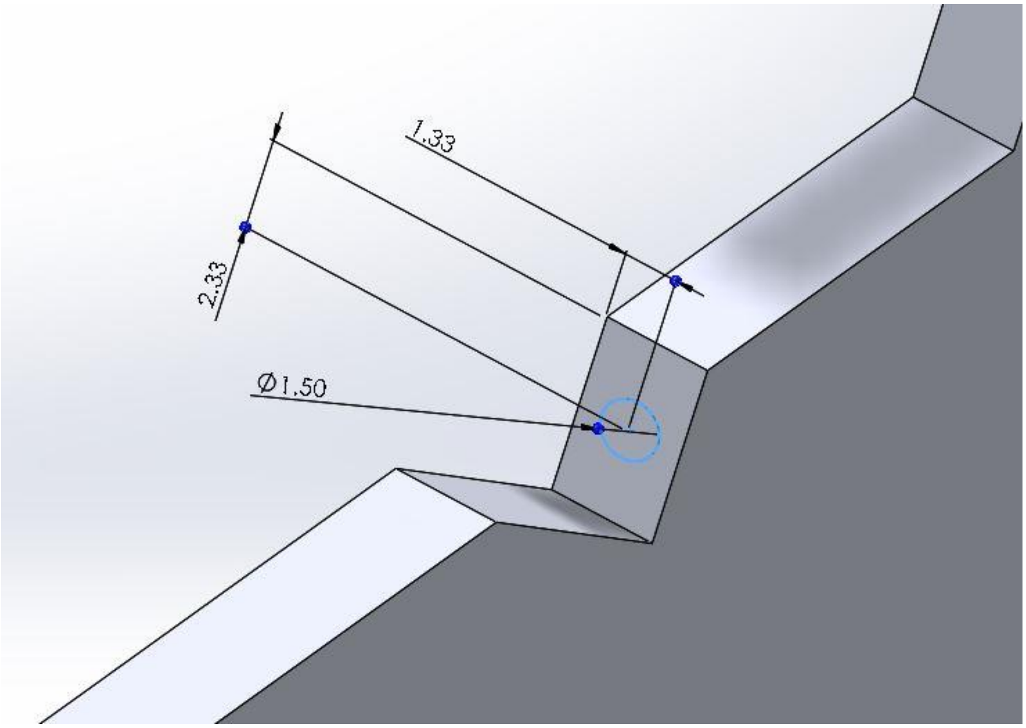

Figure 13 Double Cavity Parallel Injector (all units in mm)

The normal injector is placed 5 mm downstream of the back of the ramp on both top and bottom faces, while the parallel injector is placed in the middle of the back of each ramp.

The final geometry type investigated in this study involves the use of a central strut in the flow field along with a cavity flameholder. The general geometry of this setup is shown below in Fig. 14.

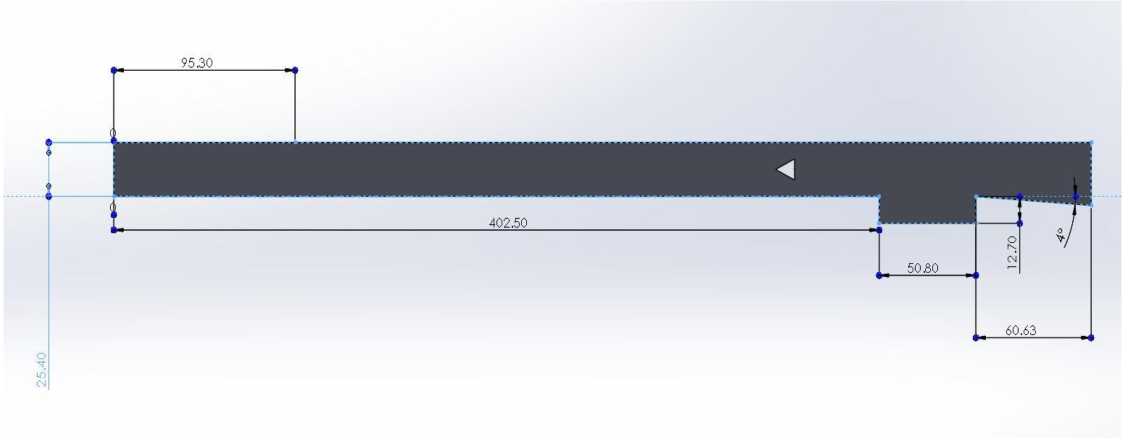

Figure 14 Strut-Cavity Geometry (all units in mm)

The geometry of the engine is the same as the standalone cavity flameholder setup shown in Fig. 1, including the extrusion thickness of 2.667 mm; the only major difference is the strut, which can be observed above as a triangular “cutout” of the domain. Nine separate strut sizes were analyzed in this study to observe the effects of geometry on mixing and combustion in ramjet and scramjet modes. The geometry of the 10 mm by 10 mm strut is shown in Fig. 15.

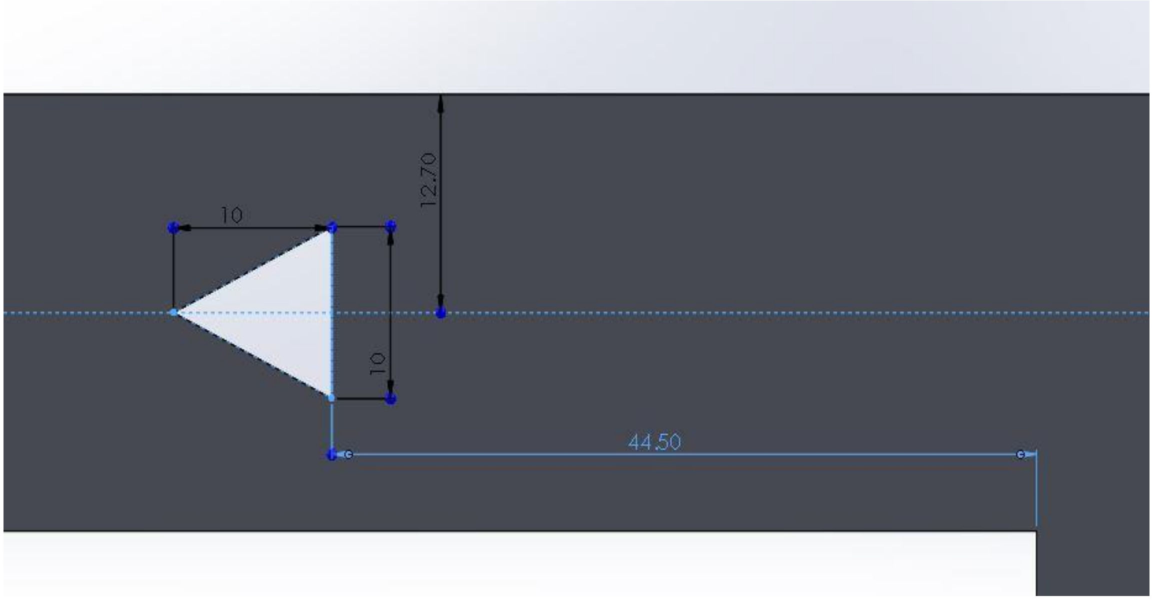

Figure 15 Strut Flameholder, 10 by 10 (all units in mm)

The strut is centered in the isolator and is placed such that its back face is 44.50 mm from the leading edge of the cavity. For the remainder of this paper, the general format when referring to the strut size will be *b* by *h*, where *b* is the base length of the strut, and *h* the height (or length) of the strut, both in millimeters. Three different base sizes, 7.17 mm, 10 mm, and 15 mm were tested with lengths of 10 mm, 15 mm, and 20 mm.

Two injectors are used for the strut-cavity setup. One injector is located on the bottom of the cavity, and is identical in placement to the one shown in Fig. 3. The main fuel injector is placed in the center of the back face of the strut for all strut sizes; this is shown for the 10 by 10 strut in Fig. 16.

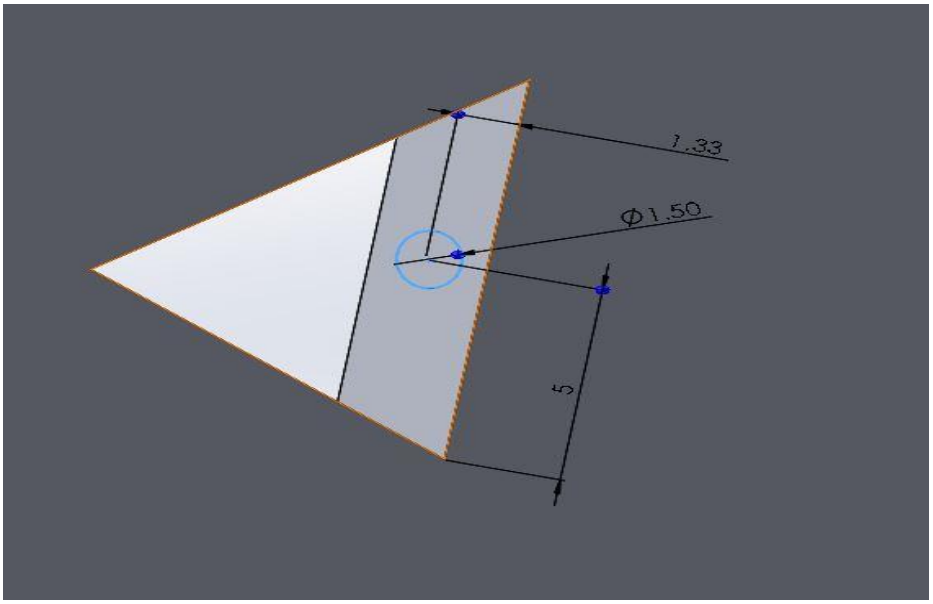

Figure 16 Strut Fuel Injector, 10 by 10

3.3 Meshing

For the mixing analyses at M = 2.2 and combustion analyses at variable Mach number, an unstructured tetrahedral mesh was used in the freestream region with inflation layers near walls to capture the boundary layer. Although a tetrahedral mesh is not as computationally robust as a hexahedral mesh, it is far less computationally expensive and is not inherently poor as long as steps are taken to ensure high mesh quality. In the following table, the mesh used in each of the geometries is outlined regarding sizing and inflation layer specifications.

Flameholder	No. of Nodes	No. of Elements	Inflation Layer
Square Cavity	612,543	2,684,905	10 layers, 1 mm
Slanted Cavity	608,871	2,650,331	10 layers, 1 mm
Double Cavity	634,683	2,783,576	10 layers, 1 mm
Strut – 10 by 10	765,312	2,939,355	20 layers, 1 mm
Strut – 10 by 15	766,358	2,935,512	20 layers, 1 mm
Strut – 10 by 20	767,936	2,933,684	20 layers, 1 mm
Strut – 15 by 10	273,587	924,107	20 layers, 1 mm
Strut – 15 by 15	766,266	2,931,204	20 layers, 1 mm
Strut – 15 by 20	767,057	2,925,447	20 layers, 1 mm
Strut – 7.17 by 10	765,535	2,941,124	20 layers, 1 mm
Strut – 7.17 by 15	767,397	2,939,374	20 layers, 1 mm
Strut – 7.17 by 20	769,282	2,939,947	20 layers, 1 mm

Table 1 Tet Mesh Specifications for Mixing and Combustion

There is an apparent outlier in the meshing parameters shown above; the strut-cavity configuration with a 15 mm by 10 mm strut has far fewer elements than all of the others, which average around 2.85 million elements per mesh. This was due to several instabilities that arose while trying to achieve a converged solution when using the 15 by 10 strut-cavity, leading to a simulation that diverged. For this reason, this mesh was coarsened to allow for a converged solution to exist; the results obtained from this geometry, which are shown later, do not appear to be contradictory to expected flow behavior.

Figures 17 through 20 are images of some of the meshes described in Table 1.

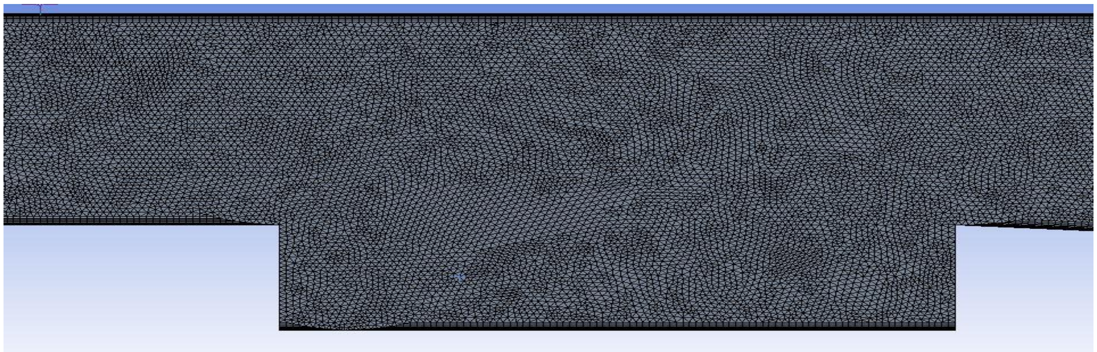

Figure 17 Square Cavity Tet Mesh

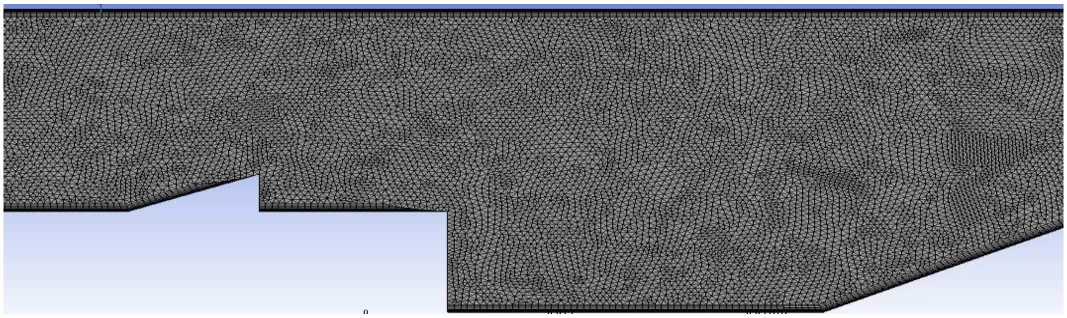

Figure 18 Slanted Cavity Tet Mesh

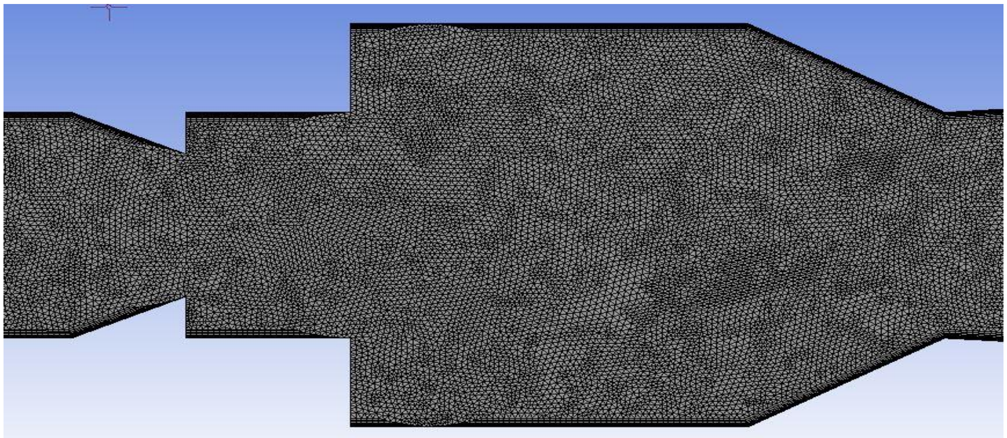

Figure 19 Double Cavity Tet Mesh

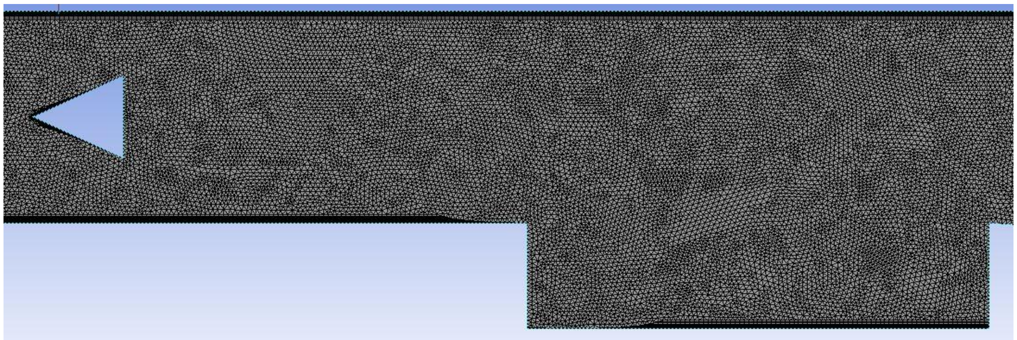

Figure 20 10 by 10 Strut-Cavity Tet Mesh

3.4 Initialization and Boundary Conditions

For all mixing simulations at M = 2.2, the boundary conditions and initializations used were based on those prescribed by Micka and Driscoll in [3]. These are:

- Inlet air heated to 450 K at M = 2.2 (935.5 m/s using Eq. (31)) at atmospheric pressure of 101,325 Pa with an O_2 mass fraction of 0.233
- Pure hydrogen fuel at room temperature, 298 K, injected sonically at 1311.7 m/s
- Outlet at atmospheric pressure of 101,325 Pa, averaged over entire opening
- No-slip, adiabatic wall condition on all solid surfaces
- Periodic boundary conditions placed on faces in the spanwise direction
- Initialization using u = 935.5 m/s, v = 0, w = 0, p = 101,325 Pa, T = 450 K, O_2 mass fraction of 0.233
- Stationary flow

All combustion analyses at variable Mach number had identical boundary conditions, albeit with the inlet velocity and Mach number changed to their corresponding values for T_{inlet} = 450 K.

4 Results and Analysis

4.1 Non-Reacting Simulations at M = 2.2

4.1.1 Effects of Flameholder on Non-Reacting Flow Field

To understand the general behavior of the fluid in the isolator and combustor as a result of the flameholders, the non-reacting cases run at a Mach number of M = 2.2 were analyzed using the relative pressure contours and velocity vector fields of the fluid. The pressure contours generated at this Mach number for the non-reacting case are shown in Figs. 21-27.

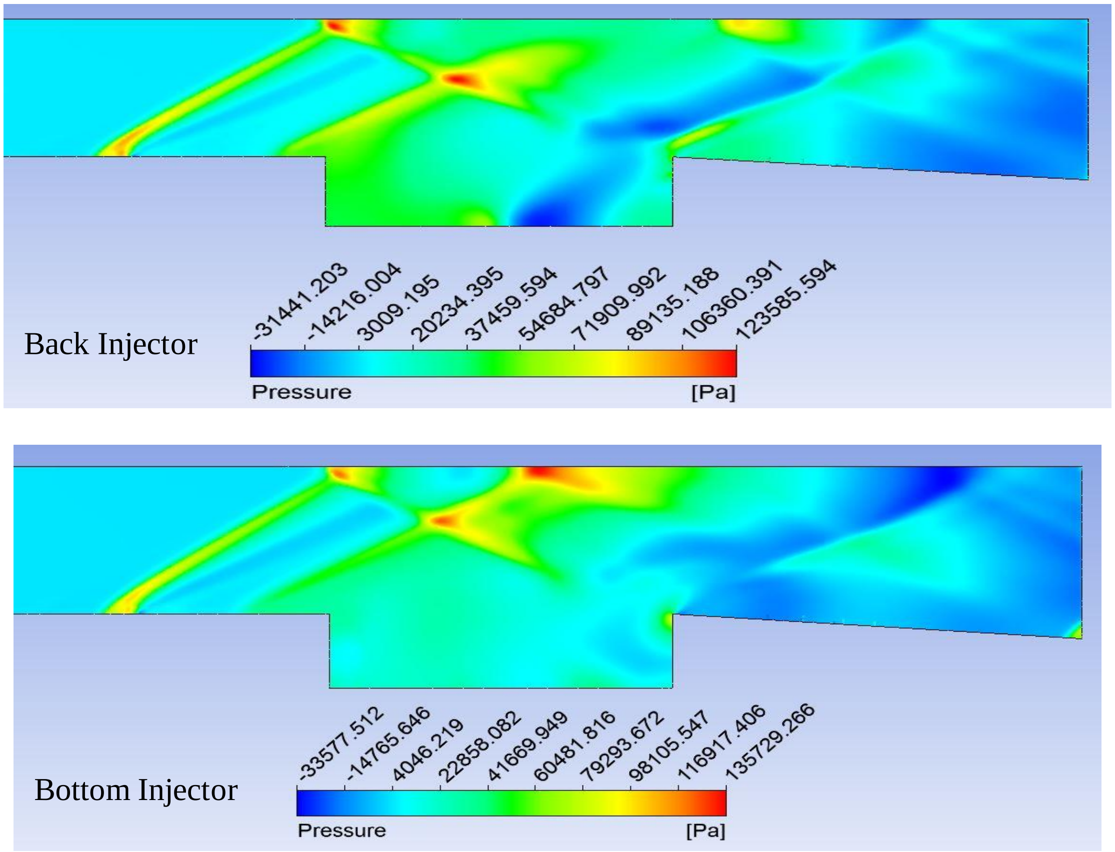

Figure 21 Square Cavity Non-Reacting Pressure

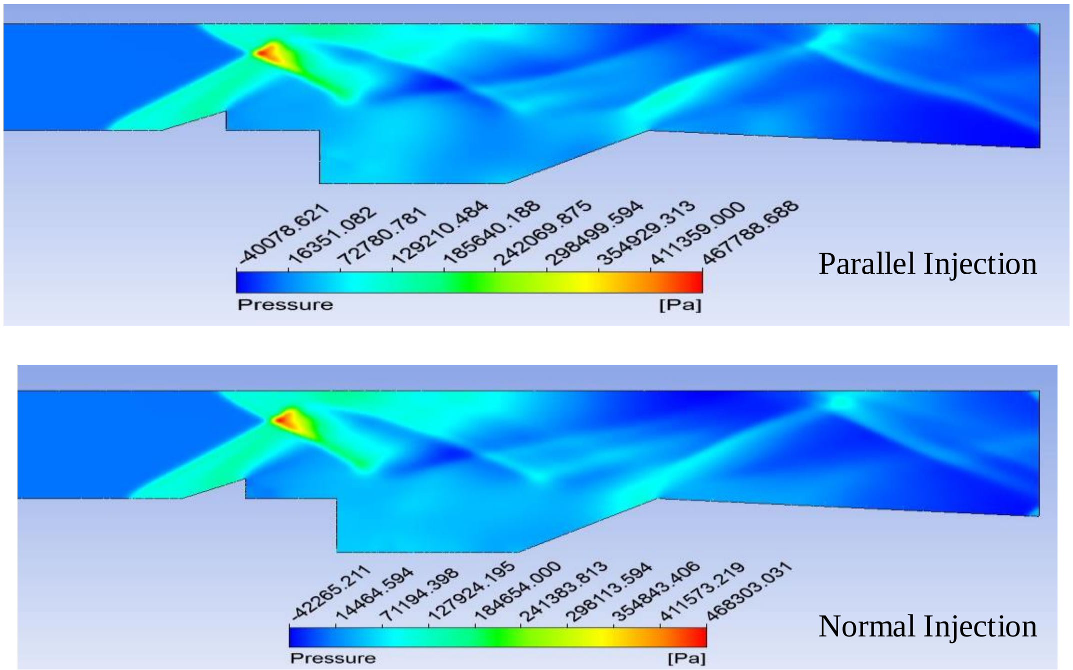

Figure 22 Slanted Cavity Non-Reacting Pressure

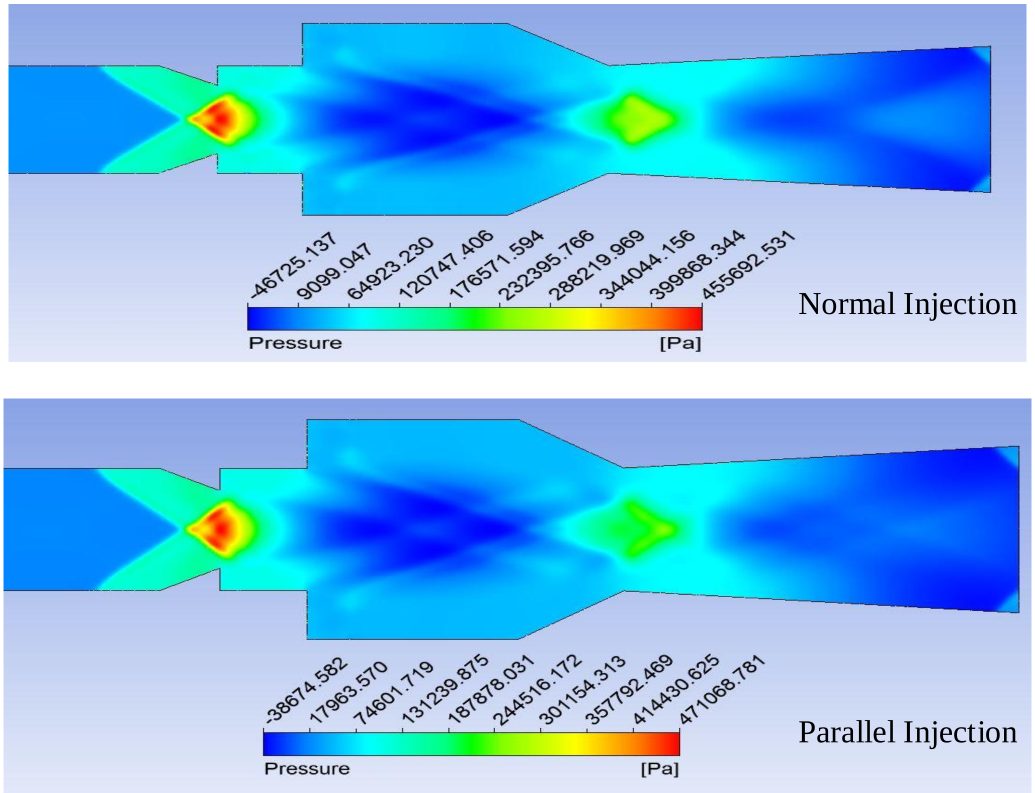

Figure 23 Double Cavity Non-Reacting Pressure

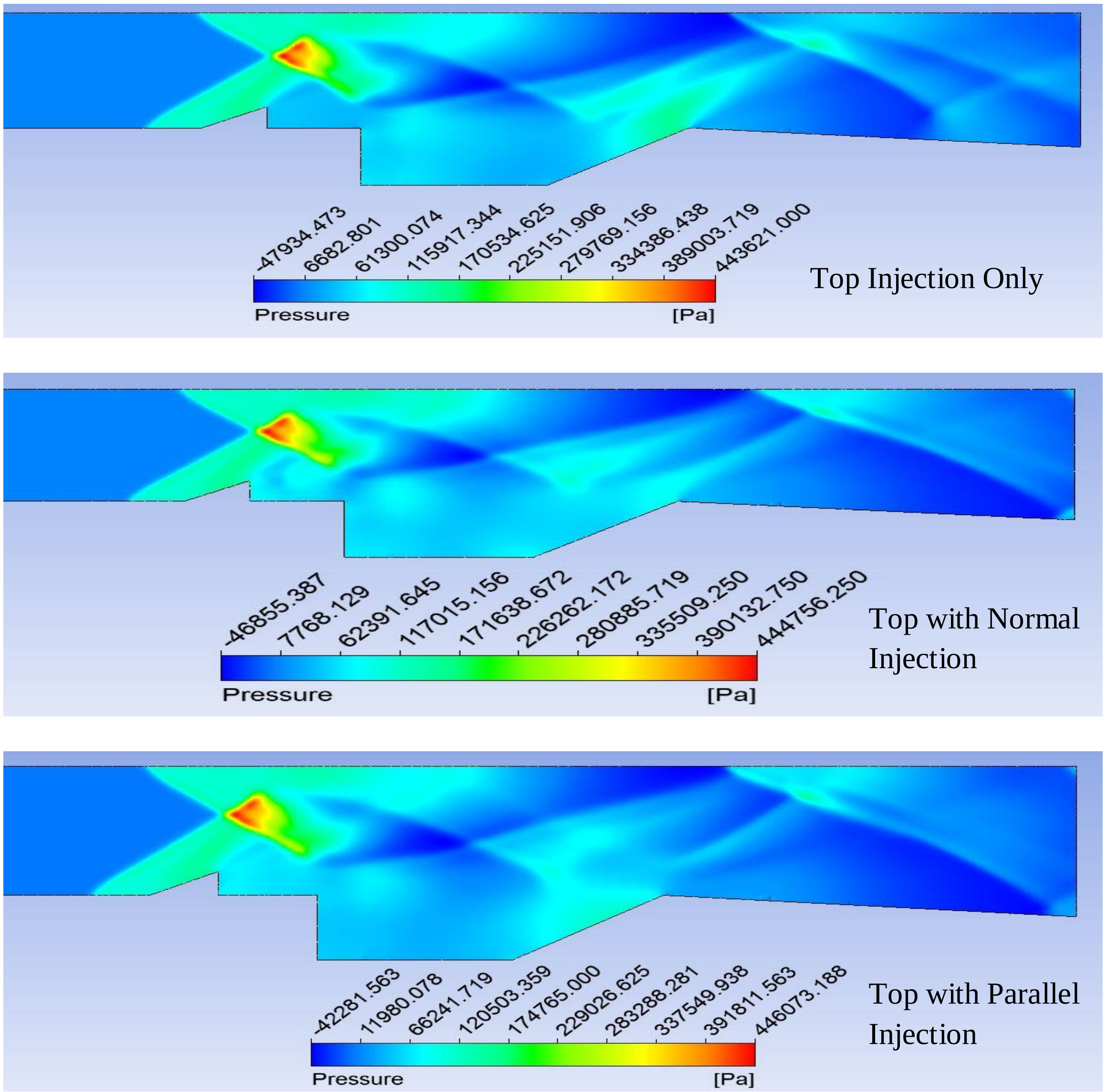

Figure 24 Slanted Cavity with Top Injector Non-Reacting Pressure

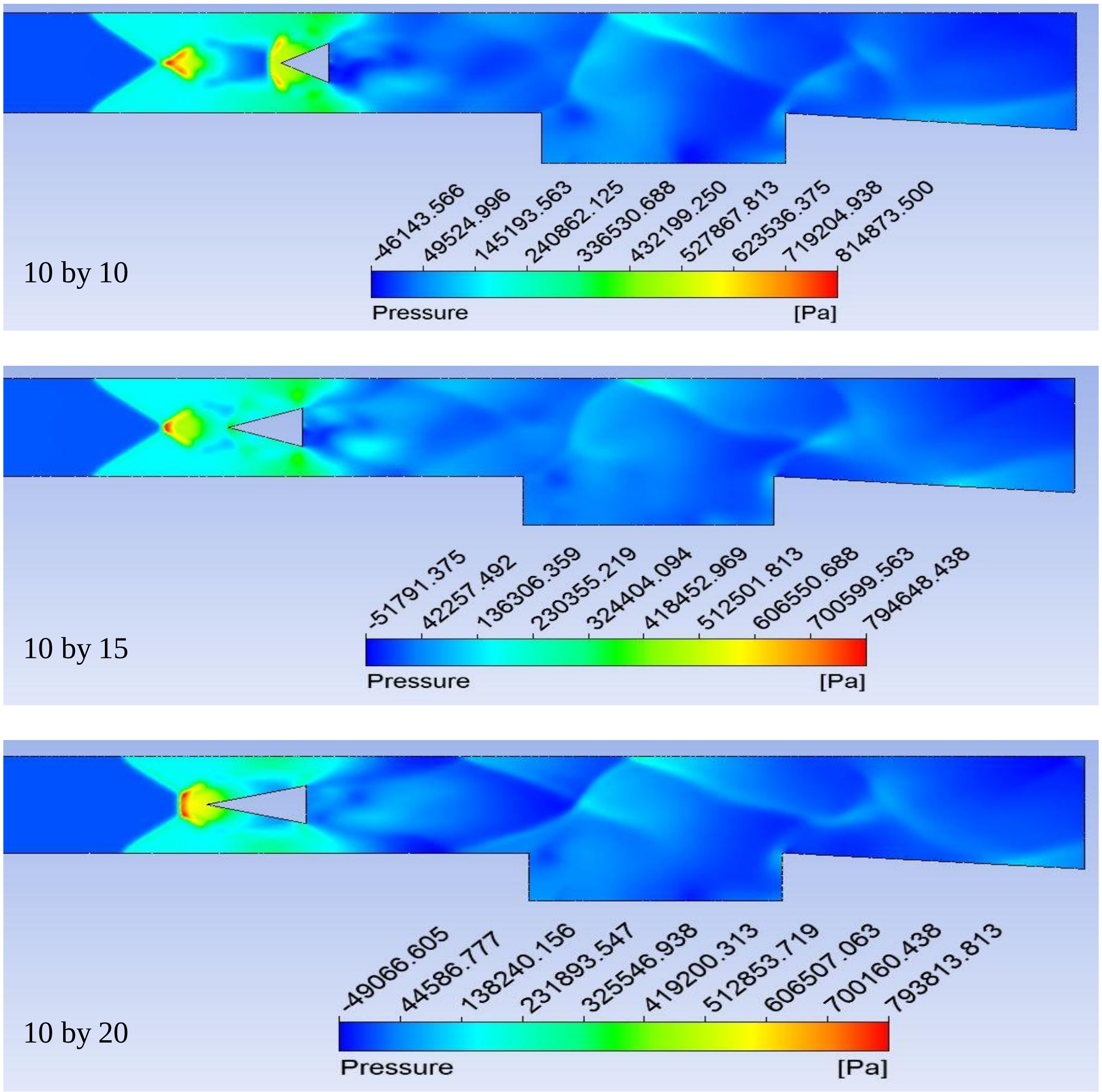

Figure 25 10 mm Strut-Cavity Non-Reacting Pressure

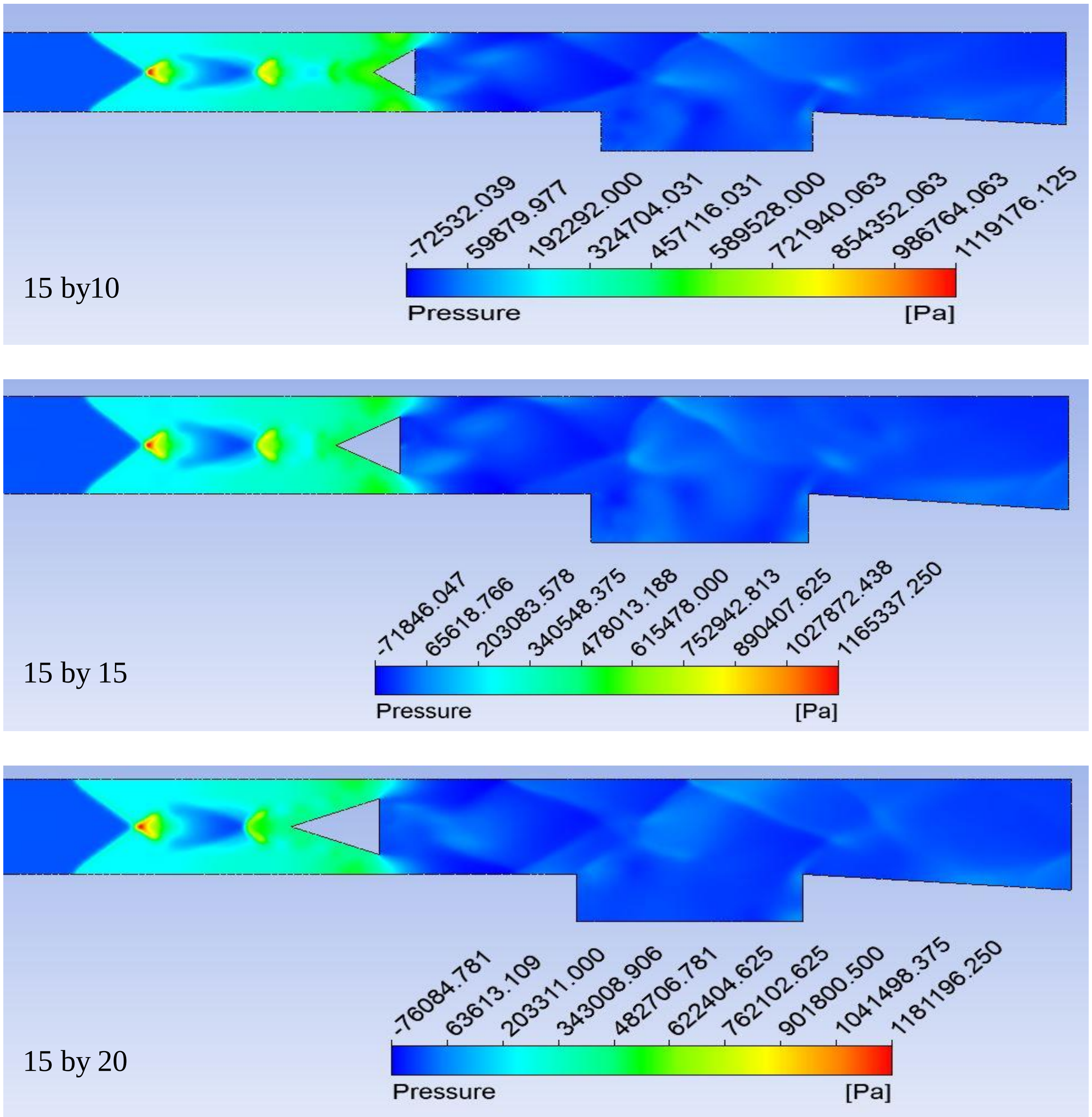

Figure 26 15 mm Strut-Cavity Non-Reacting Pressure

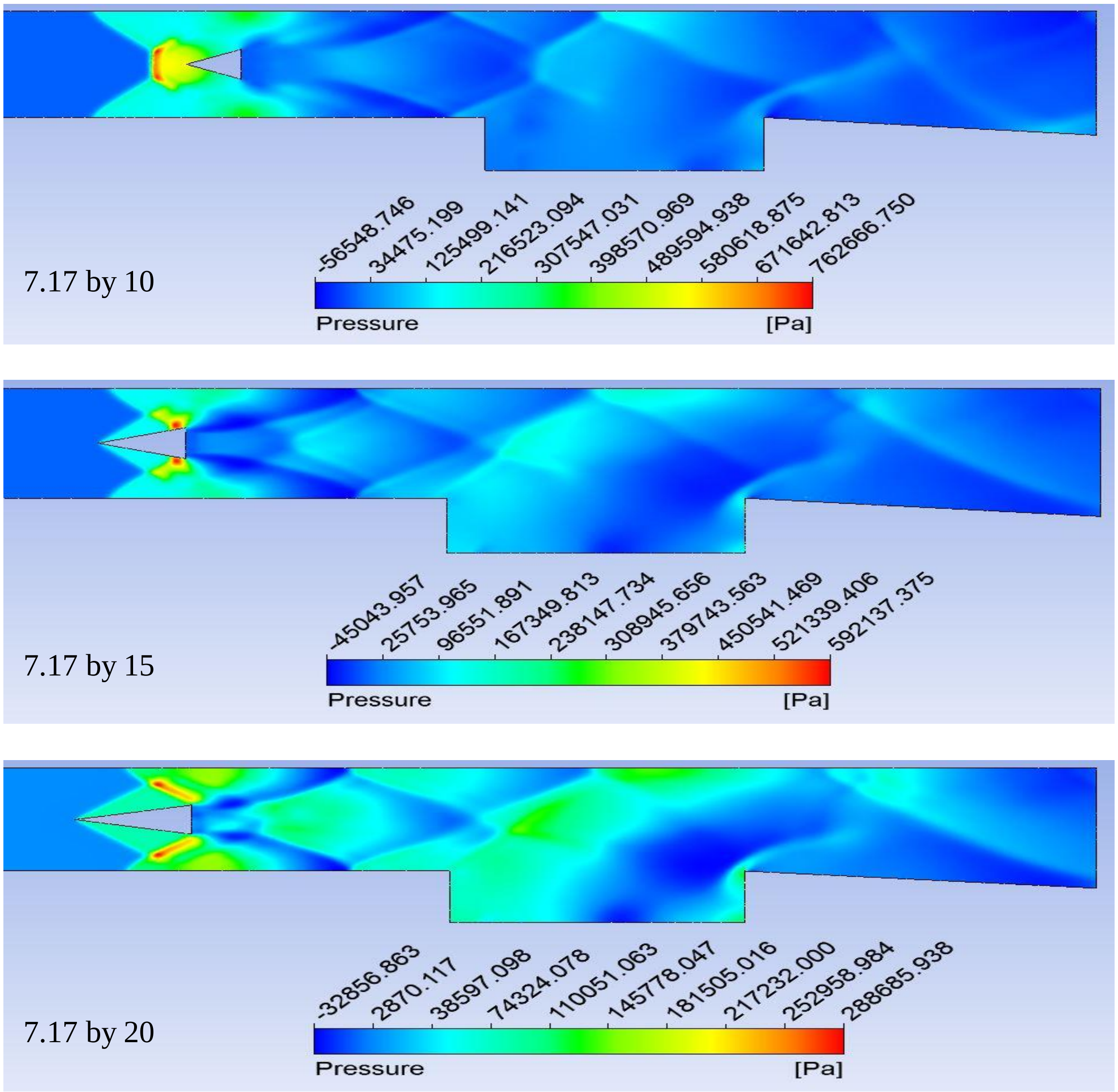

Figure 27 7.17 mm Strut-Cavity Non-Reacting Pressure

From these contour plots, it is apparent that oblique shock waves are generated within the engine as a result of the flameholders and the fuel injectors in the isolator and combustor. The strength and location of these shocks appears to be dependent on the type of flameholder used, as well as the location of the fuel injectors. For example, in the square cavity cases in Fig. 21, three shocks are attached to the bottom wall of the isolator.

The first of these shocks is due to the main fuel injector, which causes an oblique shock and results in minor boundary layer separation; this wave also reflects off of the top wall of the combustor and extends slightly past the centerline. The second shock is attached near the front wall of the cavity and is a result of cavity fueling, which results in further flow separation. The final shock is attached to the back face of the cavity as the flow enters the nozzle, and is a result of sudden flow reattachment [16]. Similar shock patterns, including reflections, are observed in the other geometries in both the combustor and isolator due to fuel injection along the wall or sudden changes in geometry. These changes include the ramps in the slanted and double cavity designs, the nozzle entrance, or the strut in the middle of the flow field in the strut-cavity designs. It is also noteworthy that the change in injection scheme for the slanted cavity, the double cavity, and the slanted cavity with the additional inlet on the top of the combustor had little to no effect on the location of shocks or general pressure distribution inside of the engine.

While shocks are detrimental to the stagnation pressure of the flow due to an increase in entropy, they can be beneficial for mixing through boundary layer separation. The shock-driven flow separation often results in subsonic vortices which enhance the rate of fuel and air mixing, thereby improving the stability of combustion inside of the engine [16]. The benefit of using shocks to enhance mixing does not come without penalty, especially when analyzing reacting flows. A shock that is too strong or too close to the inlet may eventually lead to engine unstart, in which case air is not delivered uniformly to the combustor and thrust drops severely. This must be considered during the design of a ramjet or scramjet engine, and will be discussed further when analyzing the reacting cases.

The creation of shocks by the flameholders is not the only way in which they improve mixing; the use of a cavity or strut also tends to create a recirculation zone or vortex where fuel and air mix prior to ignition. This creates a region where a flame is able to be anchored during sustained combustion, preventing blowout. The vortices created by the flameholders are shown in Figs. 28-31.

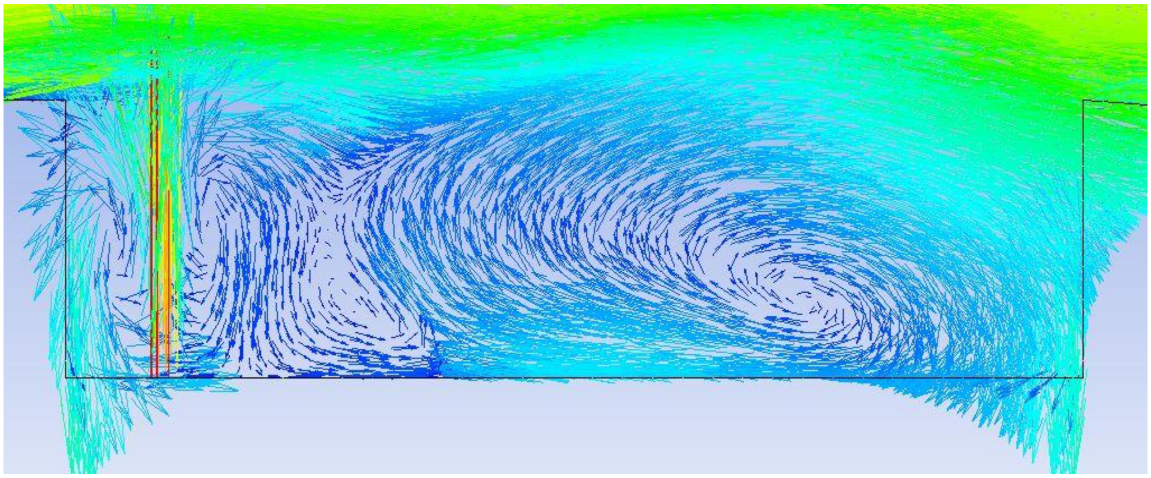

Figure 28 Square Cavity Flameholder Vortex

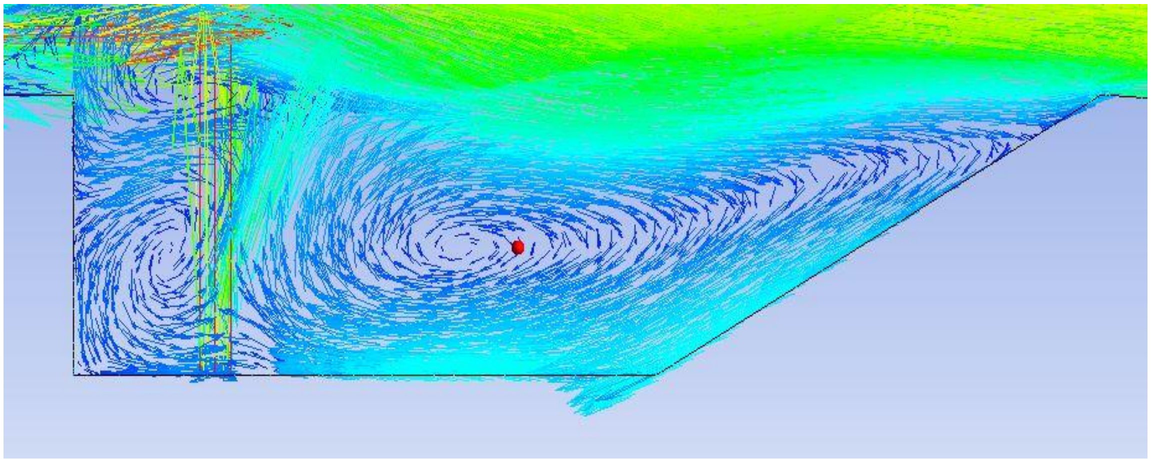

Figure 29 Slanted Cavity Flameholder Vortex

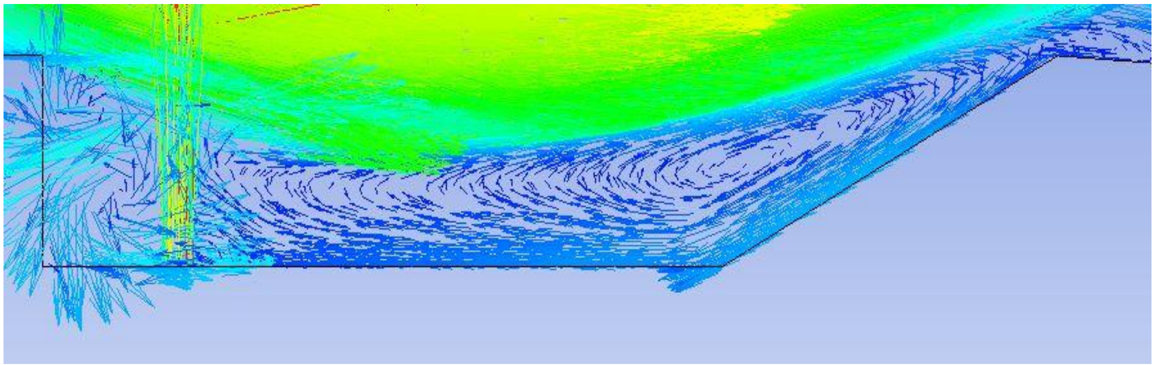

Figure 30 Double Cavity Flameholder Vortex

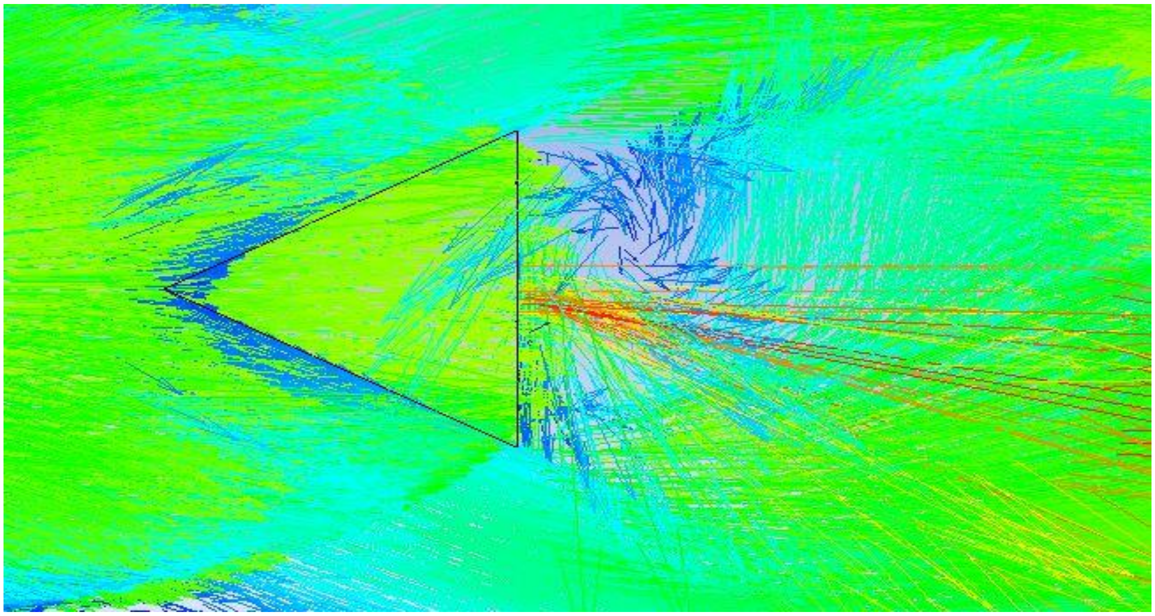

Figure 31 10 by 10 Strut Flameholder Vortex

Each of the flameholder designs generates a vortex in which the aforementioned mixing and flame anchoring can occur. The cavity vortices are well defined in structure, and rotate with the direction of flow (in this case, clockwise), while the strut vortex is less easily discernable and does not have a definitive direction. The rotation of the cavity vortices carries fuel and radicals from the bottom of the cavity towards the freestream, which further aids in both mixing and combustion stability in the cavity shear layer. The vortices created by the strut will accelerate the turbulent mixing of fuel from the main inlet in the freestream, with the potential of anchoring a flame in the shear layers generated along the top and bottom of the strut. To gauge the ability of flameholders to promote mixing, a metric known as the mixing efficiency was calculated for each design in a non-reacting flow at M = 2.2.

4.1.2 Mixing Efficiency

The mixing efficiency in a combustor can be defined using the ratio of the reacting mass flow rate of fuel to the actual mass flow rate of fuel at a given cross-section. In equation form, this is written as

$$\eta_M = \frac{\int Y_{R,H_2} \rho u dA}{\int Y_{H_2} \rho u dA} \tag{33}$$

where Y_{H_2} is the mass fraction of hydrogen, Y_{R,H_2} is the reacting mass fraction of hydrogen, and A is the area of the cross-section being considered [5]. The reacting mass fraction is calculated using

$$Y_{R,H_2} = \begin{cases} Y_{H_2} & \text{if } Y_{H_2} \leq Y_s \\ Y_s(1 - Y_{H_2})/(1 - Y_s) & \text{if } Y_{H_2} > Y_s \end{cases} \tag{34}$$

where Y_s is the stoichiometric mass fraction of the fuel [5]. As the oxygen mass fraction for this study was prescribed as 0.233 and the stoichiometric air to fuel ratio (AFR) for hydrogen is 34.33:1, the stoichiometric mass fraction of fuel is 0.0283 [17]. This parameter was calculated across 15 individual planes normal to the flow direction for each of the combustor designs and plotted as a function of a non-dimensionalized distance from the main fuel inlet, x^*, which is defined for each plane as

$$x^* = x/H \tag{35}$$

Here, x is the plane's distance downstream from the main fuel inlet and H is the height of the air inlet (25.4 mm). The use of this variable allows for a direct comparison to be made, as the distance from the main fuel inlet to the outlet is not the same for all cases. An image of the planes used to calculate mixing efficiency, as well as the resulting plots of this metric as a function of x^* are shown in Figs. 32-39.

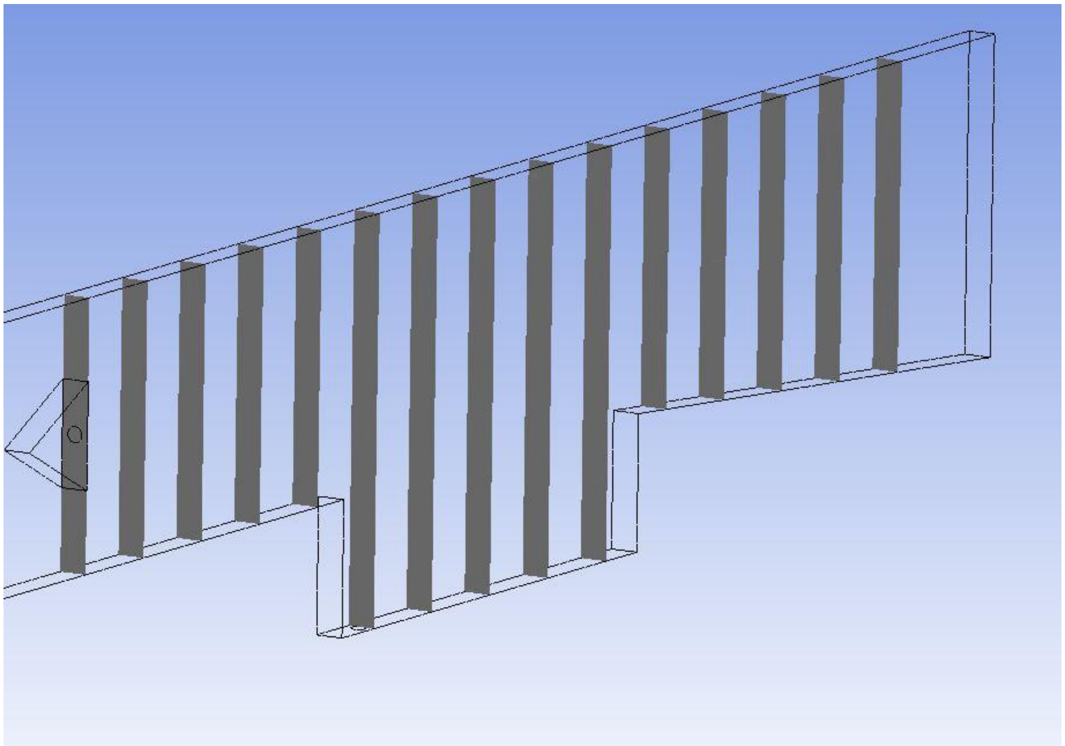

Figure 32 Combustor Mixing Planes on 10 by 10 Strut-Cavity

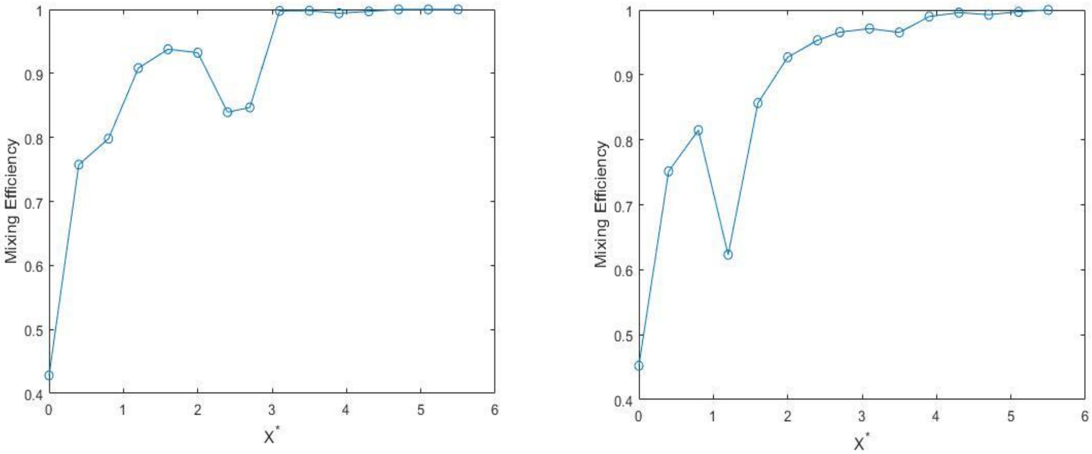

(b) Back Injection

(a) Bottom Injection

Figure 33 Square Cavity Mixing Efficiencies

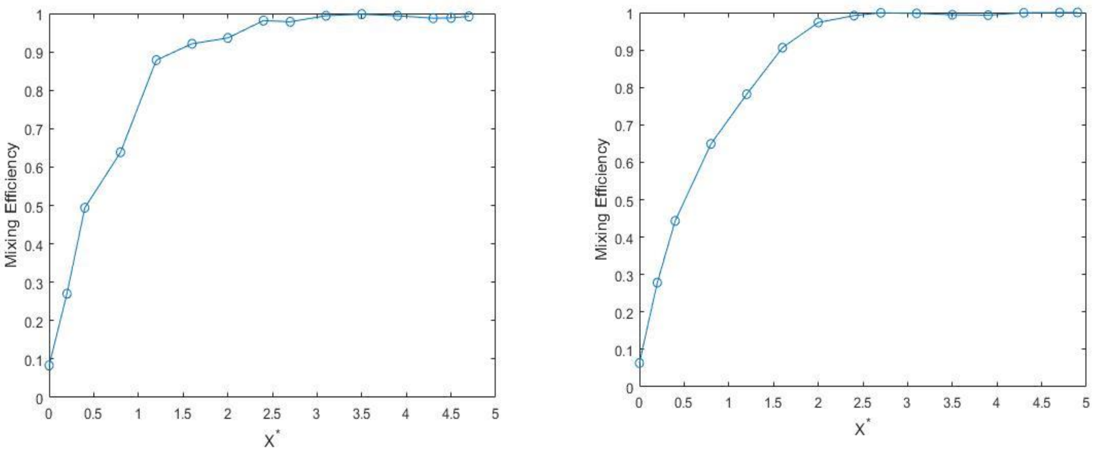

(a) Normal Injection

(b) Parallel Injection

Figure 34 Slanted Cavity Mixing Efficiencies

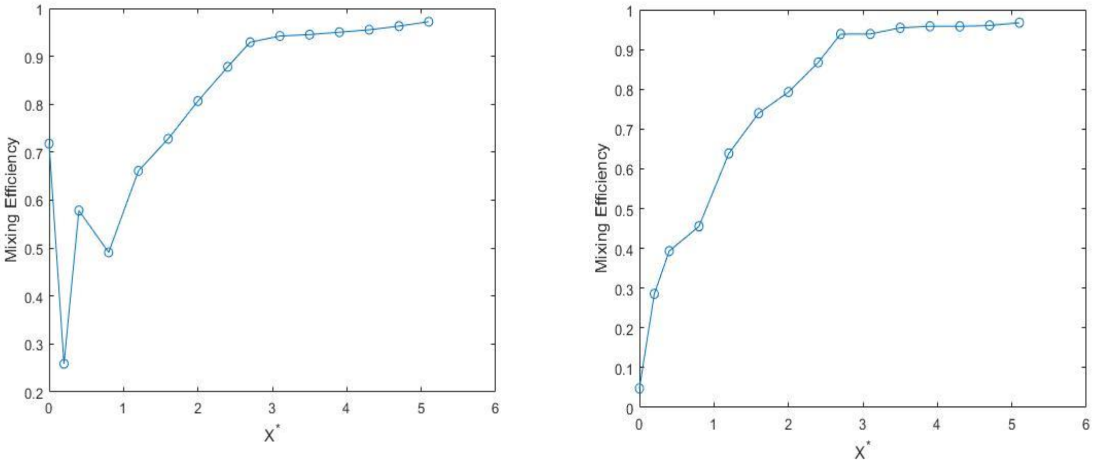

(a) Normal Injection

(b) Parallel Injection

Figure 35 Double Cavity Mixing Efficiencies

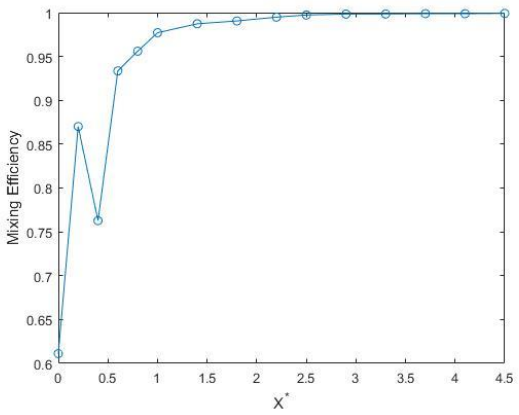

(a) Top Injector Only

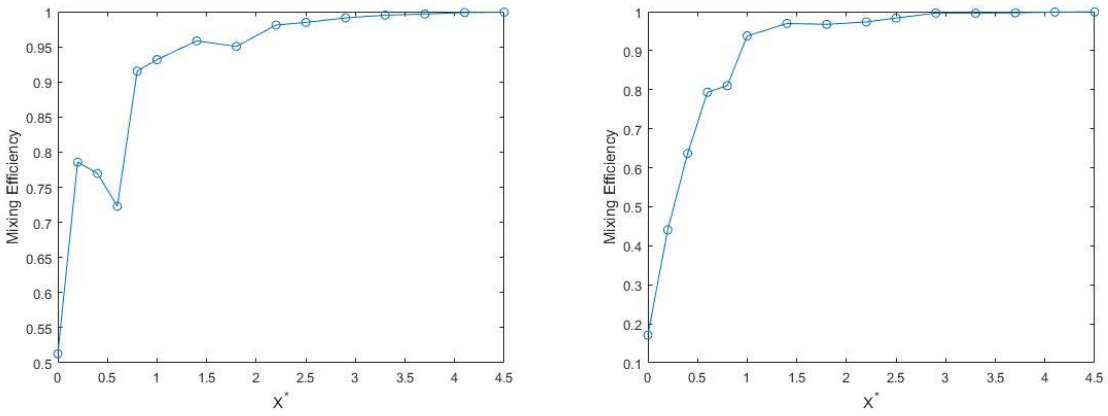

(b) Top with Normal Injection (c) Top with Parallel Injection

Figure 36 Slanted Cavity with Top Injector Mixing Efficiencies

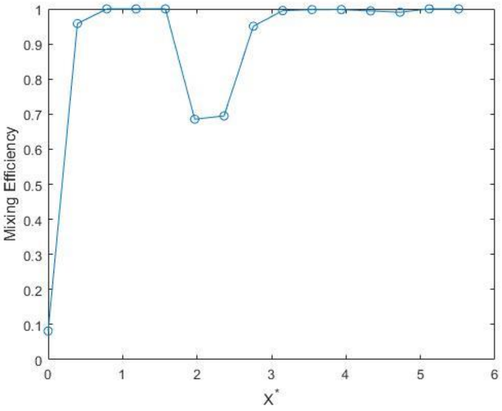

(a) 10 by 10

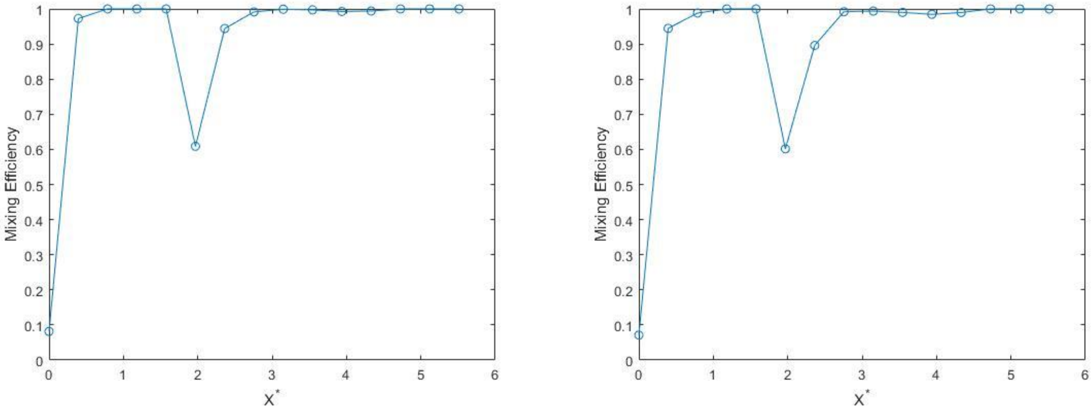

(b) 10 by 15 (c) 10 by 20

Figure 37 10 mm Strut-Cavity Mixing Efficiencies

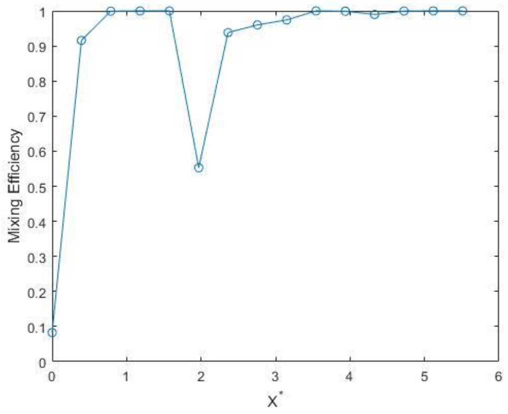

(a) 15 by 10

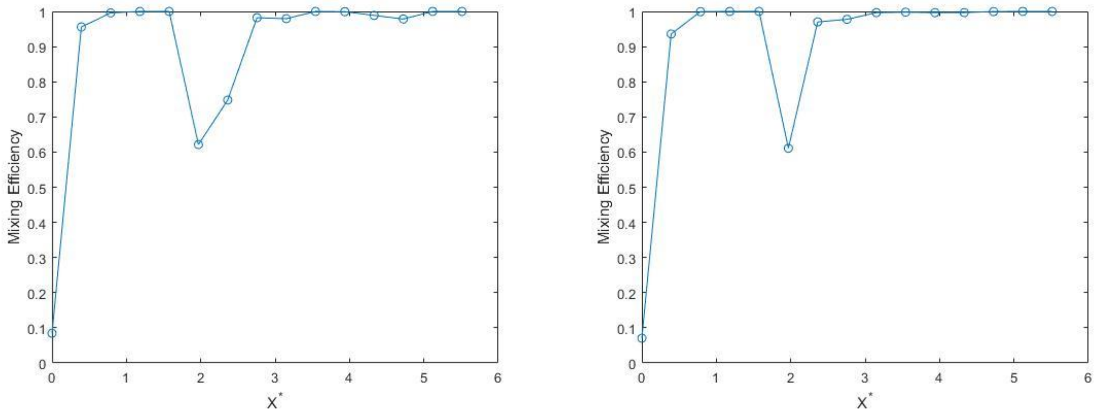

(b) 15 by 15

(c) 15 by 20

Figure 38 15 mm Strut-Cavity Mixing Efficiencies

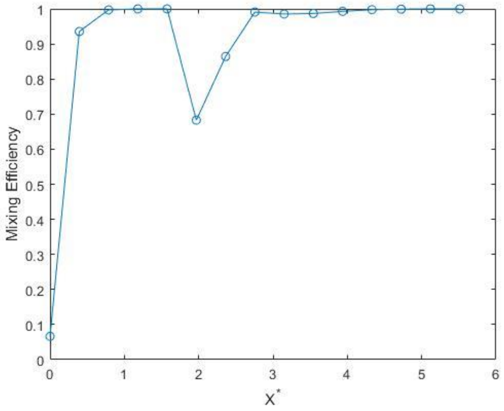

(a) 7.17 by 10

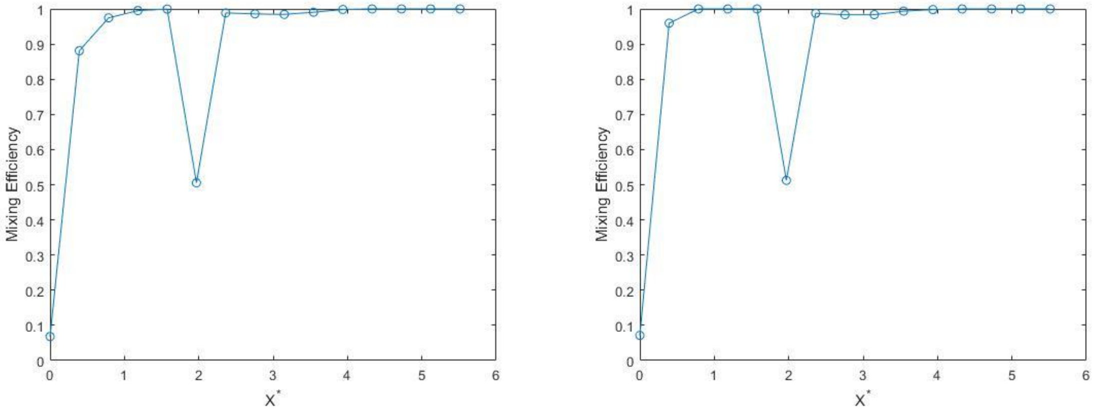

(b) 7.17 by 15

(c) 7.17 by 20

Figure 39 7.17 mm Strut-Cavity Mixing Efficiencies

From Figs. 33-39, it is apparent that mixing efficiency tends to increase as the non-dimensionalized distance x^* increases, with a significant decrease occurring at the location of the cavity inlet due to a large influx of unmixed fuel.

Comparing the mixing efficiencies, there is a clear difference between the flameholder designs in terms of the rate of change of efficiency through the combustor. For example, the two square cavity plots seen in Fig. 33 show a sharp increase in efficiency immediately downstream of the main fuel inlet, followed by a slow rise to becoming fully mixed at a non-dimensionalized distance of approximately three. The slanted cavity designs with and without the top injector behave similarly, becoming fully mixed at around the same non-dimensionalized distance. The double cavity designs, although initially similar in behavior to the square and slanted cavity geometries, do not reach an efficiency of one at any point in the combustor. In the reacting case, this can result in fuel being ejected without reacting, leading to poor performance of the engine. Comparatively, the strut-cavity designs demonstrate a near immediate rise of efficiency to unity, only dropping slightly due to the previously mentioned cavity fuel injector before returning to a value of one through the remainder of the combustor. This is somewhat expected due to the behavior of the strut as a bluff body; as a result of the vortices generated from flow separation (see Fig. 31), fuel is dispersed along the height of the isolator and combustor. This contributes to even and complete combustion of the fuel before it enters the nozzle, introducing more energy to the flow, and therefore allowing for a higher possible thrust output of the engine.

While high quality mixing is vital to proper performance of the scramjet, a reacting analysis will provide more insight into how the effects of the flameholder translate to flame stability and overall behavior of the combustor. As a scramjet can operate upwards of Mach 10, varying the inlet velocity will also be necessary to fully understand the viability of each design.

4.2 Reacting Simulations at M = 2.2

By applying the previously discussed eddy dissipation model to the non-reacting simulations, the effects of the flameholders on a reacting flow field can be analyzed. The selected combustion model often overpredicts temperatures, therefore an H_2O mass fraction contour should be used to observe the flame location. Studies by Kedia and Ghoniem in [18] and Wan et al in [19] use a similar technique to demonstrate flame anchoring by observing the distribution of combustion products, namely radicals, to determine recirculation regions. A similar concept was used here, although with the primary combustion product (water), as only a single step reaction was considered. The H_2O mass fraction contours for all geometries at an inlet Mach number of 2.2 are shown in Figs. 40-46.

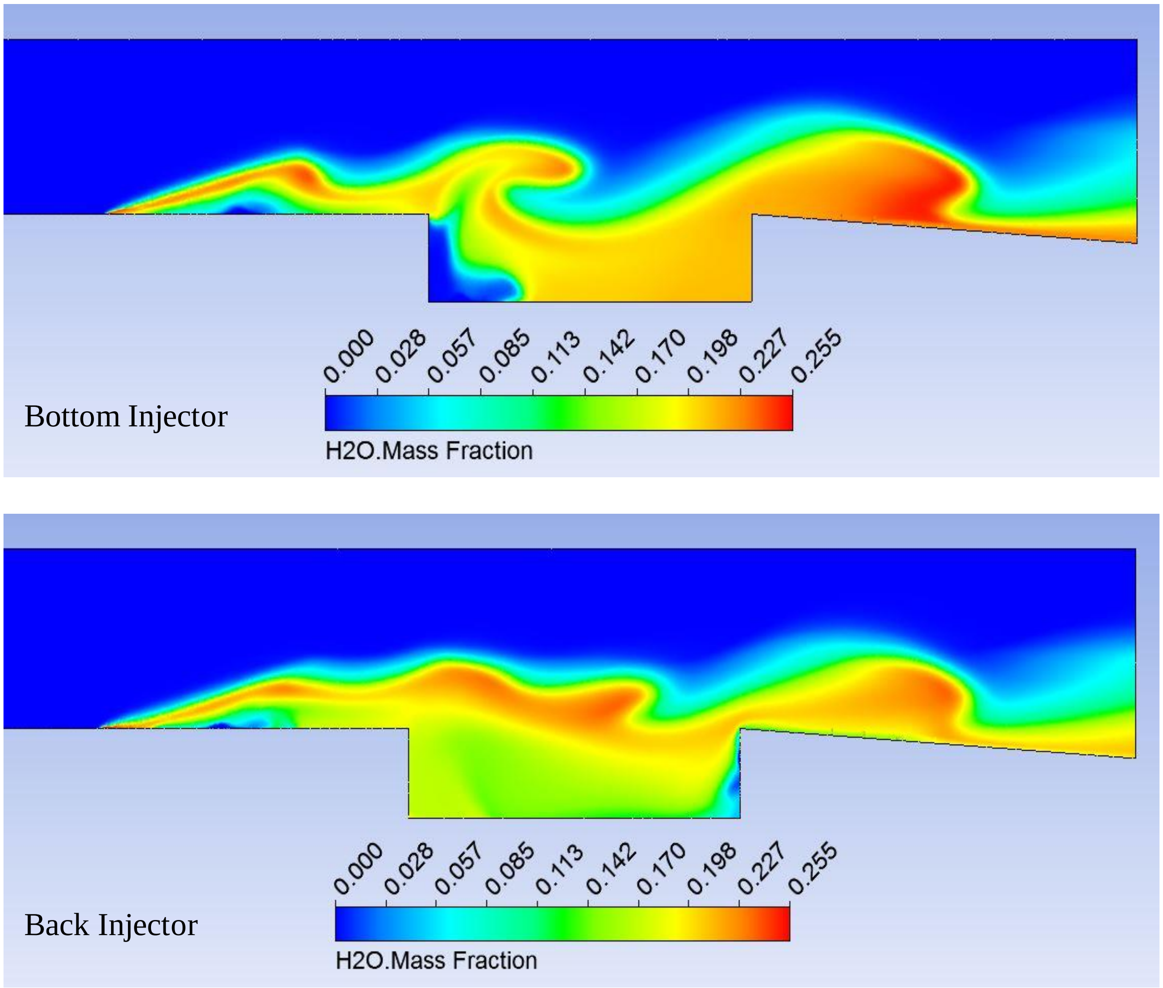

Figure 40 Flame Position, Square Cavity M = 2.2

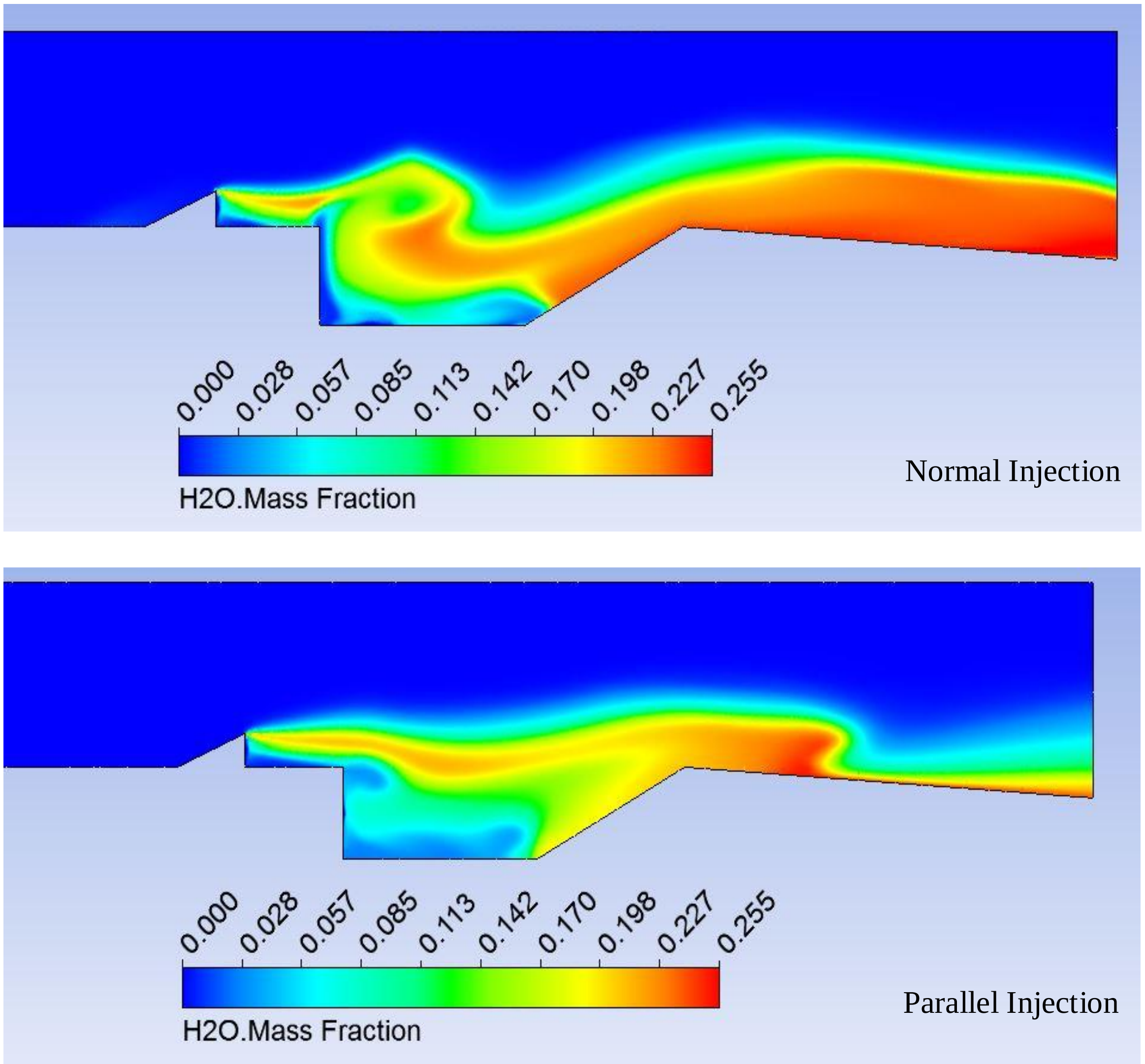

Figure 41 Flame Position, Slanted Cavity M = 2.2

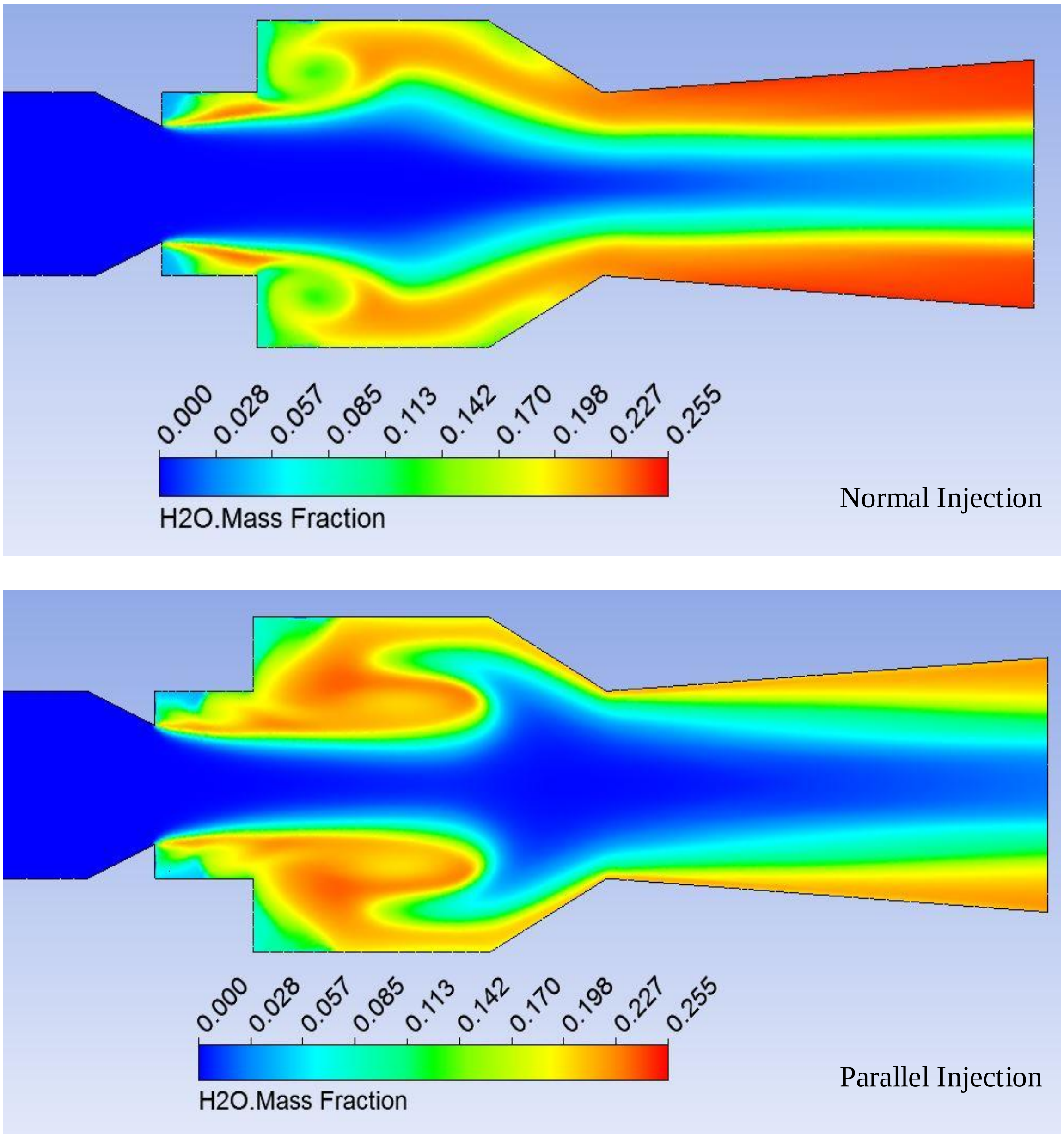

Figure 42 Flame Position, Double Cavity M = 2.2

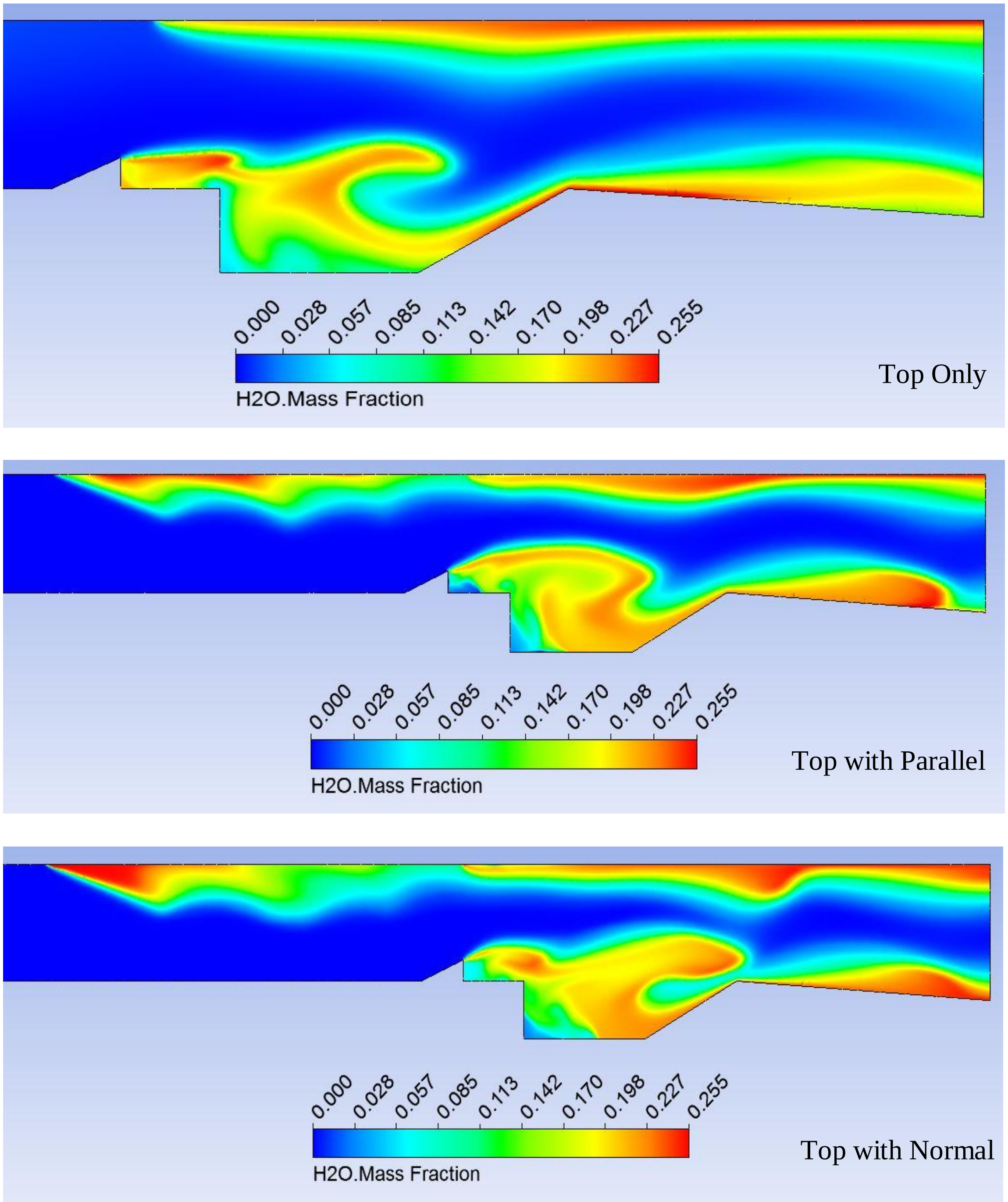

Figure 43 Flame Position, Slanted Cavity with Top Injector M = 2.2

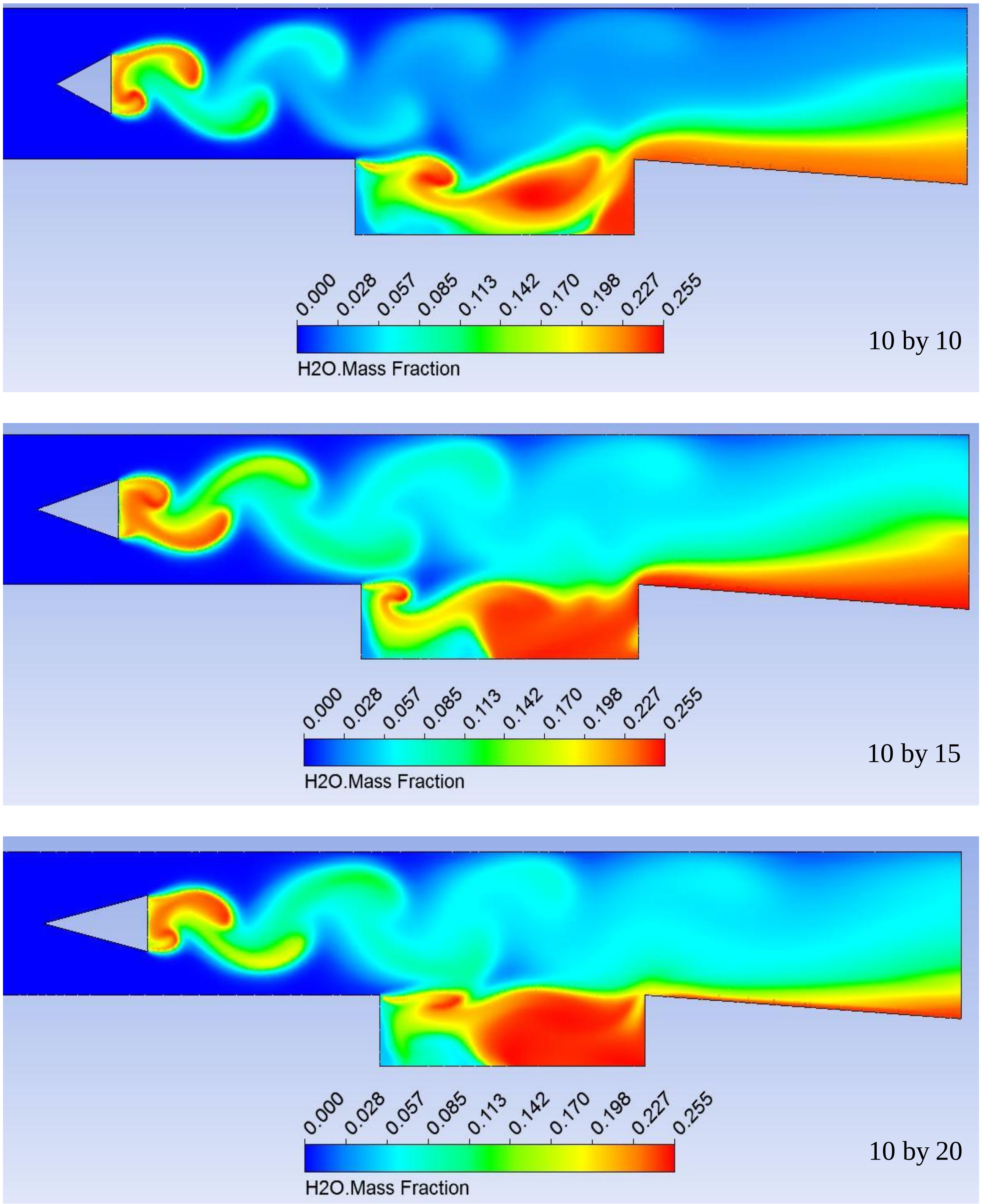

Figure 44 Flame Position, 10 mm Strut-Cavity M = 2.2

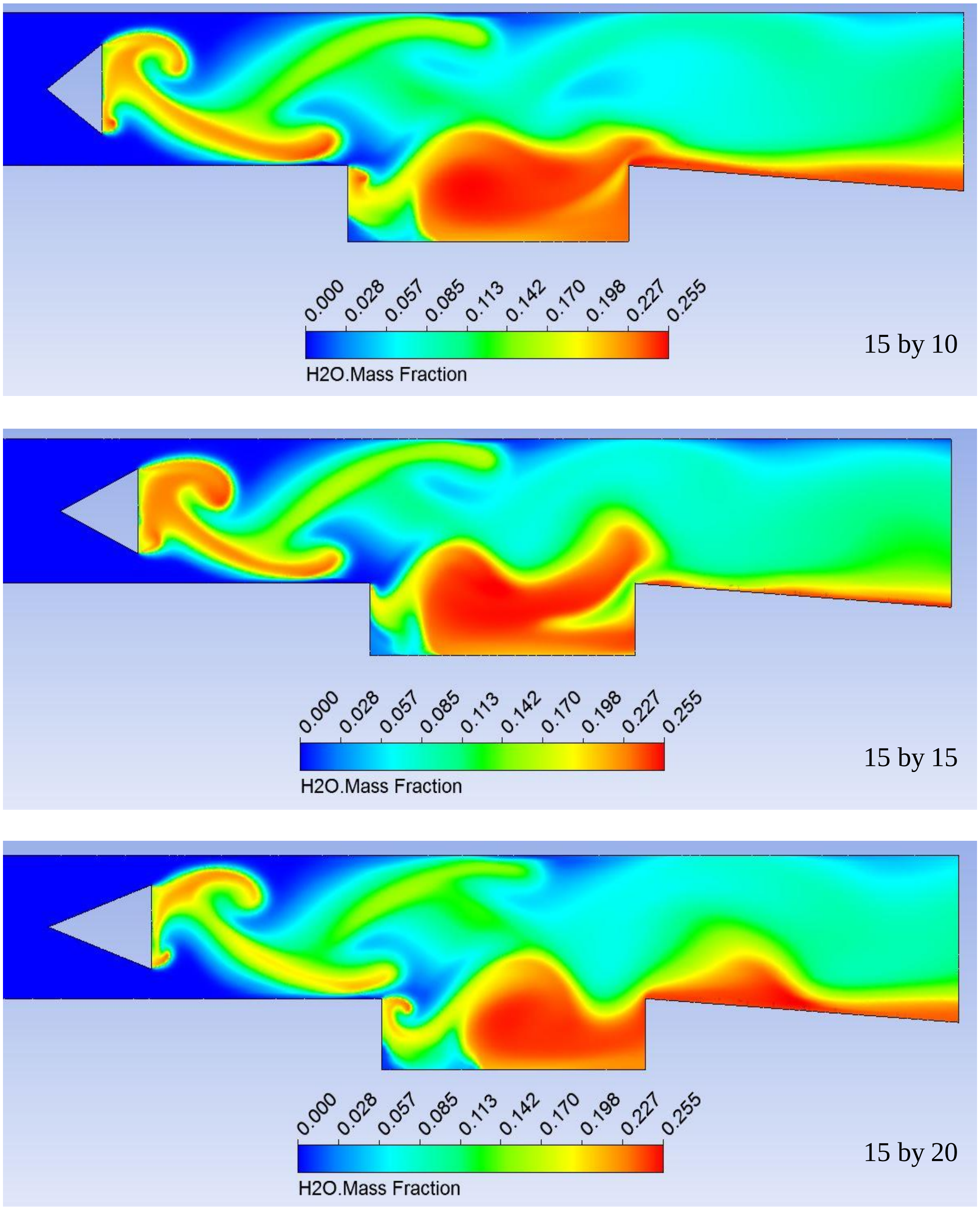

Figure 45 Flame Position, 15 mm Strut-Cavity M = 2.2

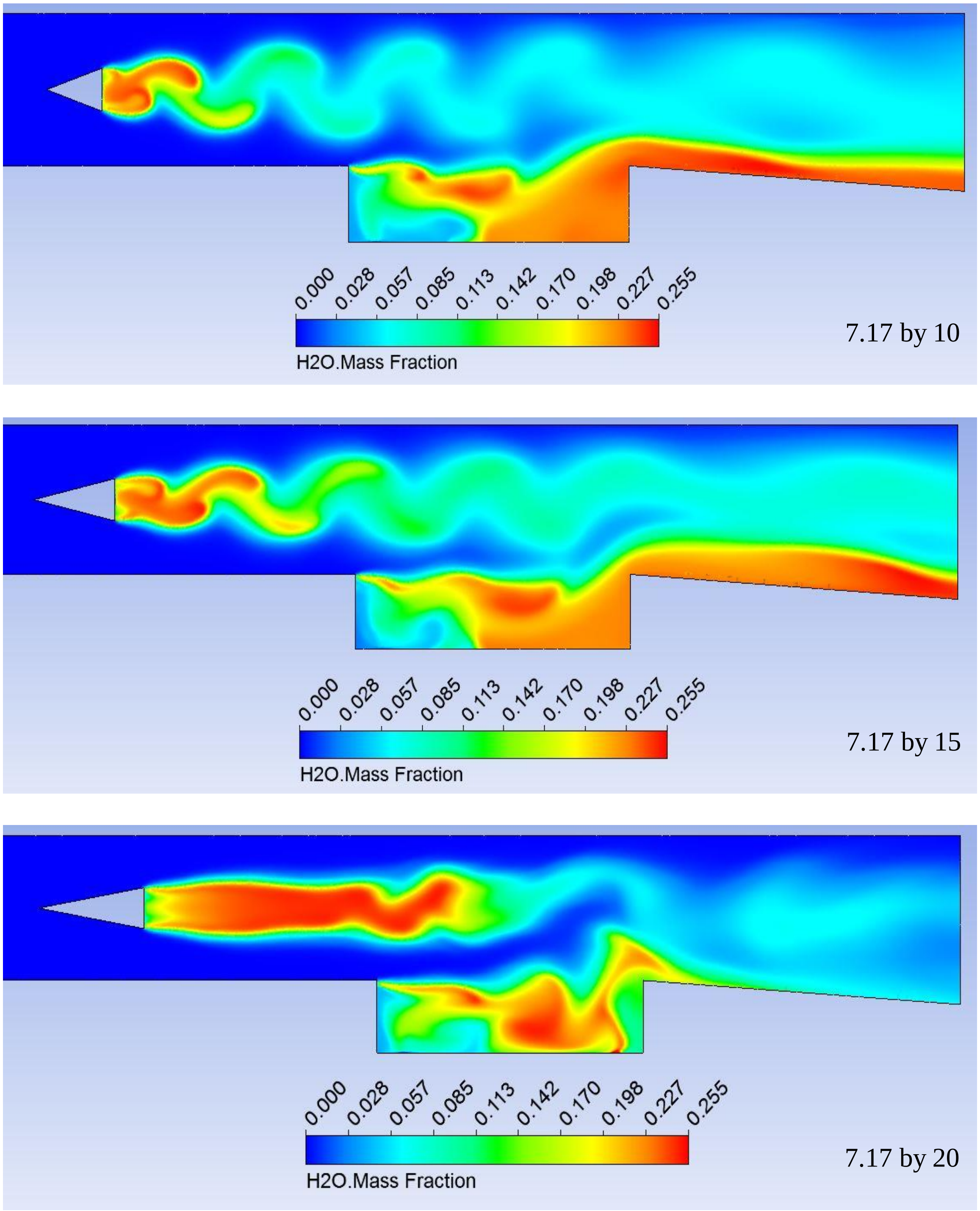

Figure 46 Flame Position, 7.17 mm Strut-Cavity M = 2.2

Much like in the mixing analyses, several patterns are observed across all combustor geometries. The most apparent is the effect of the cavity on the flame; in the majority of the contours, there is a visible flame contained within the cavity that is anchored to the top of its front face or just upstream of its front face, in the case of the slanted cavity. The square cavity cases in Fig. 40 do not directly demonstrate this anchoring effect as a result of the upstream fuel inlet, which generates combustion ahead of the cavity; however, it is evident that the flame is partially contained within the cavity prior to exiting the combustor. Also apparent are large vortices generated by the cavities and ramp (in the case of the slanted cavity designs). These appear as bulges or “waves” in the flames.

Flame anchoring is also observed on the trailing edge of the strut in Figs. 44, 45, and 46. This flame is seen “waving” due to vortex shedding on the strut, but is nevertheless attached to the back of the strut, providing for sustained combustion in the freestream. These vortices are consistent with the observations made in the non-reacting field seen in Fig. 31, and assist in spreading fuel and the flame through the combustor. The size of these vortices is directly affected by the size of the strut, with the 15 mm struts (Fig. 45) producing vortices that span almost the entire height of the engine, while the 7.17 mm by 20 mm strut (Fig. 46) generates very small downstream perturbations at the center of the flow. Based on these results, however, it can be claimed that the size of the strut does not directly affect flameholding capabilities.

Although all of these geometries do exhibit flameholding in some form, there is a notable deficiency in the slanted cavity with the top injector. In the normal and parallel injecting cases, the use of the top injector leads to reaction occurring upstream of the combustor due to shock induced flow separation. While complete combustion is desired, the location of the combustion is also important for proper operation of the engine. By combusting inside of the isolator, the risk of engine unstart increases due to thermal choking of the flow, which can cause failure during operation if the flame approaches the inlet [20]. For this reason it is crucial to maintain a degree of separation between the air inlet and the combustion region; although this design did not develop such drastic flow separation, it would still be necessary to alter it to avoid the possibility of unstart in practical applications.

It must be recognized that the exact location of the flame anchoring is not completely correct in these simulations. The use of the EDM causes immediate combustion upon reaching a stoichiometric ratio of fuel to air for a single-step reaction. Due to this, the phenomenon of flame liftoff is not observed. In a multi-step reaction, a small gap is often seen between the flameholder/fuel inlet and the generation of the final reaction product due to intermediate reactions involving radicals. In these results, no such gap is observed due to the lack of radical production, which does not fully represent the reaction mechanism of hydrogen and oxygen. In a CFD analysis of a scramjet by Hyslop, increasing the amount of reaction steps decreased the wall pressure over the length of the engine and increased the delay time between injection and combustion as compared to a single-step reaction [21]. However, the overall profile of the reacting zone did not vary between multi-step and single-step reactions. From this, as well as the previously discussed importance of turbulent mixing as compared to chemical kinetics due to short residence times, these combustion results can be considered a good approximation of the flame position.

4.3 Reacting Simulations at M = 4

As discussed in Section 4.2, using a combustion product mass fraction contour allows for visualization of the flame inside of the combustor. Shown in Figs. 47-53 are the H_2O mass fraction contours for the reacting case at an inlet Mach number of 4 (1700.9 m/s).

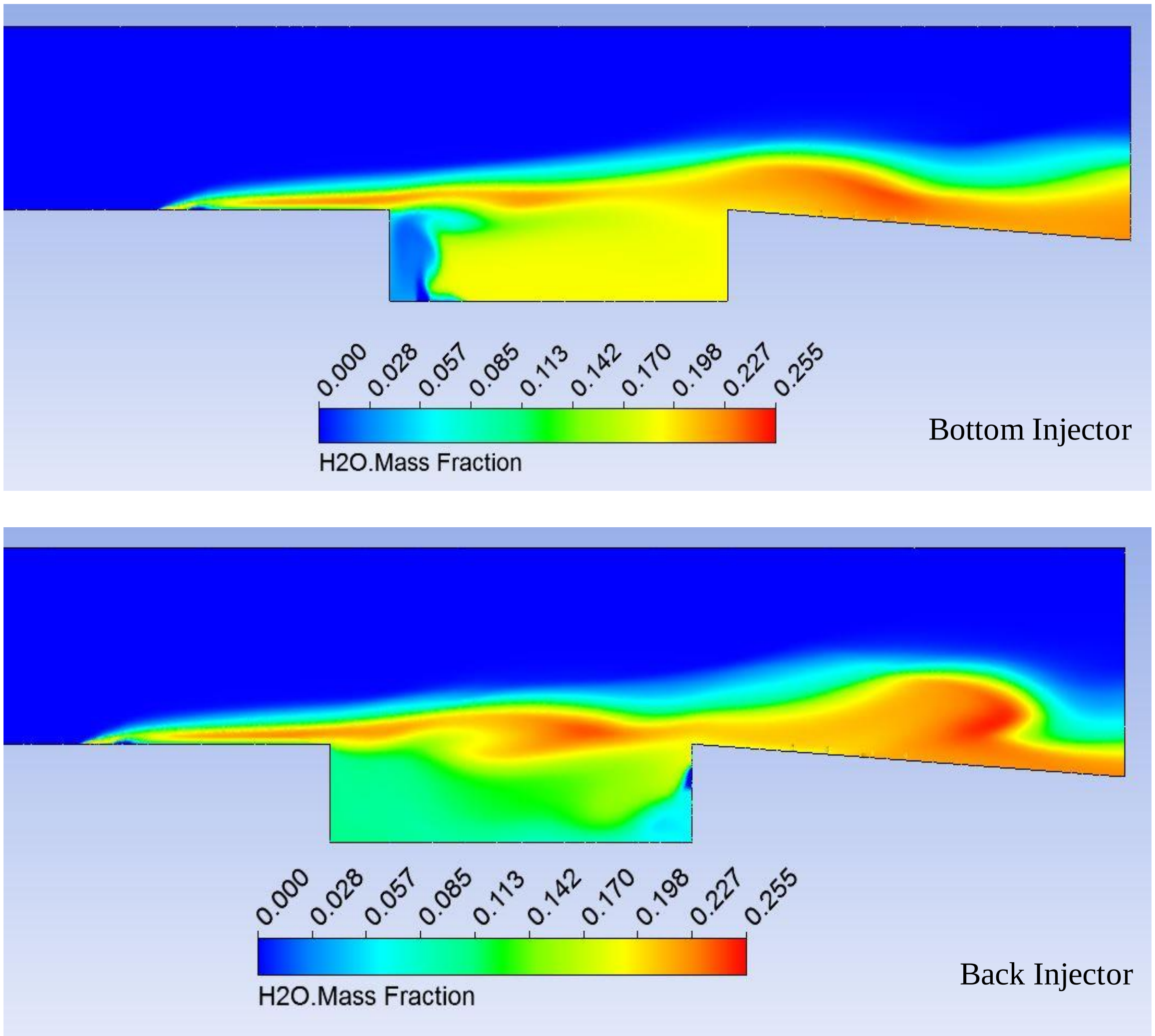

Figure 47 Flame Position, Square Cavity M = 4

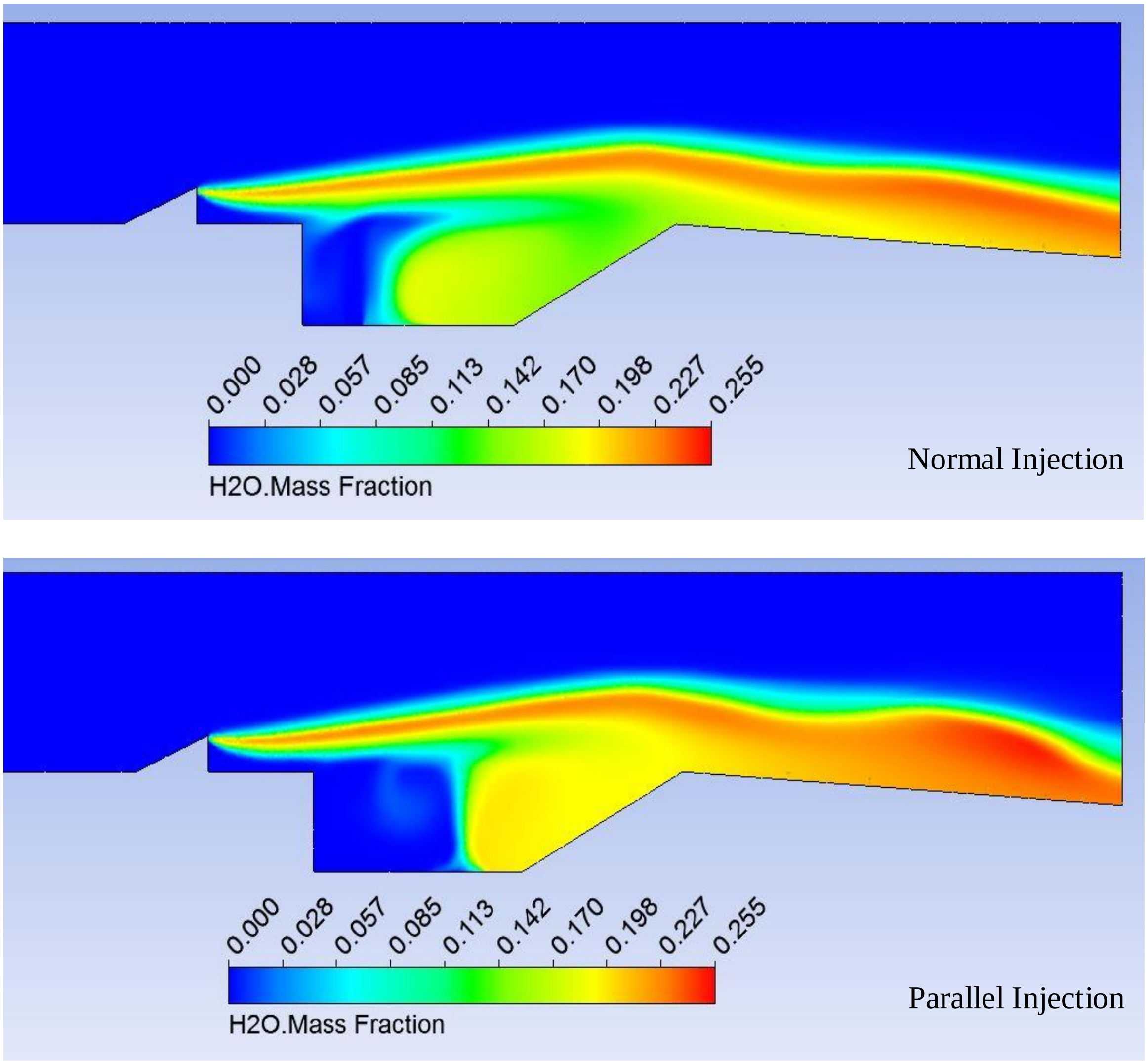

Figure 48 Flame Position, Slanted Cavity M = 4

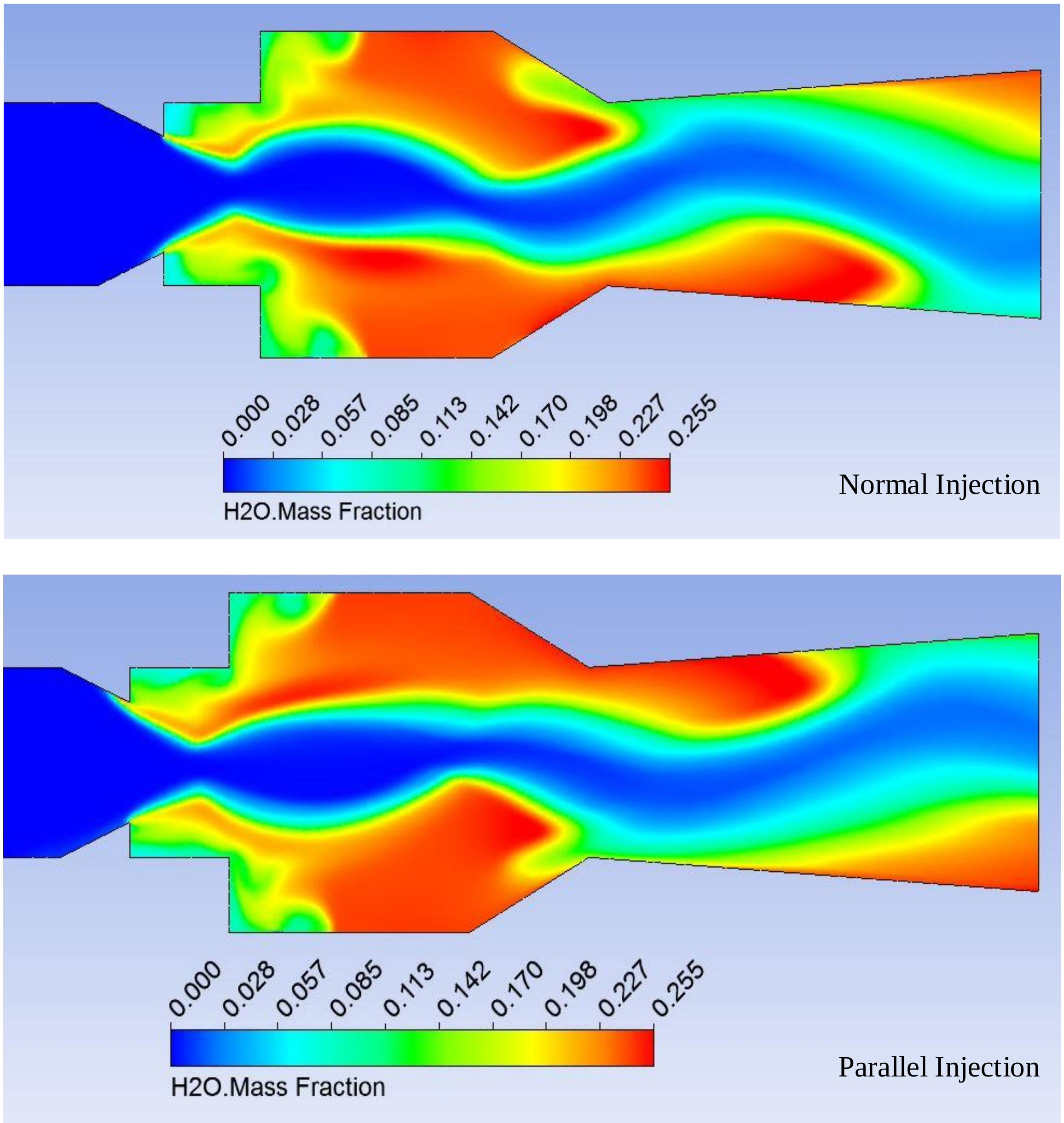

Figure 49 Flame Position, Double Cavity M = 4

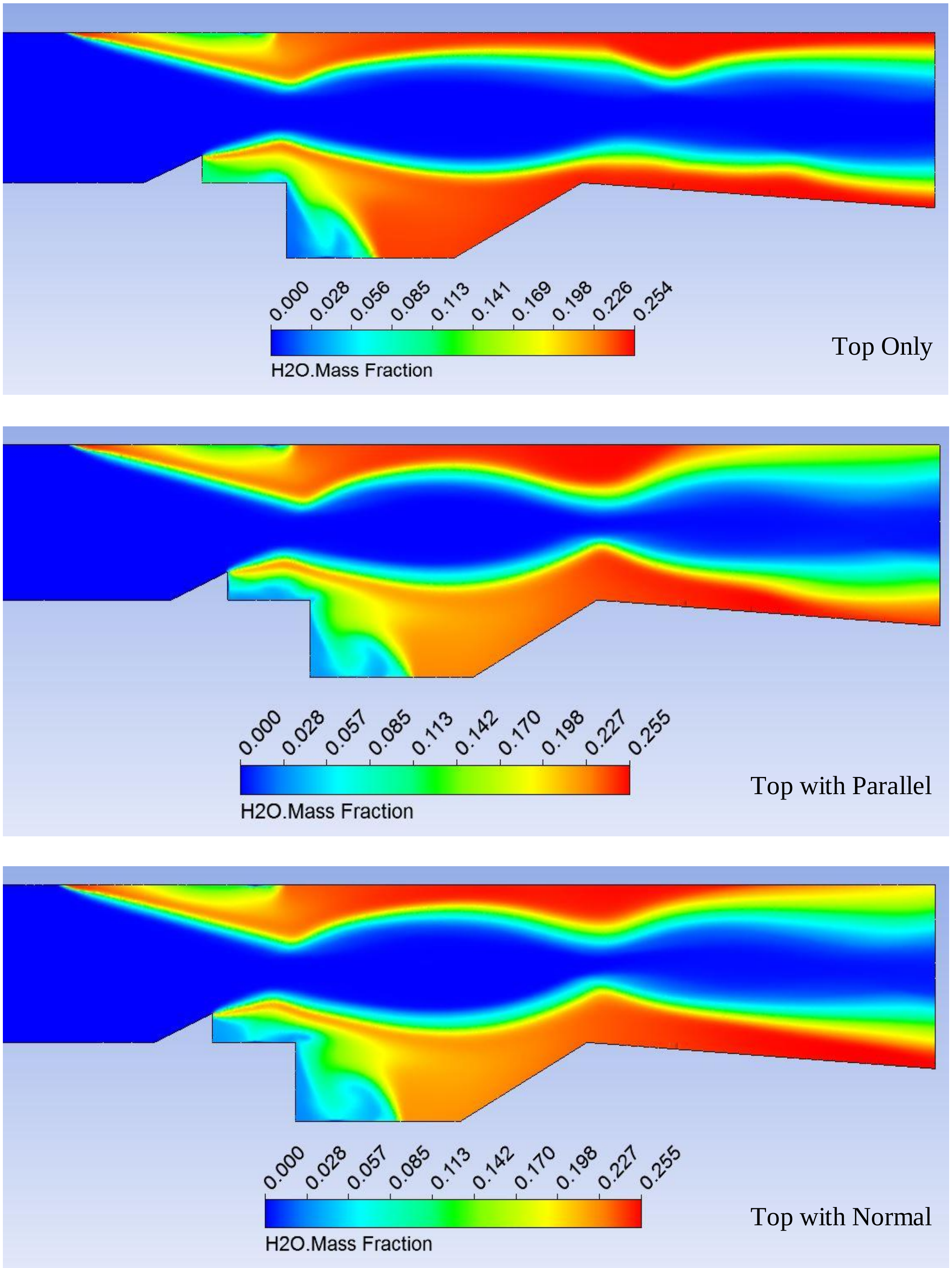

Figure 50 Flame Position, Slanted Cavity with Top Injector M = 4

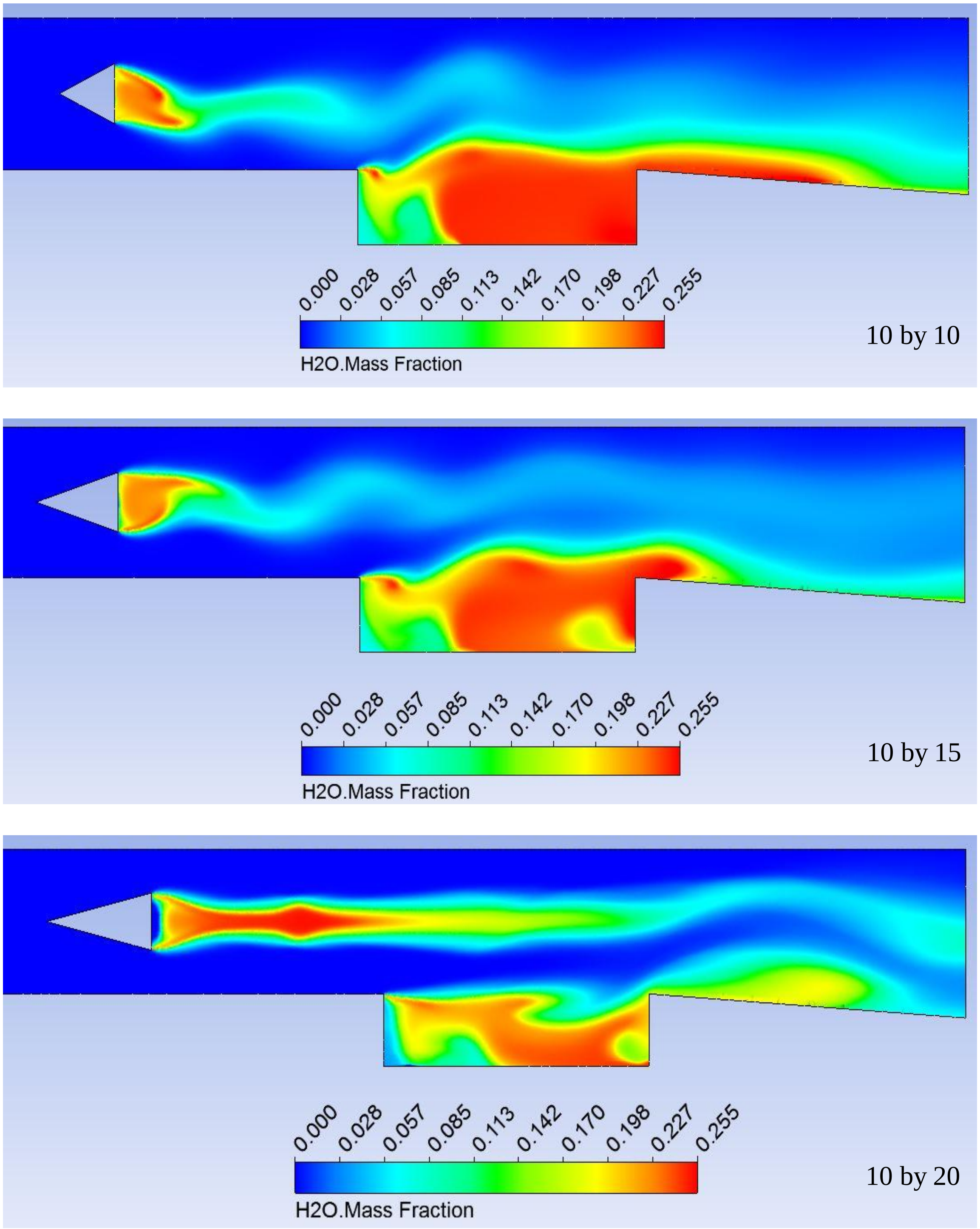

Figure 51 Flame Position, 10 mm Strut-Cavity M = 4

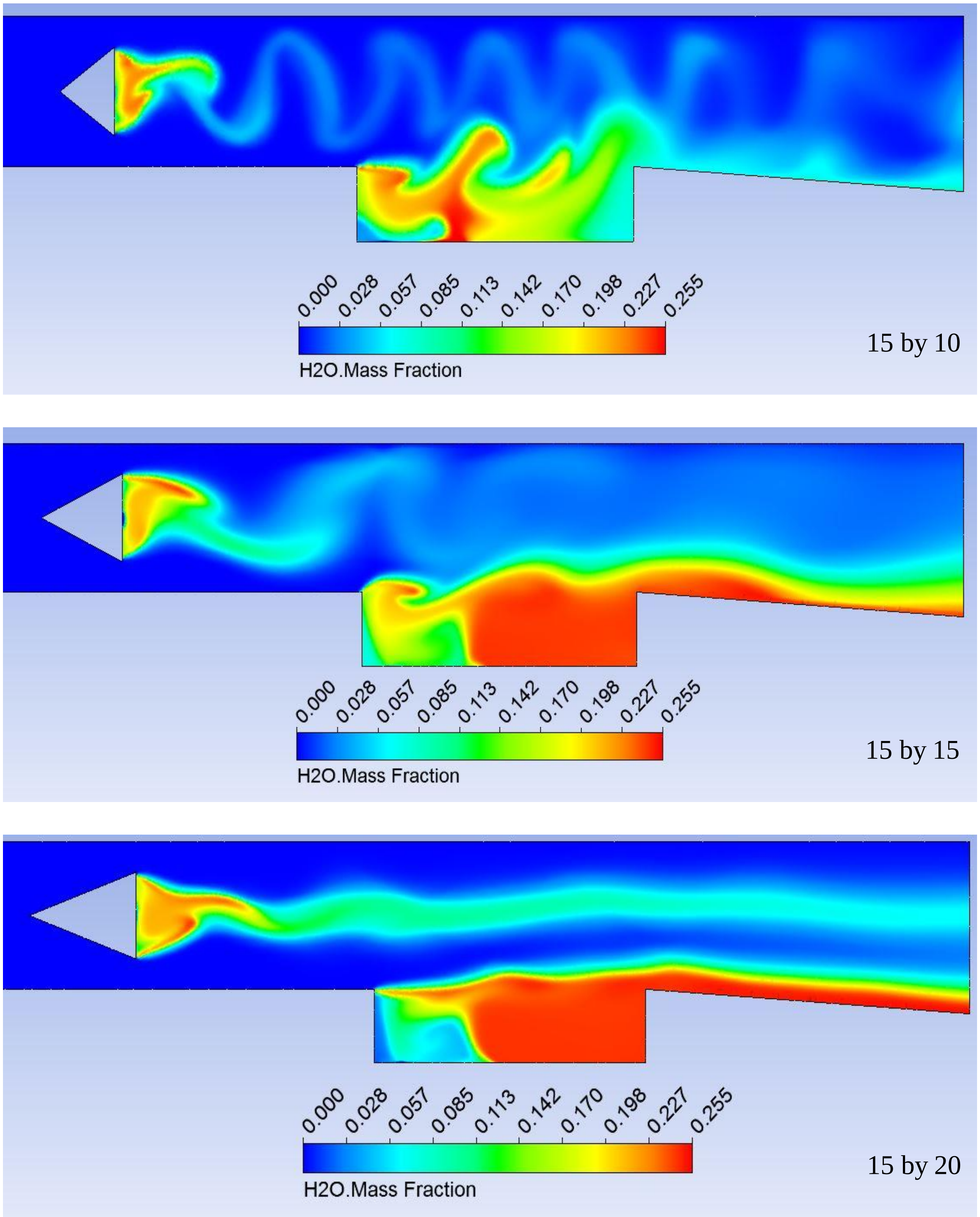

Figure 52 Flame Position, 15 mm Strut-Cavity M = 4

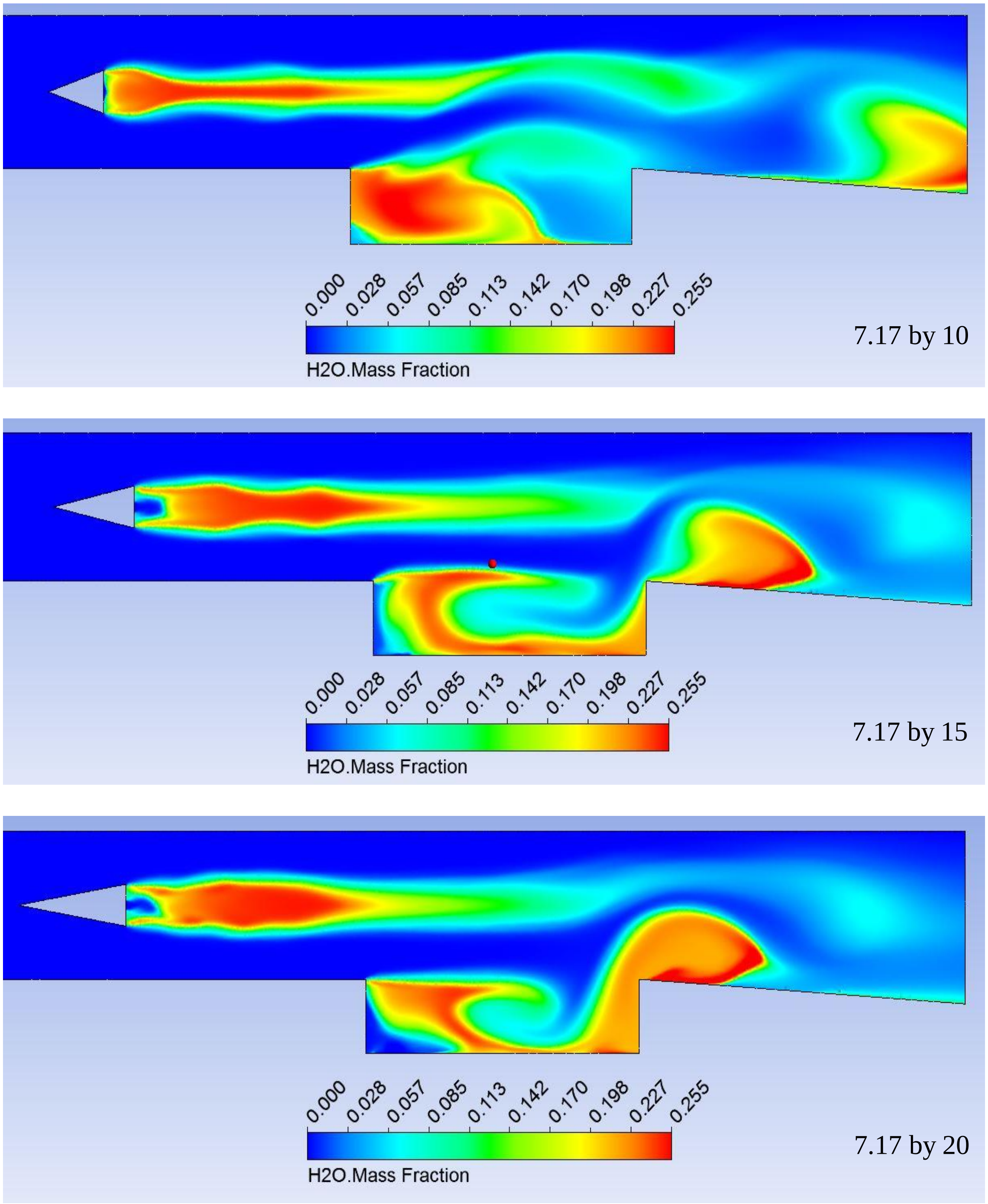

Figure 53 Flame Position, 7.17 mm Strut-Cavity, M = 4

The behavior of the flame at an inlet Mach number of 4 is comparable to its behavior at M = 2.2; flame anchoring is evident at the leading edge of most cavities, at the top of the ramp in the slanted cavity cases, as well as on the downstream faces of the struts. Again, in the square cavity cases, the flame is not necessarily anchored at the edge of the cavity, but is captured in the cavity due to the recirculation region shown in Fig. 28. There are several differences in the flame shape as a result of the increased flow velocity. The most notable difference is the lack of large eddies formed due to vortex separation on the 10 mm by 20 mm strut in Fig. 51 and the 7.17 mm struts in Fig. 53. As a result of an increase in flow velocity, the vortex street transitions into a turbulent wake and no longer forms the large swirls that were shown in Figs. 44, 45, and 46. The lack of a vortex street does not affect the ability for the strut to hold a flame, as each design has an attached region of high H_2O concentration, indicating high temperature reaction.

At this inlet velocity, there is evidence to suggest that the orientation or placement of fuel inlets for a design does not have an impact on the flameholding characteristics of the design. In the slanted cavity with and without the top inlet designs in Figs. 48 and 50, as well as in the double cavity design in Fig. 49, different fuel injection schemes do not change the position or shape of the flame. While there may appear to be differences, such as the distribution of the flame in the double cavity (which is simply mirrored over a central axis), or the location of the flame front inside the slanted cavity without a top injector, they are not appreciable in terms of overall flame stability.

4.4 Reacting Simulations at M = 6

As it was observed that placement of the fuel injectors for a given combustor design did not generate a significant difference in flame position at higher velocities, it is necessary to only look at one injector layout per design. This group of H_2O contours is shown Figs. 54-60 for an inlet Mach number of 6 (2551.3 m/s).

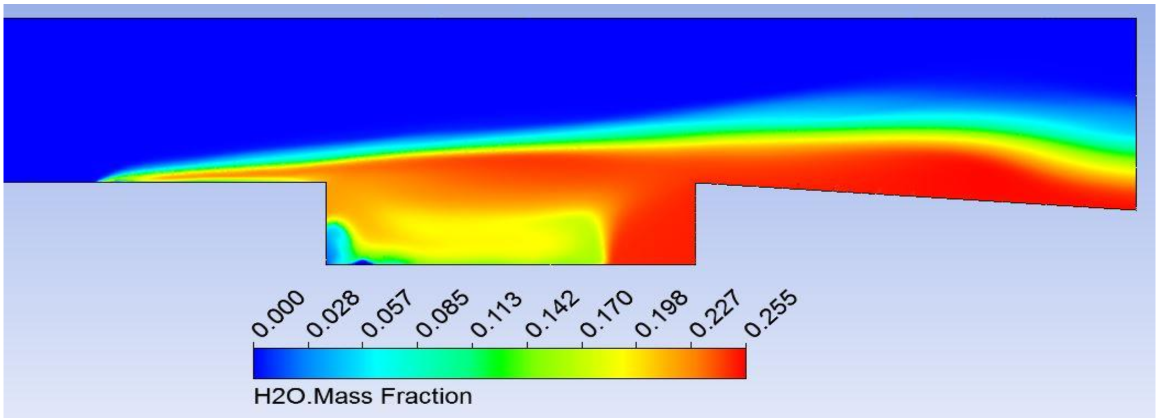

Figure 54 Flame Position, Square Cavity M = 6

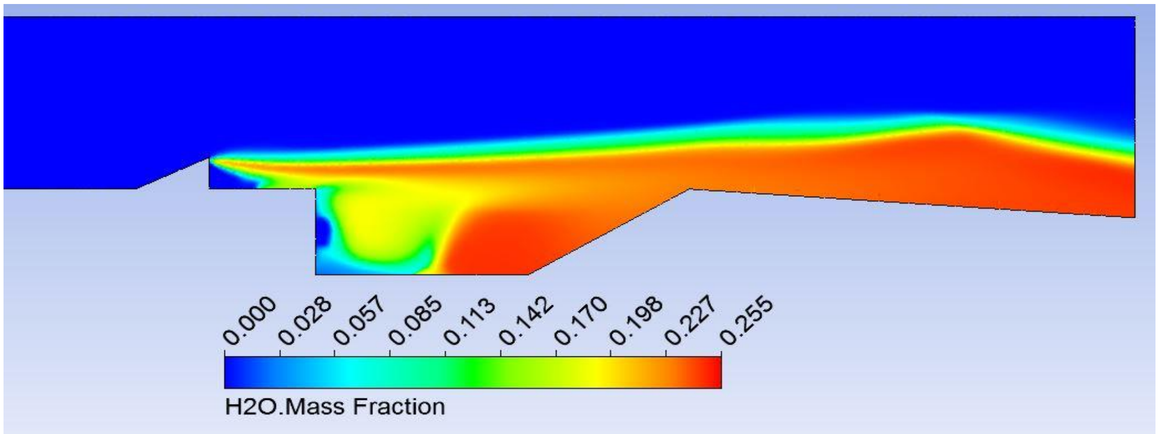

Figure 55 Flame Position, Slanted Cavity M = 6

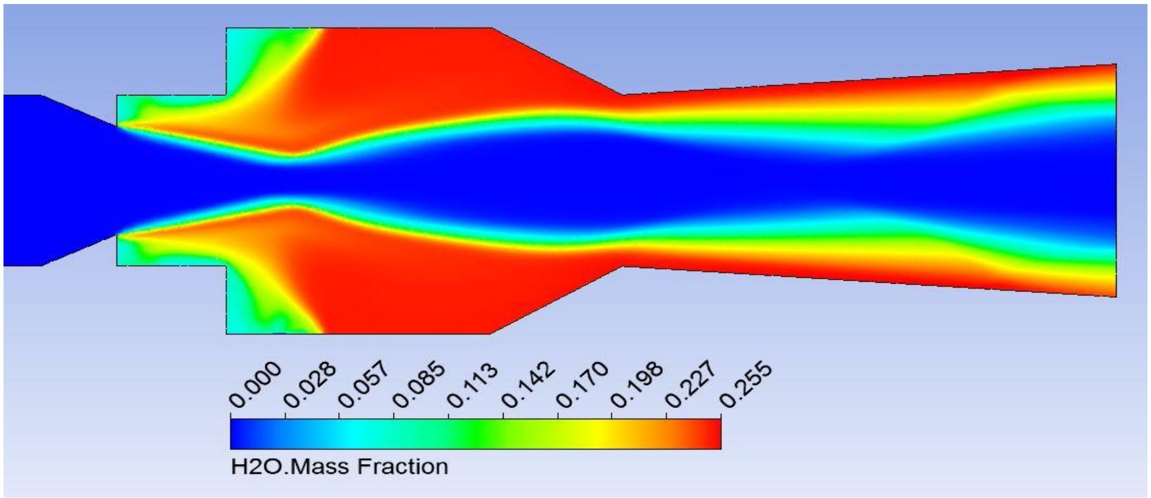

Figure 56 Flame Position, Double Cavity M = 6

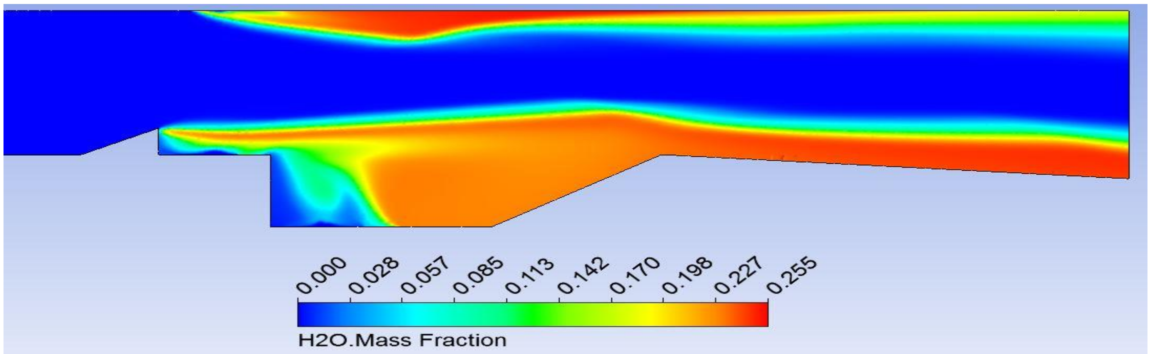

Figure 57 Flame Position, Slanted Cavity with Top Injector M = 6

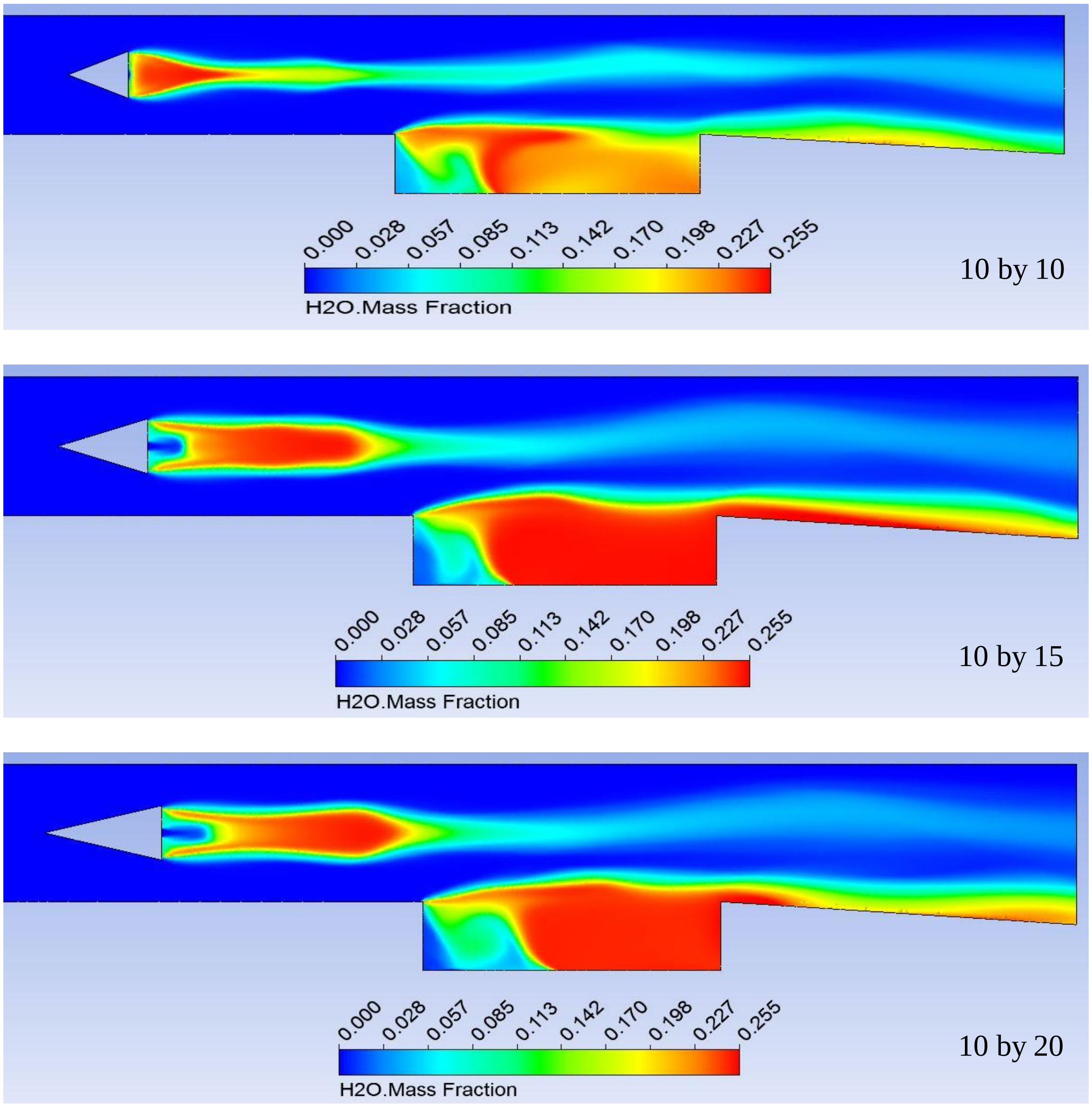

Figure 58 Flame Distribution, 10 mm Strut-Cavity M = 6

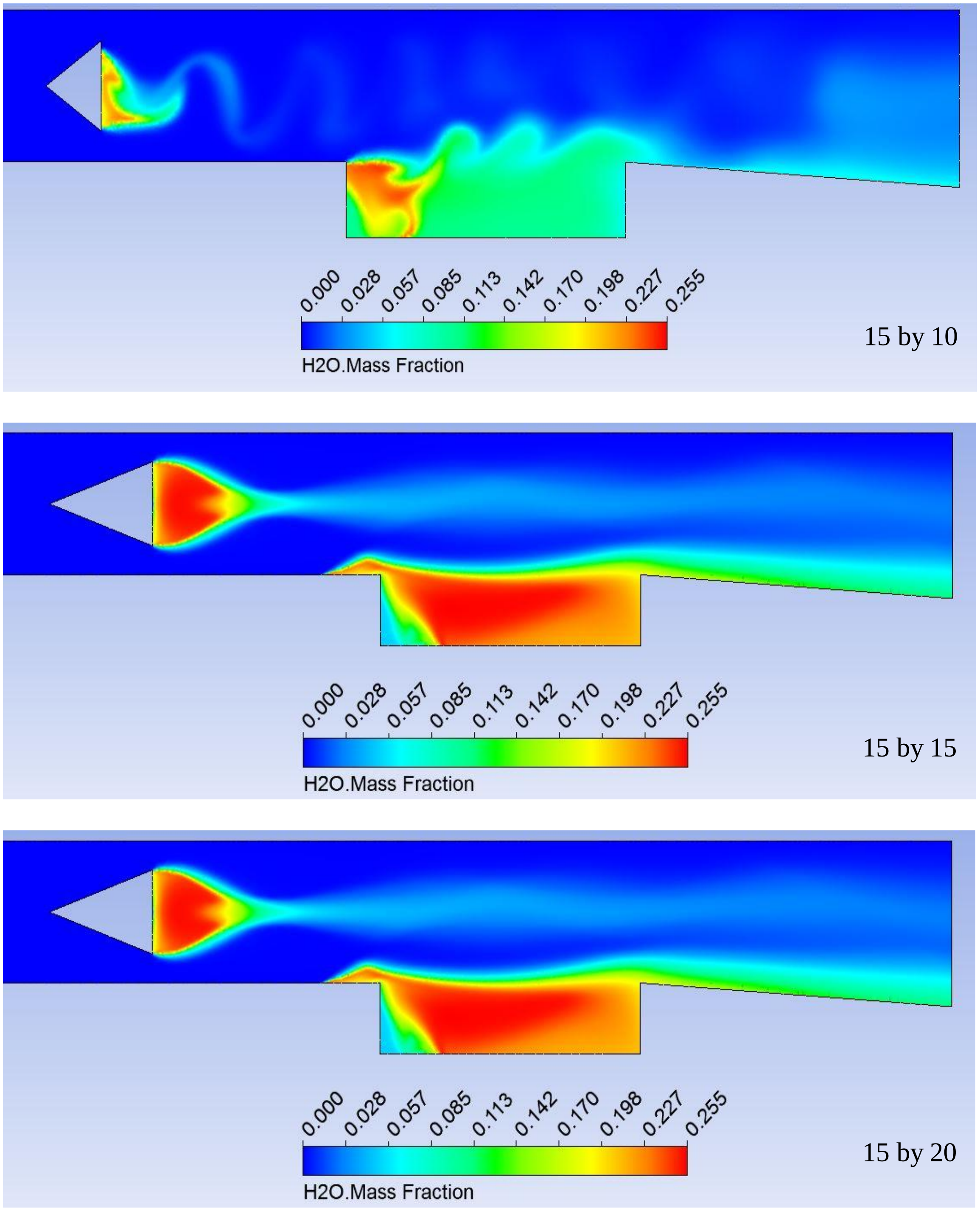

Figure 59 Flame Position, 15 mm Strut-Cavity M = 6

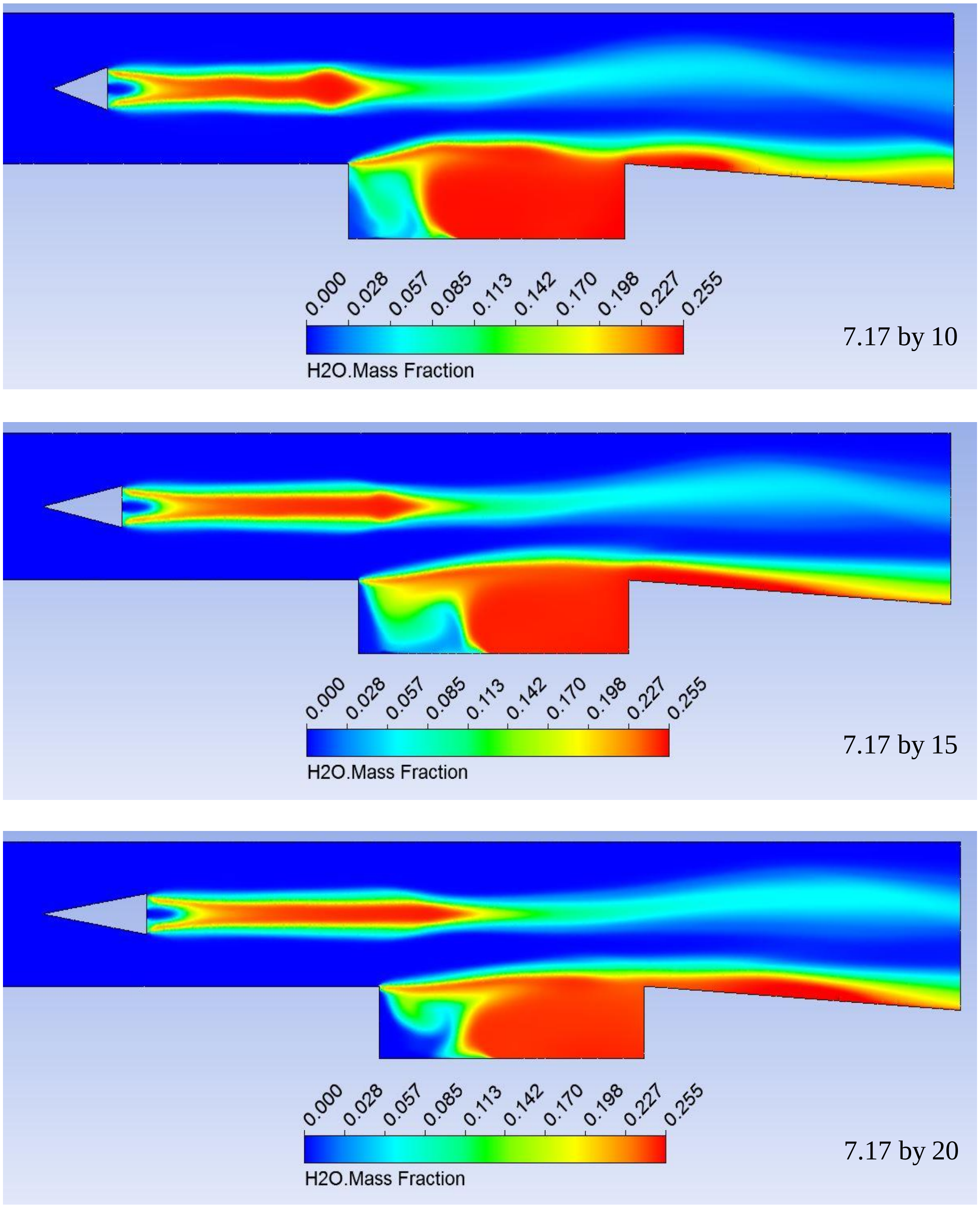

Figure 60 Flame Position, 7.17 mm Strut-Cavity M = 6

Flame stabilization on the strut and on the front face of the cavity/ramp is observed for all flameholders at an inlet Mach number of 6. Figure 59 shows a flame that is held very close to the downstream edge of the strut in the 15 mm by 10 mm design, as well as a “rippled” flame in the cavity. This strut has a large deflection angle, leading to a lack of a turbulent wake downstream. Instead, a vortex street is formed, which quickly dissipates reaction products immediately downstream of the strut. These vortices interact with the flame in the cavity, causing the visible rippling effect. The effect of the shape of this strut will be discussed further when performing an overall analysis of the flameholder designs in combustion.

Similarity between the different struts is also observed in Figs. 58, 59, and 60, which all (except for the aforementioned 15 mm by 10 mm case) demonstrate the transition to a turbulent wake rather than a vortex street as a result of an increased inlet Mach number. There does not appear to be a significant variation in the flame position when the length of the strut is changed for a given width, although the flame does tend to extend further into the combustor for longer struts. Also, the length of the strut does not seem to have as much of an effect on the cavity flame for a given base width as it did at lower inlet Mach numbers (see Figs. 51-53).

4.5 Reacting Simulations at M = 8

It was found from the previous section that increasing the inlet Mach number leads to similarity of the flame position for a given strut width, as well as the already discussed uniformity between different fuel inlet layouts. Knowing this, the H_2O contour data can be condensed further, and is shown in Figs. 61-67.

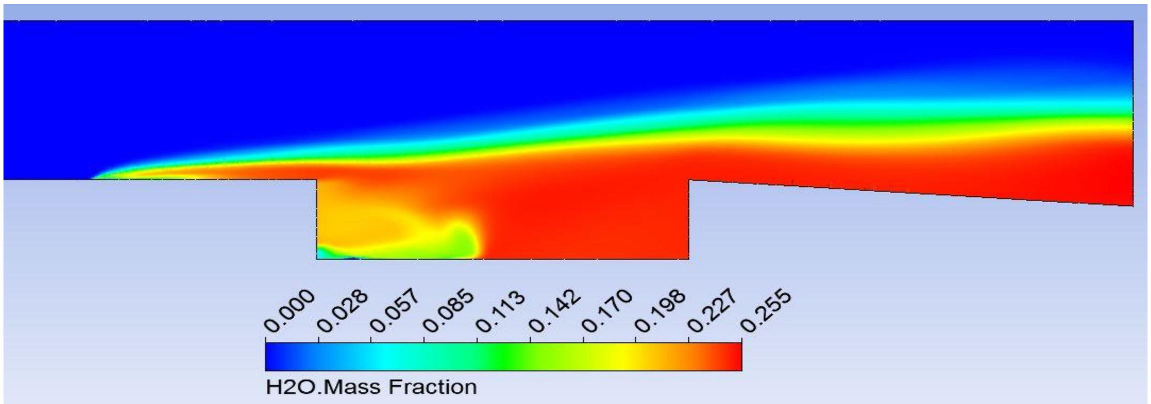

Figure 61 Flame Position, Square Cavity M = 8

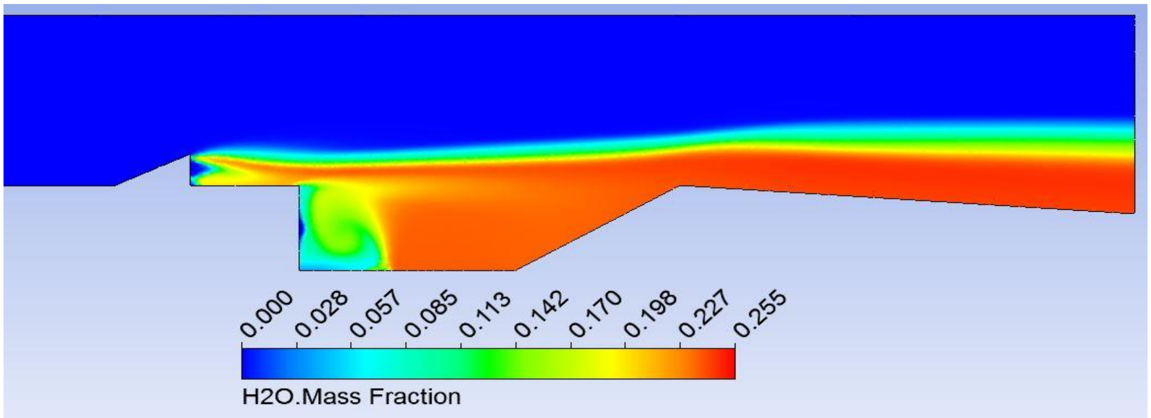

Figure 62 Flame Position, Slanted Cavity M = 8

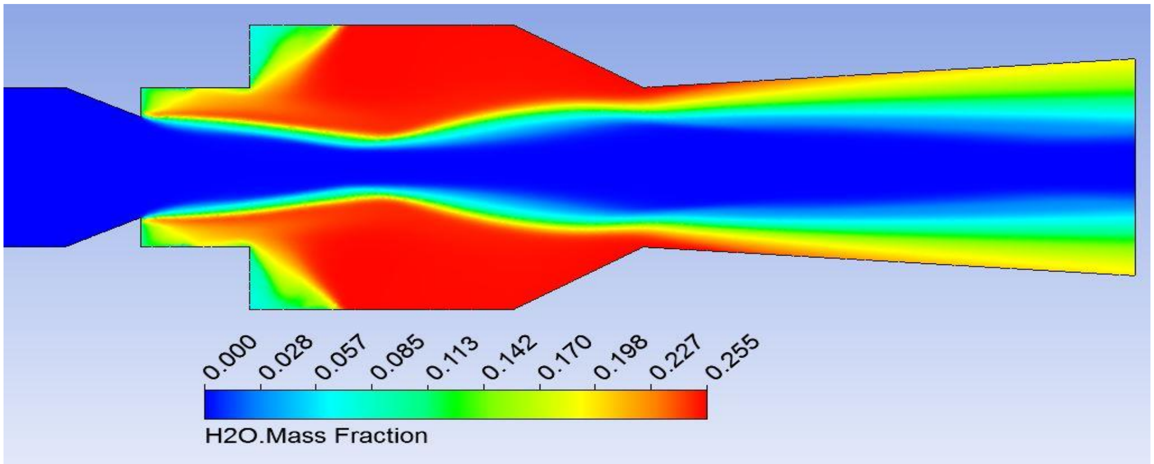

Figure 63 Flame Position, Double Cavity M = 8

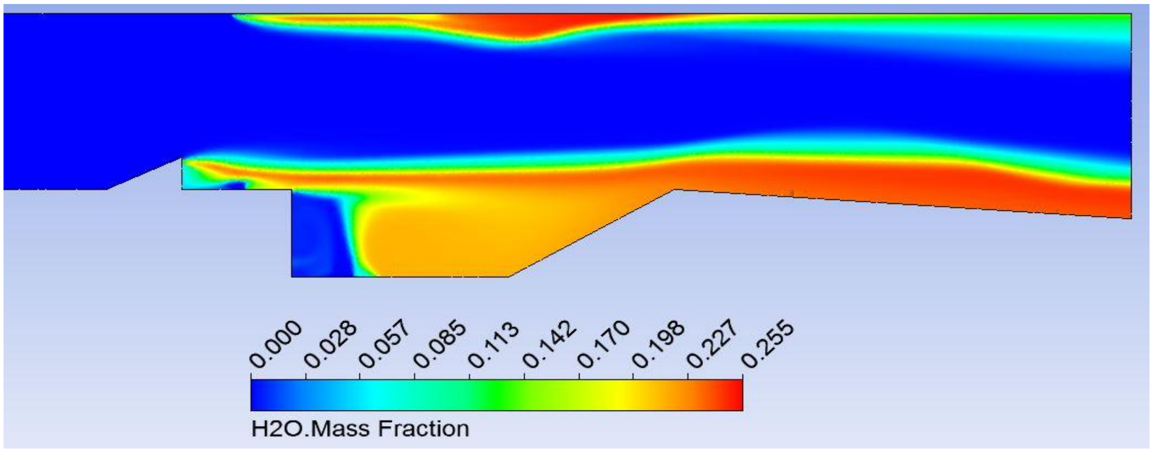

Figure 64 Flame Position, Slanted Cavity with Top Injector M = 8

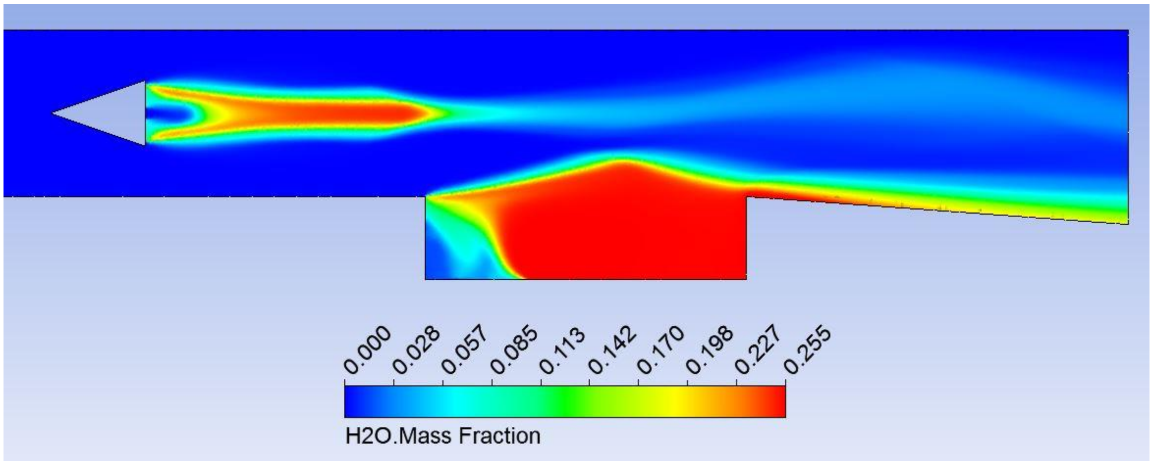

Figure 65 Flame Position, 10 mm Strut-Cavity M = 8

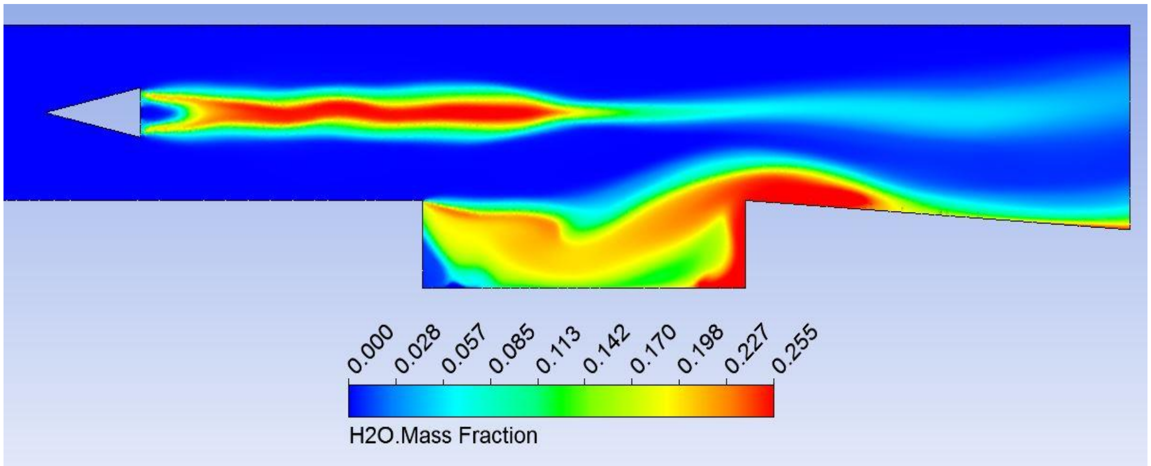

Figure 66 Flame Position, 7.17 mm Strut-Cavity M = 8

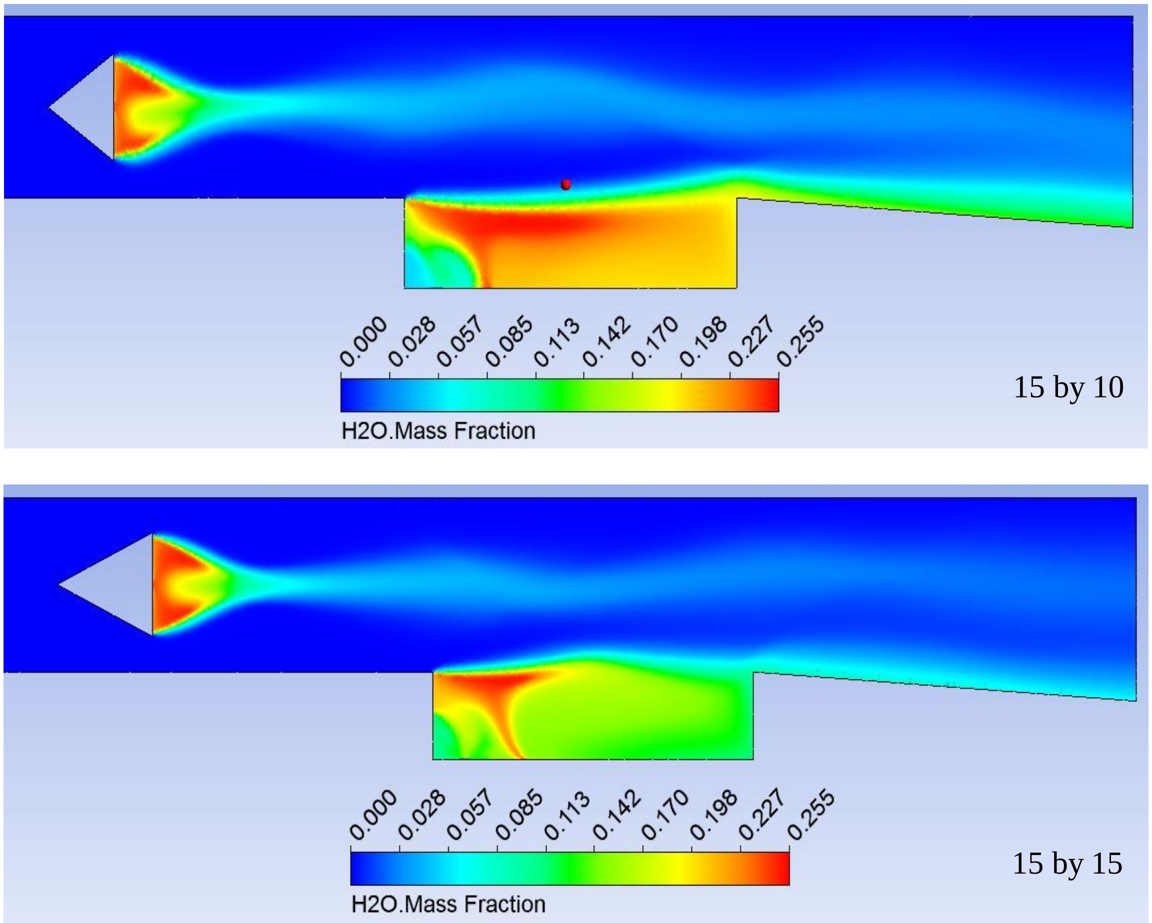

Figure 67 Flame Position, 15 mm Strut-Cavity M = 8

Apparently, the position of the flame in the combustor is now only a direct result of the flameholder being used at an inlet Mach number of 8. The 15 mm by 10 mm strut, which generated a vortex street at M = 6, has now transitioned to the turbulent wake with an attached flame, much like the other strut sizes. Flame positions in all other geometries are similar to those seen at M = 6.

4.6 Reacting Simulations at M = 10

Data from combustion analyses at an inlet Mach number of 10 (4252.2 m/s) are shown in Figs. 68-74, again only considering each geometry as opposed to fuel injector location, as this has been shown to not affect flame position or flameholding behavior at high Mach numbers.

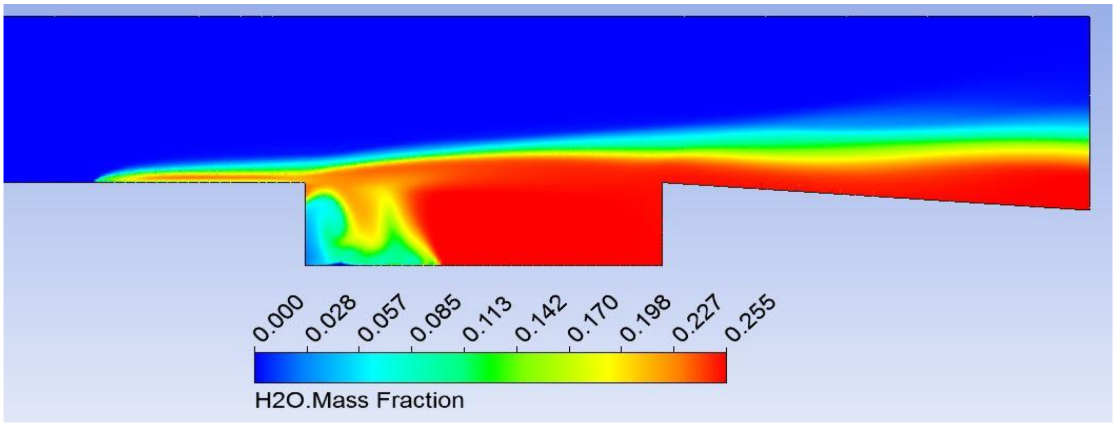

Figure 68 Flame Position, Square Cavity M = 10

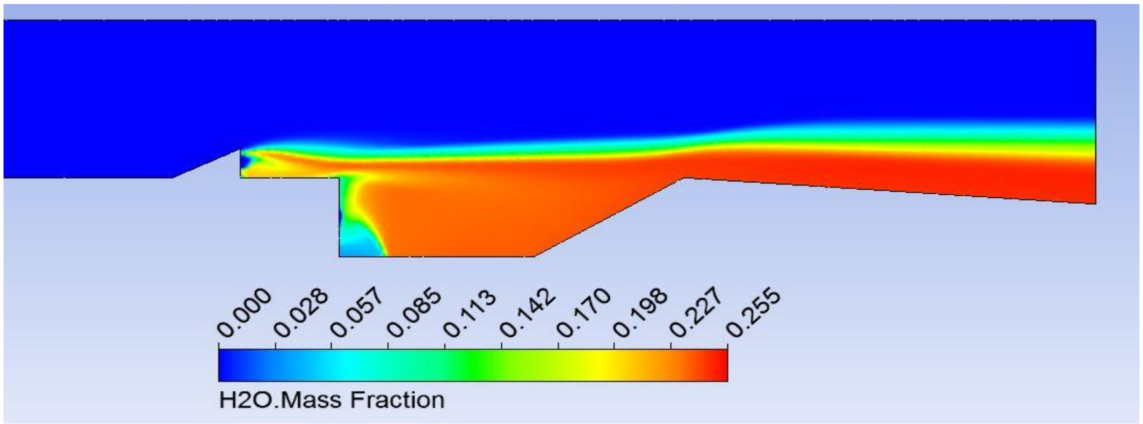

Figure 69 Flame Position, Slanted Cavity M = 10

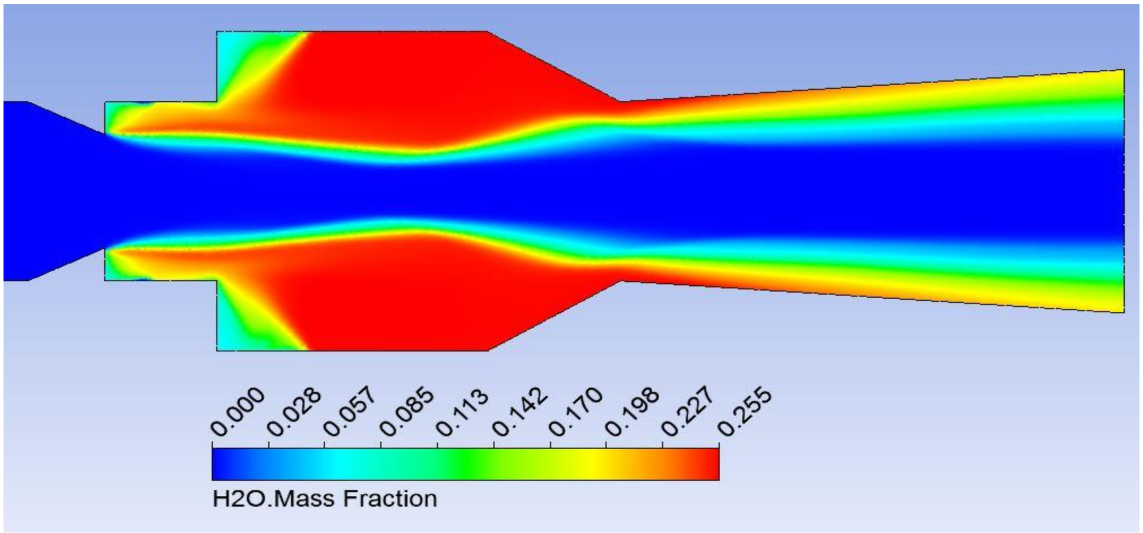

Figure 70 Flame Position, Double Cavity M = 10

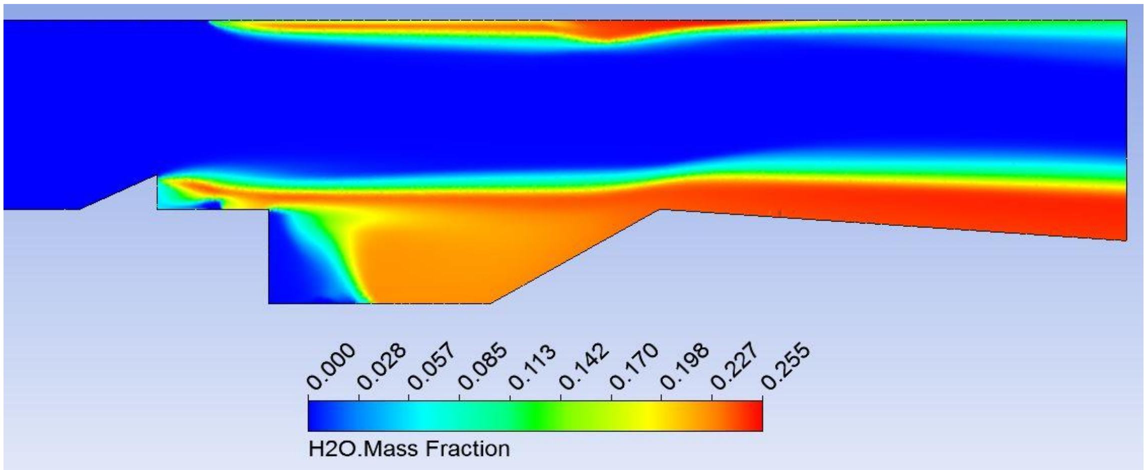

Figure 71 Flame Position, Slanted Cavity with Top Injector M = 10

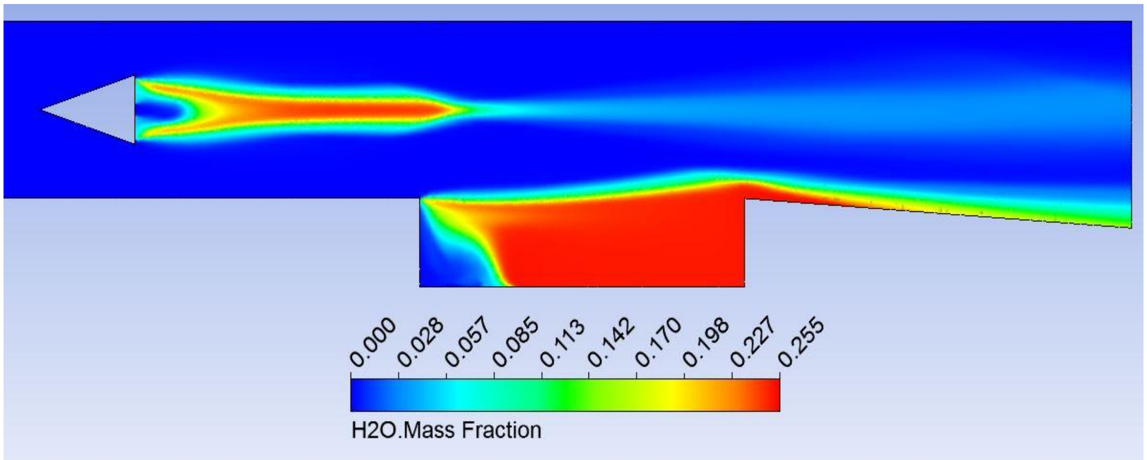

Figure 72 Flame Position, 10 mm Strut-Cavity M = 10

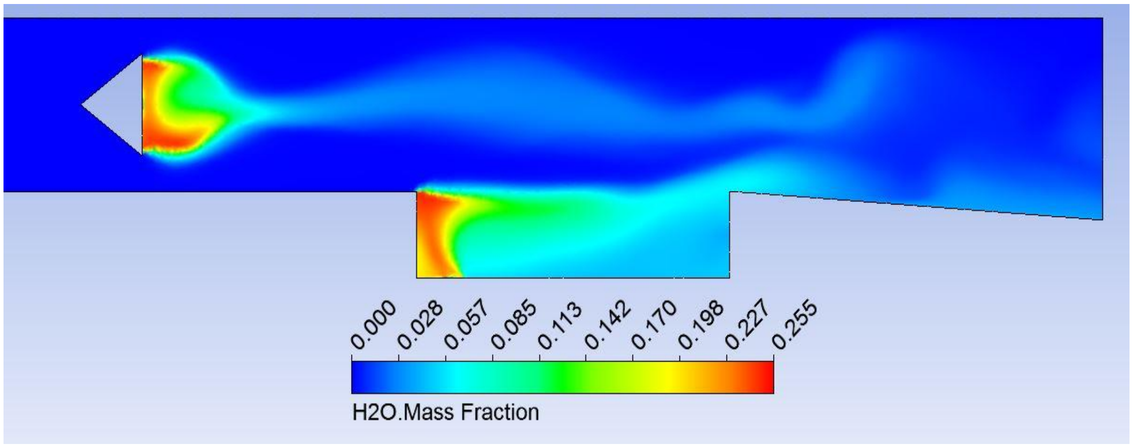

Figure 73 Flame Position, 15 mm Strut-Cavity M = 10

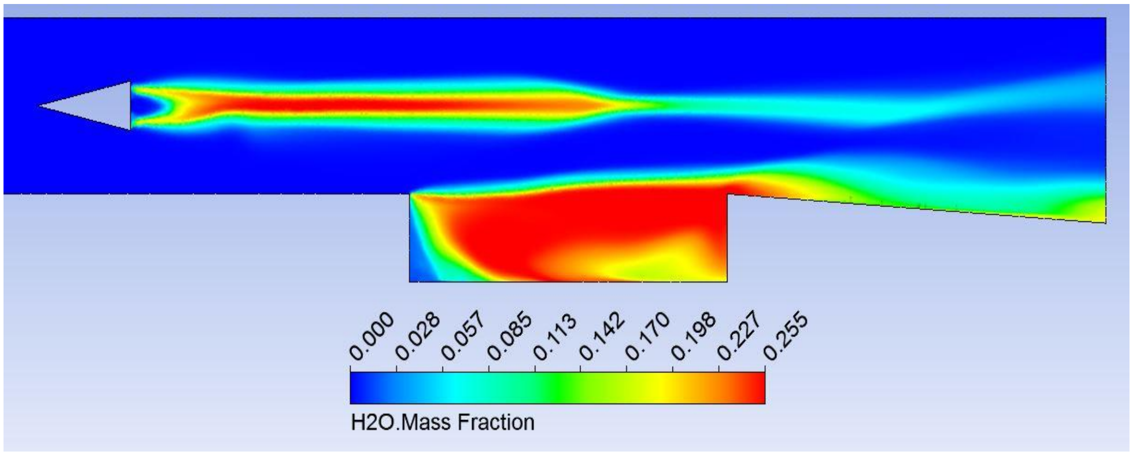

Figure 74 Flame Position, 7.17 mm Strut-Cavity M = 10

The results at an inlet Mach number of 10 demonstrate that the geometries are capable of sustaining a flame at high flight velocities. The combustion regions are shown to anchor in the shear layers produced by the cavity, strut, and ramp and extend downstream towards the nozzle. The 15 mm strut, as compared to the other widths, demonstrates a much shorter flame attached to the downstream face due to the large angle of deflection.

While it has been demonstrated that all of the geometries are adequate at stabilizing a flame at varying Mach numbers, the effects of the flameholders on the reacting flow must be discussed if the engine is designed for practical applications.

4.7 Viability of Flameholders in a Reacting Flow

4.7.1 Shock Trains and Engine Unstart

As shown in Section 4.1.1, the flameholders tend to generate compression and expansion waves in the isolator, combustor, and nozzle as a result of changing geometry. In a reacting flow, these waves, coupled with the pressure rise from combustion and thermal choking, may limit the ability of the engine to produce thrust and therefore its viability as a propulsion device.

Shock waves created due to the flameholders tend to form a shock train in the isolator; this is comprised of a set of successively smaller compression waves beginning with a pair of oblique shock waves that combine into a Mach disk at their meeting point. Behind the first shock, reacceleration occurs, followed by alternating compression and acceleration until the end of the train is reached. The starting location of this shock train is one of the many contributing factors to engine unstart. If the first shock is too close to the inlet of the isolator, the mass flow rate of air into the engine may be disrupted, leading to a loss of thrust. Possible unstart behavior was exhibited in several of the strut-cavity designs at an inlet Mach number of 2.2; these are shown in Fig. 75.

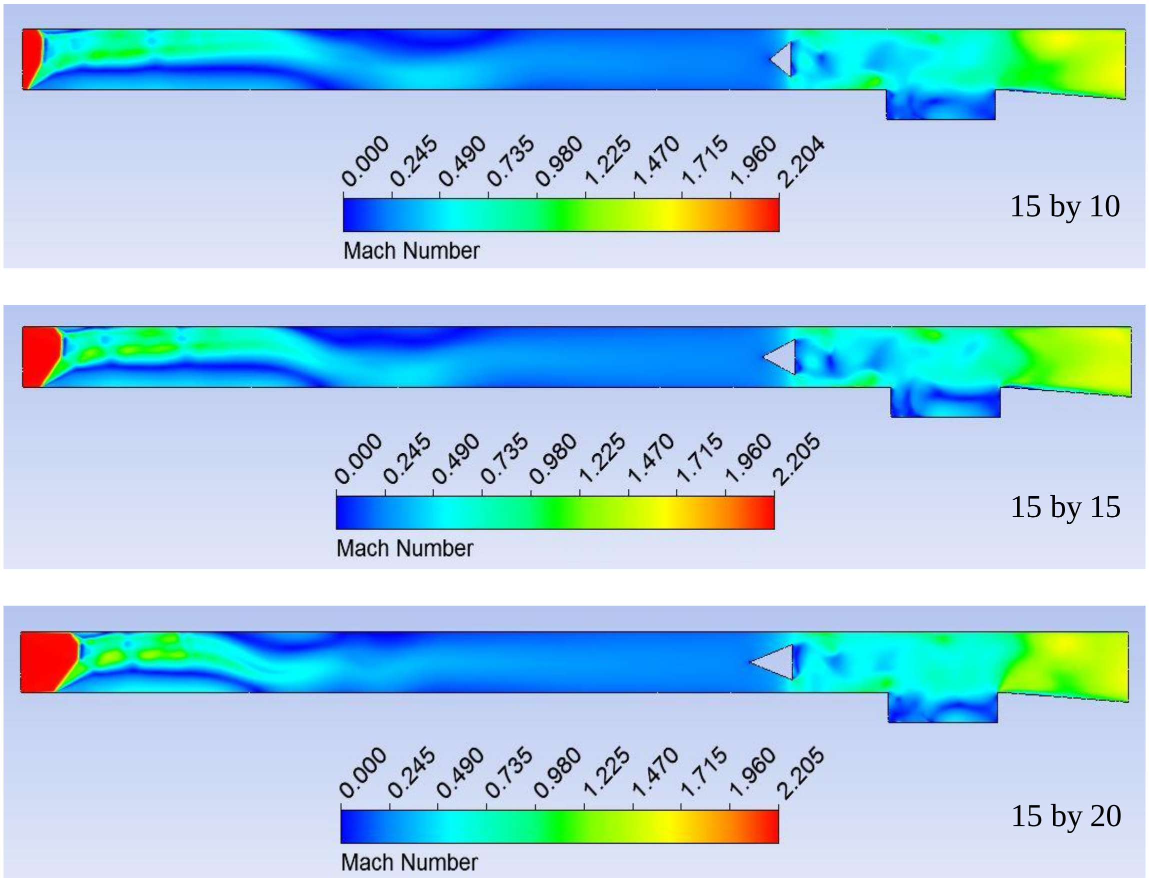

Figure 75 Potential Unstart Conditions, 15 mm Strut-Cavity M = 2.2

The first shock in all three cases is approaching the isolator inlet, resulting in a shock train that quickly drops the flow Mach number below one; this limits reacceleration of the flow, leading to subsonic combustion. While subsonic combustion is viable in most cases (turbojets/turbofans, ramjets), the significant loss of stagnation pressure and fluctuation of mass flow rate in a scramjet will severely limit thrust generation at supersonic or hypersonic speeds. This phenomenon was also observed at an inlet Mach number of 4 for the 15 mm by 10 mm and 15 mm by 15 mm strut-cavity cases; these are shown in Fig. 76.

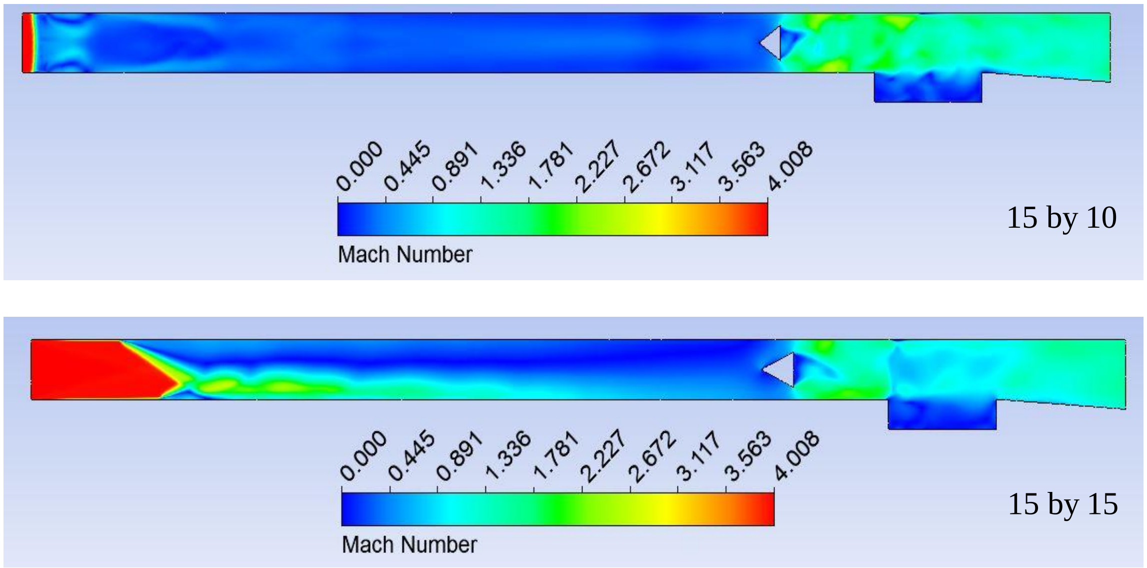

Figure 76 Potential Unstart Conditions, 15 mm Strut-Cavity M = 4

When the inlet Mach number was increased further, the shock train was pushed downstream into the isolator, eventually becoming attached to the strut, ramp, or leading edge of the cavity. This is expected behavior in the engine, as the increasing Mach number also leads to an increase in total upstream pressure, forcing the shock towards the combustor. This displacement of the shock train is shown in Fig. 77 for the 15 mm strut-cavity design.

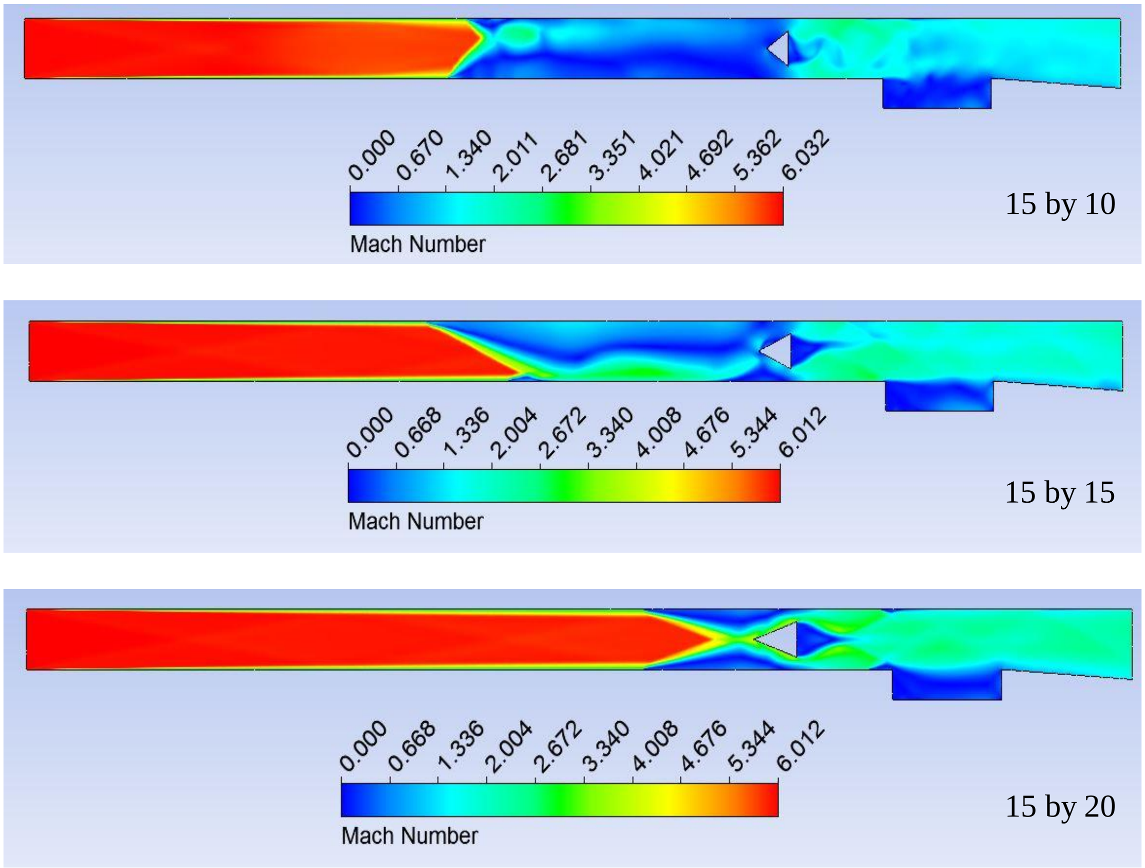

Figure 77 Translated Shock Train in 15 mm Strut-Cavity M = 6

4.7.2 Stagnation/Total Pressure Losses

As discussed in Section 4.1.1, shock waves cause a drop in stagnation (or total) pressure of the flow as it progresses through the isolator and into the combustor; stronger compression regions (that is, shocks that are nearly normal or long shock trains) cause larger drops in stagnation pressure. This drop in stagnation pressure translates to a decrease in flow energy, thereby reducing the amount of thrust that can be generated.

The normalized stagnation pressure of the flow was plotted as function of the distance from the inlet of the isolator in order to observe the losses that occur from flameholder-generated shocks and from friction. These plots are shown in Figs. 78-82.

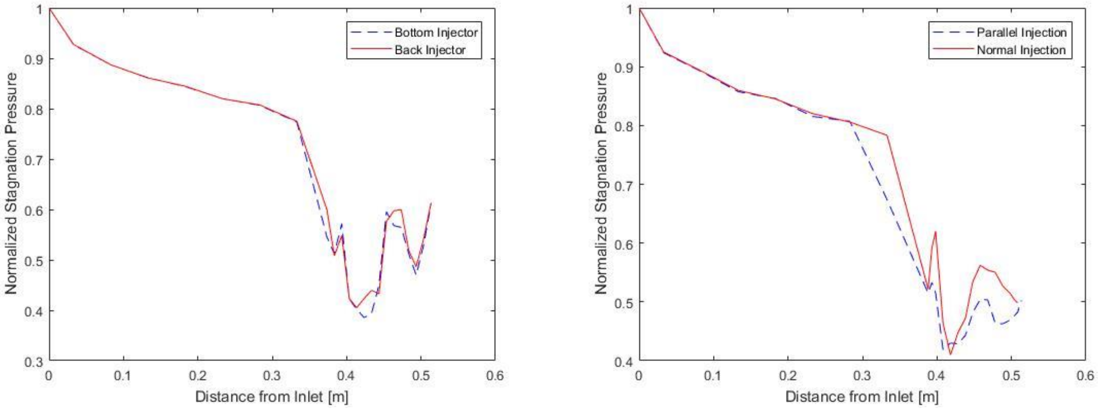

(a) Square Cavity (b) Slanted Cavity

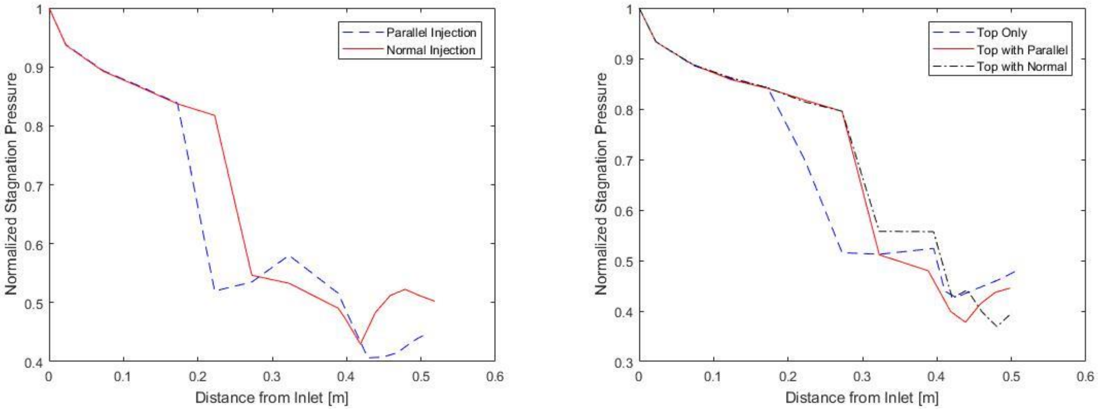

(c) Double Cavity (d) Slanted Cavity with Top Injector

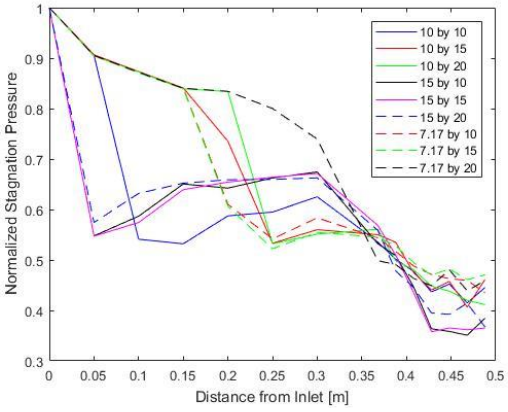

(e) Strut-Cavity

Figure 78 Stagnation Pressure at M = 2.2

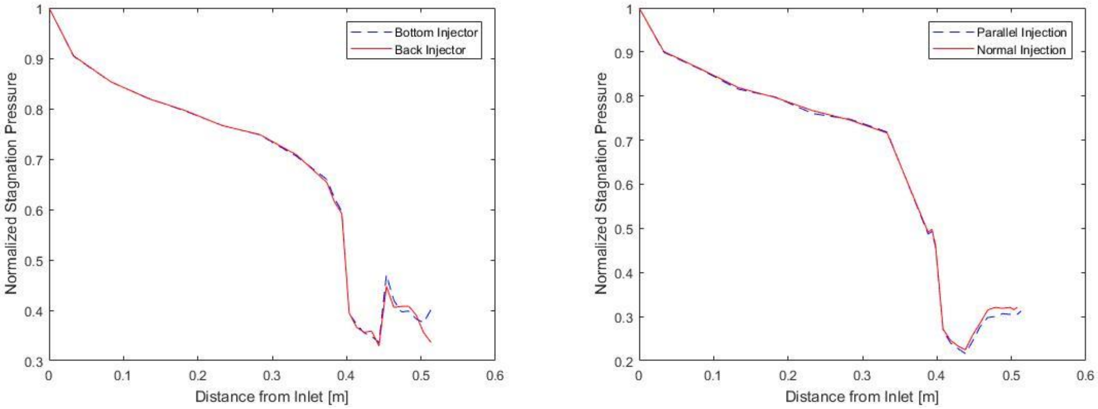

(a) Square Cavity

(b) Slanted Cavity

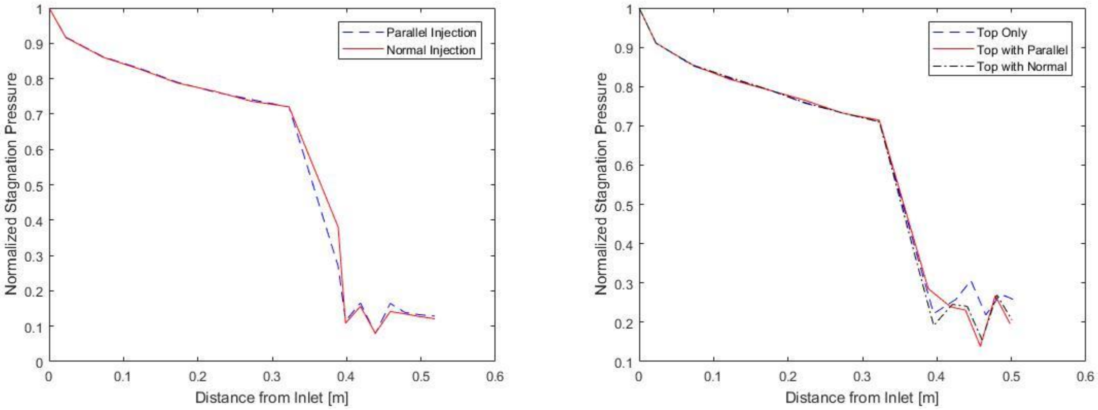

(c) Double Cavity

(d) Slanted Cavity with Top Injector

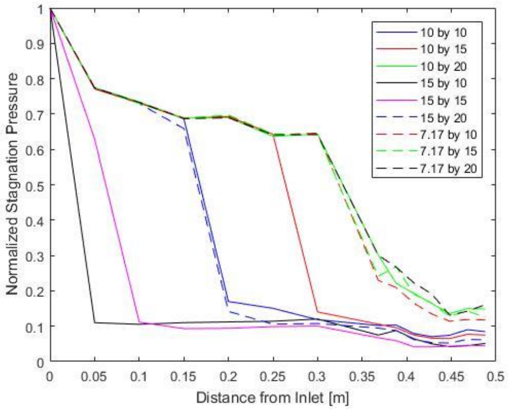

(e) Strut-Cavity

Figure 79 Stagnation Pressure at M = 4

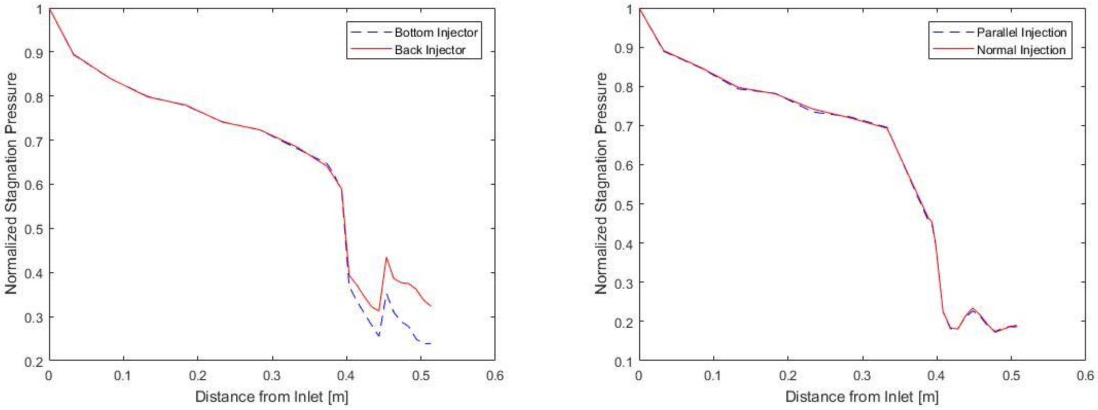

(a) Square Cavity

(b) Slanted Cavity

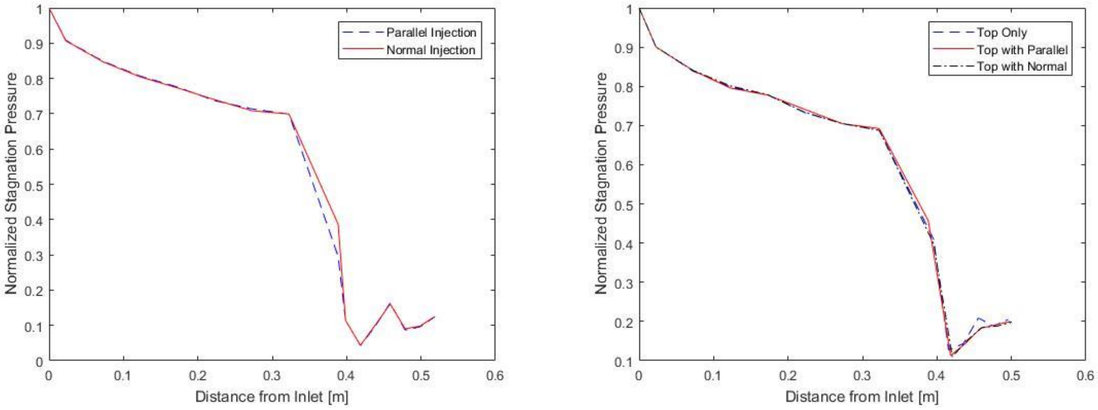

(c) Double Cavity

(d) Slanted Cavity with Top Injector

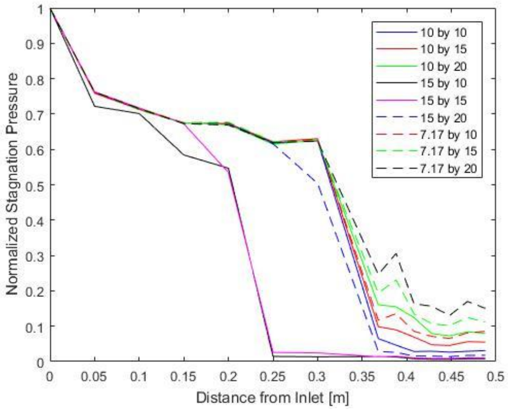

(e) Strut-Cavity

Figure 80 Stagnation Pressure at M = 6

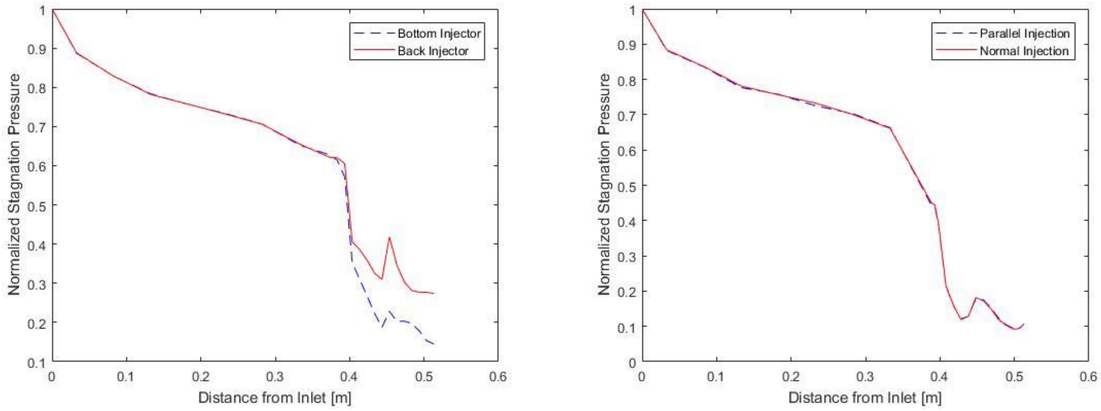

(a) Square Cavity

(b) Slanted Cavity

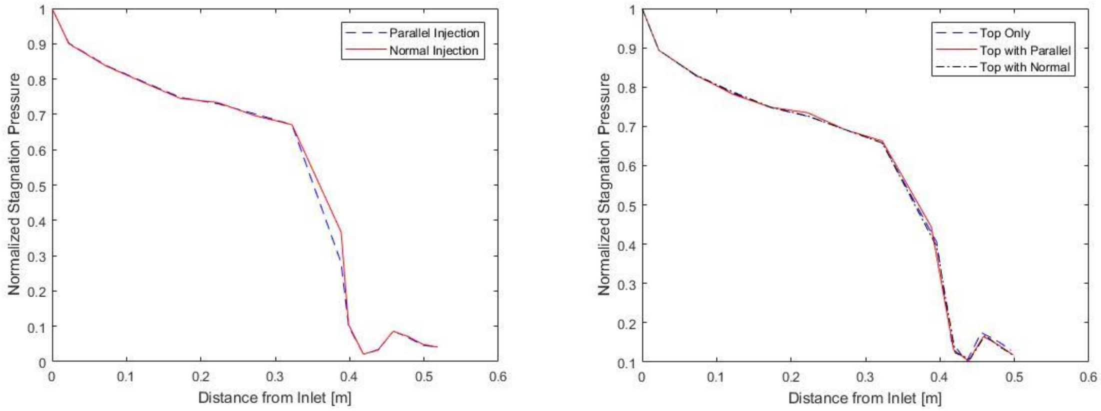

(c) Double Cavity

(d) Slanted Cavity with Top Injector

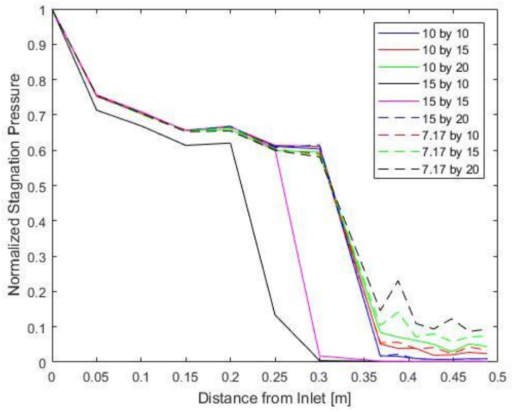

(e) Strut-Cavity

Figure 81 Stagnation Pressure at M = 8

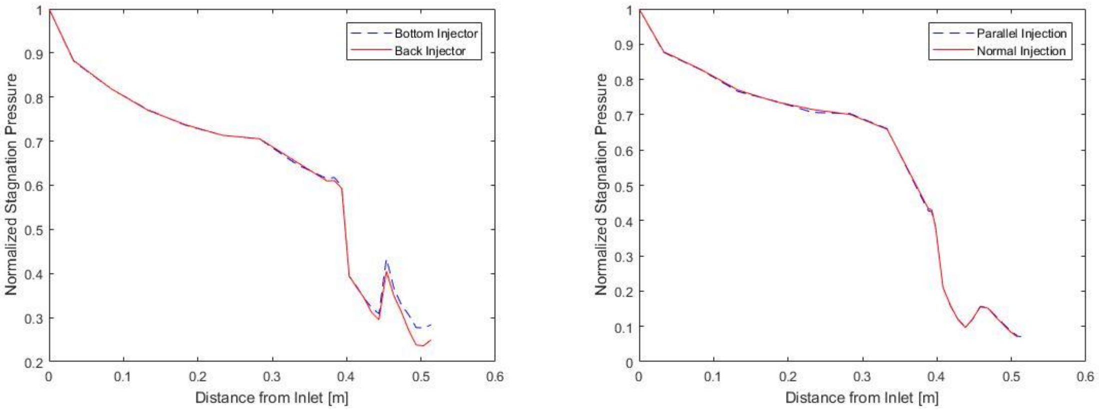

(a) Square Cavity

(b) Slanted Cavity

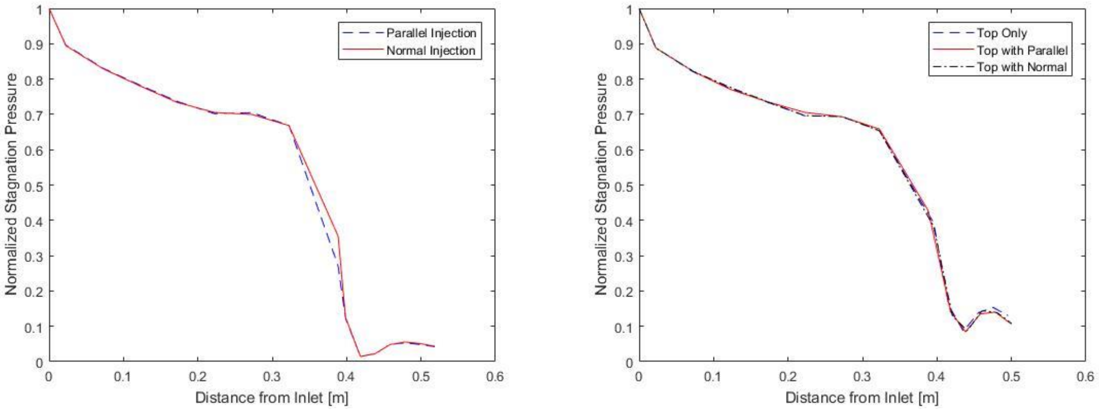

(c) Double Cavity

(d) Slanted Cavity with Top Injector

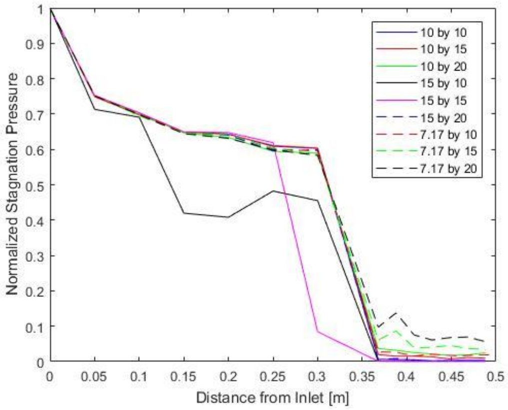

(e) Strut-Cavity

Figure 82 Stagnation Pressure at M = 10

These figures show a consistent trend across all flameholders: friction generates a steady decrease in stagnation pressure until a shock is reached, at which point the stagnation pressure drops significantly. The locations of these drops in pressure are consistent with the observed location of shocks in the combusting simulations. While the square cavity, slanted cavity with and without top and injector, and double cavity show a consistent drop in stagnation pressure across all Mach numbers, the use of a strut alters the location of the shock based on the inlet flow velocity. As shown in Fig. 79(e) and Fig. 80(e), the shocks are far closer to the inlet of the isolator for certain strut shapes as compared to the other flameholder geometries; this results in a low stagnation pressure as the air enters the combustor. As discussed in the previous section, the shocks are translated downstream at higher Mach numbers.

Although not as detrimental as engine unstart due to shock location or thermal choking, the loss of stagnation pressure in a scramjet is necessary to consider in the overall design of the combustor. From these simulations, the strut-cavity designs generate drops in stagnation pressure at points further upstream from the inlet of the combustor than other geometries. The shocks in the strut-cavity designs also appear to be stronger based on the steeper drops in stagnation pressure across a shorter distance. While normal shocks do occur in scramjet isolators in the form of shock trains, the increased back pressure due to the strut appears to increase the strength of these shocks. This negatively affects performance of the engine, and leads to insufficient thrust at high flight velocity.

Stagnation pressure loss in a scramjet engine is unavoidable, and the geometry of the combustor has been shown to affect the overall drop through the engine. To further investigate the performance of the engine based on the geometry of the combustor, the net thrust produced due to combustion is analyzed.

4.7.3 Net Thrust

To calculate the thrust produced by an air breathing engine, an equation based on a linear momentum analysis of the engine can be used. This equation is written as

$$F_T = \dot{m}_e v_e - \dot{m}_i v_i + (p_e - p_i) A_e \tag{36}$$

where $\dot{m}_e$ and $\dot{m}_i$ are the outlet and inlet mass flow rates, respectively, v_e and v_i the outlet and inlet flow velocities, p_e and p_i the outlet and inlet pressure, and A_e the outlet cross sectional area. Using Eq. (36), thrust was calculated as a function of inlet Mach number and is plotted in Fig. 83. It must be noted that the simulations run for this study are quasi-2D, and do not completely represent the actual performance of the engine. The thrust values shown in this figure can be considered approximate representations of the drag generated by the flameholders. To properly calculate the thrust, a 3D simulation would be required.

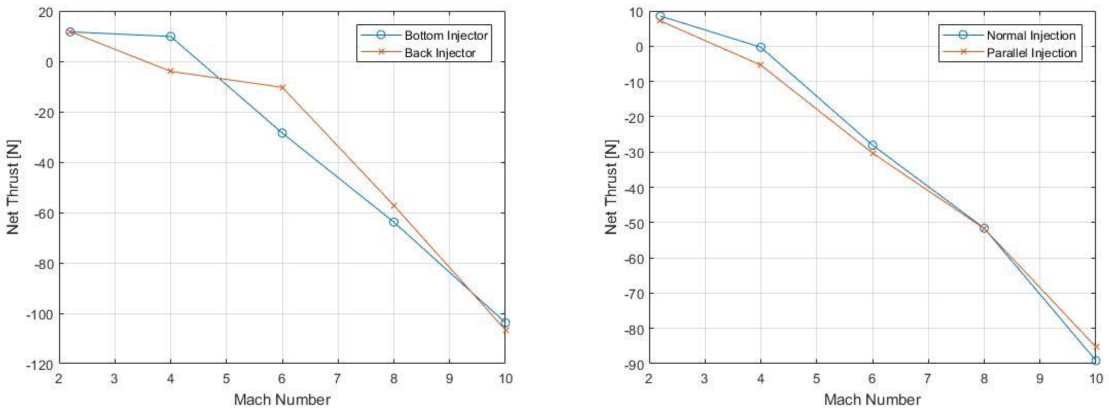

(a) Square Cavity

(b) Slanted Cavity

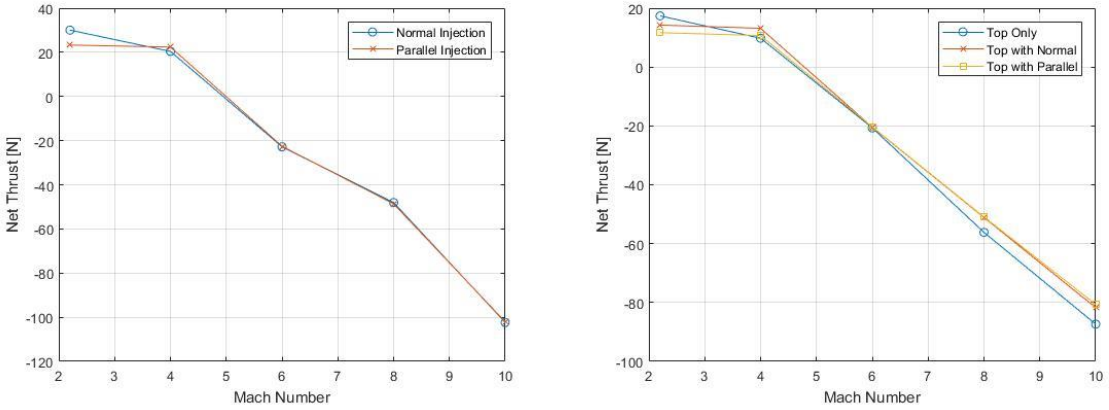

(c) Double Cavity

(d) Slanted Cavity with Top Injector

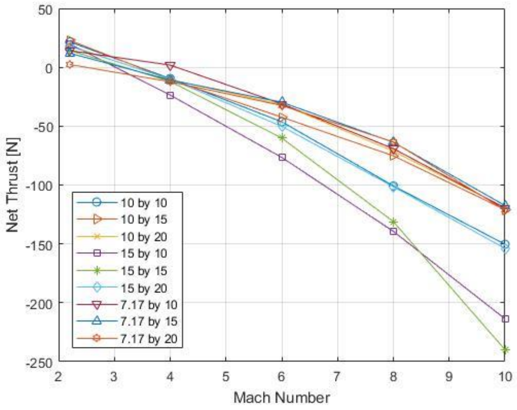

(e) Strut-Cavity

Figure 83 Net Thrust by Mach Number

The overall force produced appears to be close to a linear, negative relationship between inlet Mach number and thrust. At low Mach numbers (M = 2.2, M = 4), the thrust of all geometries tends to be positive. It then proceeds to become increasingly negative as inlet Mach number increases, demonstrating that drag inside of the engine predominates over thrust generated by combustion. This is highly evident in the strut-cavity plot in Fig. 83(e), with all designs becoming heavily dominated by drag at high Mach numbers. This increase in drag can be attributed to the strut in the flow field, which has already been shown in Section 4.7.1 and Section 4.7.2 to lead to potential engine unstart and significant stagnation pressure loss. Although the other flameholders produce increasingly negative thrust, they do not reach the level of the strut-cavity, which ranges between -100 and -250 Newtons at an inlet Mach number of 10; at the same Mach number, the largest thrust was produced by the slanted cavity with a top injector at a value of around -80 N. This still demonstrates that drag dominates over thrust generated by combustion at high Mach numbers.

The drag values from this study should not be taken as absolute values for an actual scramjet engine; as stated, these should only be used as a comparison of drag generated by the flameholders. Using this metric, the strut-cavity design has the largest impact on drag. This is to be expected, as the introduction of a body into the flow field will produce a force against the flow, reducing its linear momentum and thus its velocity. The other designs do not appear to have as drastic of an effect as the strut, as the majority of geometric variation occurs on the far edges of the flow field.

5 Conclusion

Four combustor geometries and a total of 18 different fuel injector layouts were tested to gauge the flameholding ability and overall performance of a scramjet engine at five inlet Mach numbers. The mixing efficiencies at an inlet Mach number of $M = 2.2$ were calculated to understand the ability of the geometry to disperse fuel such that proper combustion would occur. The production and sustainability of a flame in the combustor was investigated using H_2O mass fraction contours across all Mach numbers, Mach contours were used to observe engine unstart, and stagnation pressure and net thrust plots were created to describe the overall performance of each design as a scramjet engine.

The strut-cavity design initially appears to be beneficial for overall fuel dispersion, as well as flame distribution and sustainability in the combustor; however, its tendency to produce large and strong shock trains which negatively affect stagnation pressure, as well as the large amount of drag created by the strut-cavity combination would be detrimental for operation as a thrust producing device. All other geometries demonstrated their ability to sustain a flame at varying inlet Mach numbers. Based on the other metrics investigated, the square cavity flameholder with a back cavity injector appears to be the most beneficial for use in a scramjet engine. Its simple design reduces stagnation pressure losses and drag in the engine, and the cavity produces an adequate shear mixing layer and recirculation region in which fuel and air can mix and hot gases and radicals can recirculate to maintain combustion.

Further experimentation is necessary to demonstrate complete viability of these flameholders relative to one another. While these quasi-2D analyses demonstrate general trends and patterns of the performance of the engines, it would be necessary to either run full 3D models (including transient studies for startup and shutdown) or small/large scale physical trials. Many experimental studies have already been performed based on existing flameholder designs. Further small and large scale testing at a variety of Mach numbers can only help to improve understanding of the performance of various flameholders. Development and analysis through CFD and physical testing of new flameholder geometries may also help fully realize the potential of scramjet engines.

Nomenclature

A - cross sectional area

A_e - engine outlet cross sectional area

a_1 - k-ω model constant

C_i - mass concentration of gas i

c - speed of sound

D_i - diffusion coefficient of gas i

d - distance to closest wall

F_T - thrust

F_1 - first blending function for k-ω turbulence model

F_2 - second blending function for k-ω turbulence model

f_i - body force in direction i

H - height of isolator

K - eddy diffusion coefficient

k - turbulent kinetic energy

M - Mach number

$\dot{m}_e$ - outlet mass flow rate

$\dot{m}_i$ - inlet mass flow rate

p - pressure

p_i - engine inlet pressure

p_e - engine exit pressure

R - ideal gas constant

$\bar{R}_{ij}$ - Reynolds stress tensor

S_i - production and consumption of species

T - temperature

t - time

u_j - velocity in direction j

v_e - flow velocity exiting engine

v_i - flow velocity entering engine

x - distance downstream from first fuel inlet

x^* - non-dimensional distance from first fuel inlet

x_j - direction j

Y_i - mass fraction of gas i

Y_{R,H_2} - reacting mass fraction of hydrogen

Y_s - stoichiometric mass fraction

β - k-ω model constant

β^* - k-ω model constant

γ - ratio of specific heats

γ_ω - k-ω model constant

δ_{ij} - Kronecker delta tensor

η_M - mixing efficiency

μ - dynamic viscosity

μ_t - eddy viscosity

ν - kinematic viscosity

ρ - density

σ_k - k-ω modeling constant

σ_ω - k-ω modeling constant

$\sigma_{\omega 2}$ - k-ω modeling constant

σ_{ij} - viscous stress tensor

τ_{ij} - Cauchy stress tensor

ϕ - blended k-ω constant

ϕ_1 - first constant from list of k-ω values

ϕ_2 - second constant from list of k-ω values

Ω - magnitude of vorticity

ω - specific rate of dissipation

References

[1] Dunbar, Brian. “How Scramjets Work” from https://www.nasa.gov/centers/langley/news/factsheets/X43A_2006_5.html

[2] Choubey, Gautam and Pandey, K.M. “Effect of parametric variation of strut layout and position on the performance of a typical two-strut based scramjet combustor.” *International Journal of Hydrogen Energy* Vol. 42 (2017): pp. 10485-10500.

[3] Micka, Daniel J. and Driscoll, James F. “Combustion characteristics of a dual-mode scramjet combustor with cavity flameholder.” *Proceedings of the Combustion Institute* Vol. 32 No. 2 (2009): pp. 2397-2404.

[4] Ben-Yakar, Adela and Hanson, Ronald K. “Cavity Flame-Holders for Ignition and Flame Stabilization in Scramjets: An Overview.” *Journal of Propulsion and Power* Vol. 17 No. 4 (2001): pp. 869-877.

[5] Huang, Wei and Yan, Li. “Numerical investigation on the ram-scram transition mechanism in a strut-based dual-mode scramjet combustor.” *International Journal of Hydrogen Energy* Vol. 41 (2016): pp. 4799-4807.

[6] Dunbar, Brian. “X-43A (Hyper-X)” from https://www.nasa.gov/centers/armstrong/history/experimental_aircraft/X-43A.html

[7] Mura, Amaud and Izard, Jean-François. “Numerical Simulation of a Supersonic Nonpremixed Turbulent Combustion in a Scramjet Combustor Model.” *Journal of Propulsion and Power* Vol. 26 No. 4 (2010): pp. 858-868

[8] Berglund, M. and Fureby, C. “LES of supersonic combustion in a scramjet engine model.” *Proceedings of the Combustion Institute* Vol. 31 (2007): pp. 2497-2504

[9] Pan, Yu, Tan, Jian-Guo, Liang, Jian-Han, Liu, Wei-Dong, and Wang, Zhen-Guo. “Experimental investigation of combustion mechanisms of kerosene-fueled scramjet engines with double-cavity flameholders.” *Acta Mechanica Sinica* Vol. 27 No. 6 (2011): pp. 891-897.

[10] Gatski, Thomas B. and Bonnet, Jean-Paul. *Compressibility, Turbulence, and High Speed Flow.* Academic Press, Oxford (2013).

[11] Rumsey, Chris L. "Compressibility Considerations for k-ω Turbulence Models in Hypersonic Boundary Layer Applications." NASA/TM-2009-215705. Langley Research Center, Hampton, VA. 2009.

[12] Rumsey, Chris L. "SSG/LRR Full Reynolds Stress Model" from https://turbmodels.larc.nasa.gov/

[13] Woelke, Michał. "Eddy Viscosity Turbulence Models employed by Computational Fluid Dynamic." *Transactions of the Institute of Aviation* No. 191 (2007): pp. 92-113.

[14] Stocker, Thomas. "Describing Transports of Energy and Matter." *Introduction to Climate Modeling*. Springer-Verlag, Berlin Heidelberg (2011): pp. 53-77.

[15] ANSYS® Academic Research CFX, Release 17.0, Help System, CFX-Solver Theory Guide, ANSYS, Inc.

[16] Tunçer, Onur. "COMBUSTION IN A RAMJET COMBUSTOR WITH CAVITY FLAME HOLDER." *Journal of Thermal Science and Technology* Vol 30, No. 2 (2010): pp. 57-68.

[17] "Module 3: Hydrogen Use in Internal Combustion Engines." College of the Desert, Palm Desert, CA. 2001.

[18] Kedia, Kushal S. and Ghoniem, Ahmed F. "The anchoring mechanism of a bluff-body stabilized laminar premixed flame." *Combustion and Flame* Vol. 161 (2014): pp. 2327-2339.

[19] Wan, Jianlong, Fan, Aiwu, Yao, Hong, and Liu, Wei. "Flame-anchoring mechanisms of a micro cavity-combustor for premixed H_2/air flame." *Chemical Engineering Journal* Vol. 275 (2015): pp. 17-26

[20] McGann, Brendan, Baccarella, Damiano, Lee, Tonghun, and Narayanaswamy, Venkat. "Inlet Isolator and Combustion Physics at Take-Over Region of Scramjet Engines." AFOSR Review Meeting. United States Air Force, North Carolina State University, and University of Illinois, Urbana-Champaign. 2017.

[21] Hyslop, Peter. "CFD Modelling of Supersonic Combustion in a Scramjet Engine." Master's Thesis. Australian National University, Canberra, Australia. 1998.